Title	Idealized Experiments and Data-driven Analysis for Hot-Press Joining Mechanism and Strength of Aluminum/CFRTP Joints
Author(s)	Li, Weihao
Citation	大阪大学, 2025, 博士論文
Version Type	VoR
URL	https://doi.org/10.18910/103234
rights	
Note	

Doctoral Dissertation

Idealized Experiments and Data-driven Analysis for Hot-Press Joining Mechanism and Strength of Aluminum/CFRTP Joints

理想化実験とデータ駆動型解析を用いた Aluminum/CFRTP 熱圧接メカニズムと継手強度の研究

LI WEIHAO

July 2025

Division of Global Architecture,
Graduate School of Engineering,
The University of Osaka

Doctor of Engineering Dissertation
submitted to
Department of Naval Architecture and Ocean Engineering
Division of Global Architecture
Graduate School of Engineering
The University of Osaka

July 2025

Supervised by
Professor Ninshu Ma

Committee members

Professor Naoki Osawa

- Department of Naval Architecture and Ocean Engineering, Graduate School of Engineering. The University of Osaka

Professor Kazuhiro Iijima

- Department of Naval Architecture and Ocean Engineering, Graduate School of Engineering. The University of Osaka

Professor Akira Tatsumi

- Department of Naval Architecture and Ocean Engineering, Graduate School of Engineering. The University of Osaka

Table of Contents

List of Abbreviations and Symbols

ALE: Arbitrary Lagrangian and Eulerian

CF: carbon fiber

CFRTP: carbon fiber reinforced thermoplastics

DSC: differential scanning calorimetry

DWF: Defect Width Features

EDS: Energy Dispersive X-ray Spectroscopy

FEA: finite element analysis

FIB: focused ion Beam

FSW: friction stir welding

GBDT: gradient-boosted decision tree

MAE: mean absolute error

MSE: mean squared error

R^2: coefficient of determination

RAZ: resin adhesion zone

ROZ: resin outflow zone

SAD: selected area diffraction

SCA: silane coupling agent

SCL: silane coupling layer

SEM: Scanning Electron Microscope

TAZ: tool-affected zone

TEM: Transmission Electron Microscope

TGA: thermogravimetric analysis

XPS: X-ray Photoelectron Spectroscopy

θ_T^*: Dimensionless Max Temperature

θ_P^*: Dimensionless Applied Pressure

θ_M^*: Melting Residence Ratio

θ_D^*: Decomposition Residence Ratio

θ_{DM}^*: Decomposition-to-Melting Time Ratio

δ_{Ir}^*: Dimensionless Raman intensity

δ_{ca}^*: Effective Contact Area Ratio

δ_v^*: Dimensionless Complex Viscosity

δ_L^*: Normalized Layer Thickness of Defect

δ_N^*: Defect Count

δ_{Ar}^*: Normalized defect area

δ_{dhl}^*: Average Defect Aspect Ratio

σ_r^*: Dimensionless Strength

List of Figures

List of Tables

Abstract

The increasing demand from naval architecture, ocean engineering, aerospace and automotive industries for manufacturing multifunctional and lightweight structural components is extending the use of carbon fiber reinforced thermoplastics (CFRTPs) and aluminum (Al) alloys. However, the sound joining of these dissimilar materials, which have completely different properties, is a great challenge. This study presents a comprehensive investigation into the thermo-mechanical joining mechanisms and performance evaluation of Al/CFRTP joints, with a particular focus on hot-press joining and its extension to friction spot joining (FSpJ). An idealized controllable hot-press platform was developed to systematically explore the independent effect of temperature, pressure, and time on joint formation. Through experimental observations using SEM, TEM, XPS and Raman spectroscopy, the correlation between the joint strength obtained by mechanical tests and the microstructural evolution as well as chemical reactions at the Al/CFRTP interface was elucidated. A thinning-controlled joining strategy was introduced to investigate the pressure effect and prevent excessive deformation, enabling more precise insight into polymer flow, defect formation and interfacial bonding. To bridge the process–structure–property relationship, a data-driven analysis framework was established. Physical features such as reaction layer thickness, void morphology, and bonding area were quantified and used as input to train gradient-boosted decision tree (GBDT) models. Through model distillation, interpretable mathematical equations were extracted, providing predictive capability and mechanistic understanding of joint strength evolution. These models were further validated through experiments on Al/CFRTP joints with varied conditions. Finally, the knowledge gained from hot-press studies was extended to more complex and dynamic FSpJ process. Numerical simulations based on thermo-mechanical coupling (ALE formulation) were conducted to evaluate temperature field and material deformation under different tool geometries. The results revealed the

influence of tool concavity on heat input distribution, polymer melting behavior, and joint integrity. This research offers not only practical guidelines for process design and optimization of Al/CFRTP joints, but also a generalizable framework for data-driven analysis of complex multi-material joining systems. The insights obtained herein contribute to the advancement of intelligent, high-performance hybrid structure manufacturing.

1.Introduction

1.1 Research Background and Motivation

With the increasing global emphasis on carbon neutrality and energy efficiency, lightweight structural materials have become crucial across various sectors, including transportation, aerospace, and high-end manufacturing. Material selection and optimization directly impact energy consumption, emission levels, and overall operational performance, making the development of high-specific-strength, corrosion-resistant, and cost-effective lightweight materials a critical objective for the manufacturing industry [1]. Conventional ferrous alloys, particularly steels, have long dominated structural applications due to their high strength, good formability, and relatively low cost. However, their high density inherently limits the potential for weight reduction, and challenges remain in achieving high specific strength and long-term corrosion resistance. In applications demanding extreme lightweight and high performance, such as automotive and aerospace engineering, the shortcomings of traditional steel materials have become increasingly evident. Compared to traditional metals, aluminum alloys (Al alloys) offer significant advantages, including low density (approximately one-third that of steel), high specific strength, excellent corrosion resistance, and favorable formability [2]. These properties have led to their widespread adoption in automotive body structures, aerospace skins, and railway vehicle frames, effectively balancing weight reduction and structural integrity [3]. On the other hand, non-metallic materials are also widely used due to their lighter weight. Traditional thermoplastic materials, such as polypropylene (PP) and polycarbonate (PC), although lightweight and easy to process, often suffer from insufficient mechanical strength and poor dimensional stability under load. Carbon fiber reinforced thermoplastics (CFRTPs), particularly carbon fiber reinforced polyamide 6 (CF/PA6) composites, have emerged as promising alternatives due to their superior specific strength, high impact resistance, and excellent recyclability. Their thermal processability further enables large-scale manufacturing via techniques such as compression molding and injection molding. By integrating Al alloys with CFRTPs, it is possible to achieve an optimal balance between weight reduction, mechanical performance, and multi-functional integration, highlighting the immense potential of hybrid structures in high-performance vehicle applications [4]. However, achieving a high-performance joining between metallic alloys and plastics, including carbon-fiber-reinforced thermoplastic (CFRTPs), is challenging through the conventional methods used in metal welding or joining. Since the thermal decomposition temperature of plastics is often much lower than the melting temperature of metals, it is difficult to weld them together directly by conventional fusion welding methods. Moreover, the joining process itself involves highly coupled multi-physics phenomena, including heat transfer, polymer melt flow, interfacial chemical reactions, and defect evolution. These interconnected mechanisms lead to complex and unpredictable interfacial structure formation, making it challenging to achieve precise control over joint quality. Consequently, ensuring the structural reliability and performance stability of dissimilar material joints under complex service environments remains a critical technical hurdle.

1.2 Current Status of Al/CFRTP Joining Technologies

To realize the advantages of both Al alloys and CFRTPs in hybrid structures, effective joining between these dissimilar materials is essential. However, traditional joining methods developed for homogeneous material systems exhibit considerable limitations when applied to metal/polymer hybrid structures. Mechanical fastening methods, such as riveting and bolting, have been widely employed due to their simplicity and reliability in metal structures. Nevertheless, when applied to Al/CFRTP hybrids, mechanical fastening often results in stress concentration around the fasteners, leading to premature failure under dynamic or cyclic loading. Furthermore, the need for hole drilling in CFRTP components compromises the fiber continuity and structural integrity, significantly reducing the overall mechanical performance [5]. Additionally, the added weight from fasteners and reinforcements offsets the lightweight benefits of the hybrid structure. Adhesive bonding, another conventional approach, offers a continuous load distribution along the interface and avoids fiber damage. However, adhesive joints are highly sensitive to surface conditions, environmental factors (such as moisture and temperature), and long-term degradation. The strength and durability of adhesive joints are difficult to guarantee without meticulous surface preparation and environmental protection measures. Moreover, the curing time and complexity associated with adhesive bonding processes reduce manufacturing efficiency, posing challenges for large-scale production [6].

To address the limitations of conventional methods, various thermally assisted joining technologies have been developed and increasingly adopted for Al/CFRTP hybrid structures. These techniques, including laser-assisted joining [7–9], ultrasonic welding [10], resistance spot welding [11,12] and several friction-based solid-state joining processes [13–15], introduce controlled thermal energy and/or mechanical pressure at the interface to soften or locally melt the polymer matrix while activating the metal surface. Through this process, stronger interfacial adhesion can be achieved by enhancing physical interlocking and promoting chemical bonding. Thermally assisted joining processes offer improved joint strength, processing efficiency, and design flexibility compared to traditional mechanical fastening and adhesive bonding approaches and have become the focus of considerable research and industrial interest for lightweight hybrid structures. Regardless of the joining process, the formation of strong and durable Al/CFRTP joints fundamentally depends on two key interfacial mechanisms: mechanical interlocking and chemical bonding [16,17]. Mechanical interlocking arises from the physical penetration of softened resin into surface asperities or engineered features on the metal surface, creating mechanical anchorage upon solidification. Metal surface pre-treatment strategies, such as additive-manufactured groove structures and laser texturing treatment [9], can enhance the static strength of joints by reinforcing mechanical interlocking. As for chemical bonding, covalent bonding is the main form of chemical bonding between functional groups on the metal surface and the molten matrix resin. To enhance these bonds, the metal surface is pretreated with a silane coupling agent (SCA) because this will increase active functional group density that can react with the molten-state matrix resin of the CFRTP. Ren et al. [11] successfully joined silanized 5052 Al alloy with CFRTP and established a relationship between welding current and joint tensile strength, where the effective bonding area within the melting range significantly contributes to joint strength. Choi et al. [13] found that friction lap joining of silanized pure Ti and CFRP joints resulted in high shear strength when the interface temperature was within the melting and thermal decomposition points of the CFRP. Despite progress in exploring these bonding mechanisms across various joining techniques, current research still faces significant limitations in fully understanding and predicting the evolution of joint properties. One major challenge lies in the highly dynamic nature of the joining process, which typically involves rapid and localized changes in thermal conditions, mechanical stress states, and polymer flow behavior. These coupled effects induce complex, nonlinear transformations at the interface that are difficult to observe and characterize experimentally. Consequently, there remains a lack of comprehensive understanding of how different process parameters influence interfacial structure development and, ultimately, joint strength and reliability. Bridging this knowledge gap is essential for advancing joining technologies and enabling the rational design of robust Al/CFRTP hybrid structures.

1.3 Research of Welding Behavior under Idealized Thermal–Mechanical Conditions

To address the challenges outlined above, it is essential to establish a deeper and more quantitative understanding of the interfacial phenomena occurring during the joining of Al alloys and CFRTP. Unlike other joining processes that involve highly localized and transient energy input—such as laser, ultrasonic, or friction-based techniques—hot-press joining can provides a relatively uniform and stable thermal–mechanical environment. This enables precise control over the temperature and pressure distributions at the joining interface, facilitating accurate thermal history tracking and reproducible experimental conditions. Moreover, the quasi-static nature of the hot-press process, where the interface remains under steady thermal–mechanical conditions over a defined time period, offers an ideal setting for observing the time-dependent behavior of polymer melt flow, interfacial chemical reactions, and defect evolution. Such well-regulated conditions significantly enhance the observability and interpretability of complex interfacial phenomena. They allow for the systematic decoupling and evaluation of various influencing factors—such as temperature, pressure, residence time, and surface chemistry—on interfacial structure formation and joint performance. In this context, hot-press joining is not merely considered as a practical joining technique, but rather as an idealized experimental platform for elucidating the fundamental physics governing Al–CFRTP bonding.

Furthermore, the mechanistic insights and modeling frameworks developed under hot-press joining conditions possess strong potential for extension to more dynamically complex thermally assisted joining techniques. For instance, understanding the coupling of heat transfer, polymer rheology, and interfacial reaction kinetics in a stable environment provides a foundation for constructing generalized process–structure–property relationships. These relationships are highly transferable to industrially relevant joining methods. In this way, studying joining behavior under near-ideal thermal–mechanical conditions not only advance fundamental scientific understanding but also contributes to the development of predictive models and optimization strategies for hybrid material joining technologies.

1.4 Data-Driven Analysis Approaches to Joining Strength

The fundamental challenge in joining of Al alloys and CFRTPs lies not only in achieving strong interfacial bonding, but also in establishing a predictive and interpretable understanding of how process parameters affect joint formation and performance. As described in Section 1.3, hot-press joining offers a physically stable and controllable environment, making it a valuable platform for mechanistic studies. However, even under stable thermal–mechanical conditions, the joining process involves highly coupled and nonlinear interactions between process variables (e.g., temperature, pressure, holding time), interfacial structures (e.g., chemical bonding, morphological evolution), and mechanical performance (e.g., joint strength, failure mode). This complexity makes it difficult to derive generalizable conclusions from isolated experiments or conventional statistical methods.

To address these challenges, data-driven modeling techniques—particularly those grounded in machine learning (ML)—have recently gained attention in the joining research community. ML algorithms offer the capability to learn multivariate correlations from experimental data, enabling predictive modeling without requiring explicit physical equations. In the field of metal–composite joining, ML has been applied to a wide range of tasks including process parameter optimization, prediction of mechanical properties, defect classification, and joint morphology control. For instance, Liu et al. [18] established ML models to predict joint geometry and performance in self-piercing riveting processes, while Chen et al. [19] used ensemble learning to classify fracture modes in CFRP/steel bonded joints based on joint geometry. Despite their predictive power, conventional ML models often act as “black boxes,” making it difficult to extract physically meaningful insights from the learned relationships. This has limited their adoption in scientific studies where interpretability and mechanism understanding are essential. To overcome this barrier, recent research efforts have begun integrating ML with physical reasoning through two primary strategies: dimensionless group construction and model distillation. The first strategy involves transforming original process variables into dimensionless groups based on principles of physical similarity. By reducing variable dependency and eliminating unit scales, this approach enhances model generalization across different systems and provides variables that are more physically interpretable. The second strategy, model distillation, aims to extract simplified mathematical expressions from complex models such as decision trees or neural networks. These distilled models capture the essential trends and relationships in compact, human-readable form, thereby bridging the gap between data-driven learning and physics-based understanding. In this study, a unified data-driven framework is developed to investigate the process–structure–property relationships in hot-press joining of Al alloys and CFRTPs. By constructing physically meaningful dimensionless variables, training gradient boosted decision tree (GBDT) models, and applying model distillation techniques, this framework enables both accurate prediction and mechanistic interpretation of how thermal–mechanical conditions govern interfacial evolution and joint performance. The proposed approach not only facilitates process optimization but also contributes to the broader goal of establishing a generalizable methodology for dissimilar material joining based on interpretable, data-driven models.

1.5 Objectives of this study

This study aims to quantitatively investigate how thermal–mechanical conditions govern the interfacial evolution and mechanical performance of Al alloy/CFRTP hybrid joints. A physically stable and controllable hot-press platform is employed to simulate and observe the joining process under quasi-static conditions. Furthermore, a data-driven modeling framework is developed to capture the nonlinear correlations among process parameters, microstructural features, and joint strength, enhancing both predictive capability and physical interpretability. To achieve this aim, the research is structured into three interrelated phases. First, a hot-press joining platform is constructed to provide a controlled thermal–mechanical environment for studying interfacial phenomena in

Al/CFRTP joints. Second, high-resolution experimental data are combined with interpretable machine learning models to quantitatively capture the relationships among process conditions, interfacial structures, and joint performance. Third, the knowledge and models developed under idealized hot-press conditions are extended to a more complex and practically relevant joining method—friction spot joining (FSpJ)—to assess the transferability and applicability of the developed framework under dynamic joining environments. The specific objectives of this study are as follows:

- To construct and optimize a hot-press joining platform tailored for Al/CFRTP joints. This includes the initial process design, equipment development, and refinement of joining parameters. The goal is to systematically investigate how different combinations of temperature, pressure, and holding time affect interfacial chemical reactions, polymer flow behavior, defect formation, and joint mechanical integrity.
- To establish a quantitative relationship among joining parameters, interfacial microstructures, and mechanical performance using a combination of advanced experimental characterization (e.g., SEM, TEM, XPS, Raman, mechanical testing) and data-driven regression models. Special emphasis is placed on extracting physically meaningful features such as reaction layer thickness, void morphology, and interfacial bonding indicators.
- To implement an interpretable machine learning framework based on dimensionless group analysis and GBDT, enabling accurate prediction of joint strength and mechanistic understanding. Through model distillation, simplified mathematical expressions are extracted to explain how key thermal–mechanical inputs influence output performance.
- To extend the insights obtained from hot-press joining studies toward the investigation and potential optimization of other thermally assisted joining techniques, such as friction spot joining (FSpJ).

Based on these objectives, this thesis is organized as follows, and the integrated thesis flowchart is also shown in Fig. 1:

Chapter 2 describes the key experimental methodologies adopted throughout this research, including material preparation, composition of the hot press equipment, interfacial characterization techniques, and mechanical testing methods.

Chapter 3 investigates the influence of thermal conditions during hot-press joining on interfacial chemical reactions and fracture behavior. The evolution of the joint strength as a function of heating temperature and holding time is systematically analyzed, along with corresponding interfacial structural observations.

Chapter 4 explores the introduction of a controlled thickness hot-press joining strategy to systematically vary the pressure applied during joining. The combined effects of temperature, pressure, and heating time on the mechanical performance of the joints and on the interfacial microstructure are discussed in detail.

Chapter 5 establishes quantitative process–structure–strength relationships by extracting key influencing parameters and applying dimensionless analysis. Machine learning models are developed to predict joint performance based on process conditions, and interpretable mathematical models are distilled to provide physical insights into the joining mechanisms.

Chapter 6 extends the understanding gained from hot-press studies to the analysis of other thermally assisted joining processes. In particular, the influence of tool shoulder geometry on thermal behavior, interfacial formation, and mechanical performance in friction spot joining (FSpJ) is investigated to demonstrate the transferability of the developed methodologies.

Chapter 7 provides an overall summary of the research findings and methodologies presented in this dissertation, highlighting the key conclusions and future perspectives for multi-material joining technologies.

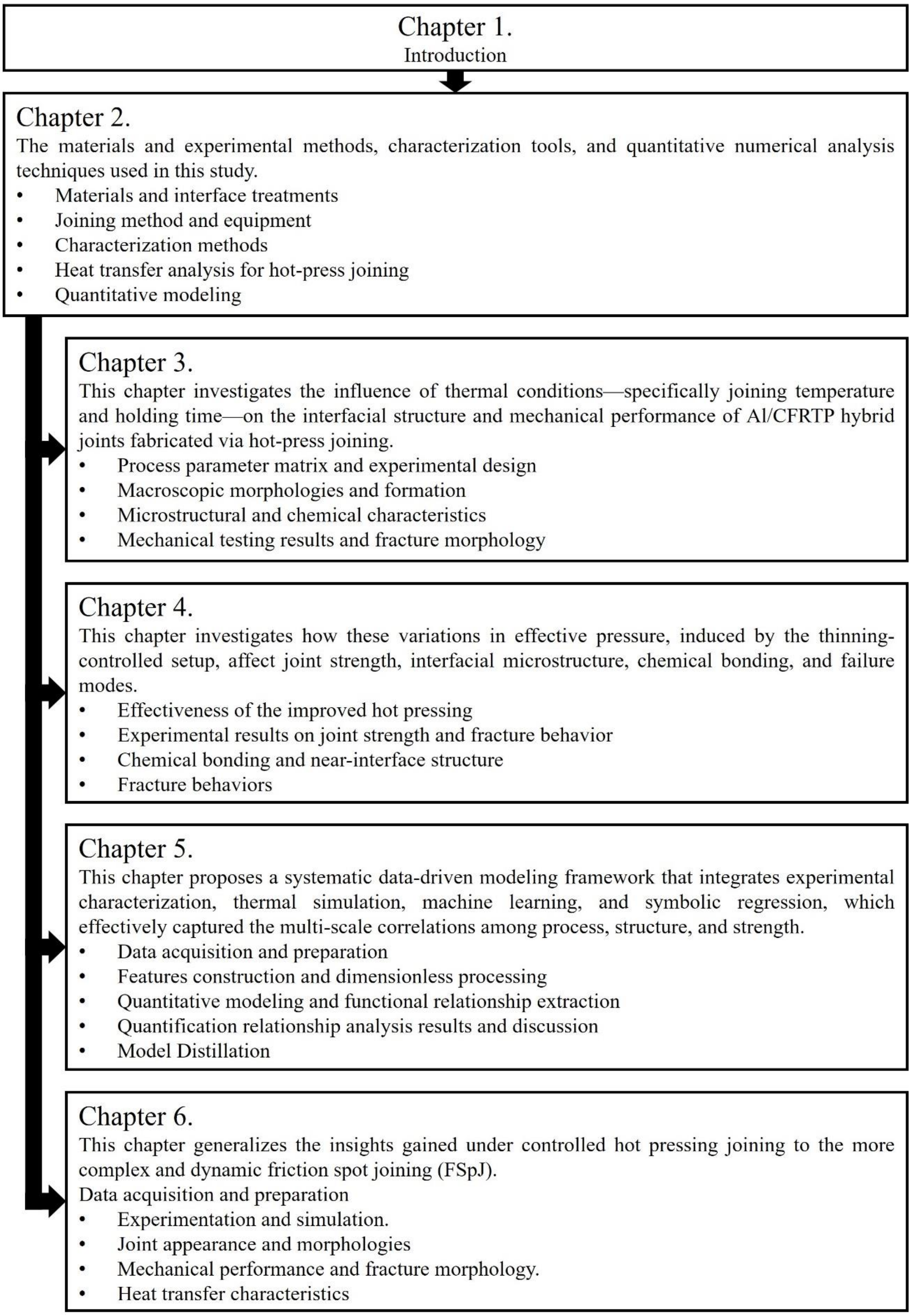

Chapter 1.

Introduction

Chapter 2.

The materials and experimental methods, characterization tools, and quantitative numerical analysis techniques used in this study.

- Materials and interface treatments
- Joining method and equipment
- Characterization methods
- Heat transfer analysis for hot-press joining
- Quantitative modeling

Chapter 3.

This chapter investigates the influence of thermal conditions—specifically joining temperature and holding time—on the interfacial structure and mechanical performance of Al/CFRTP hybrid joints fabricated via hot-press joining.

- Process parameter matrix and experimental design
- Macroscopic morphologies and formation
- Microstructural and chemical characteristics
- Mechanical testing results and fracture morphology

Chapter 4.

This chapter investigates how these variations in effective pressure, induced by the thinning-controlled setup, affect joint strength, interfacial microstructure, chemical bonding, and failure modes.

- Effectiveness of the improved hot pressing
- Experimental results on joint strength and fracture behavior
- Chemical bonding and near-interface structure
- Fracture behaviors

Chapter 5.

This chapter proposes a systematic data-driven modeling framework that integrates experimental characterization, thermal simulation, machine learning, and symbolic regression, which effectively captured the multi-scale correlations among process, structure, and strength.

- Data acquisition and preparation
- Features construction and dimensionless processing
- Quantitative modeling and functional relationship extraction
- Quantification relationship analysis results and discussion
- Model Distillation

Chapter 6.

This chapter generalizes the insights gained under controlled hot pressing joining to the more complex and dynamic friction spot joining (FSpJ).

Data acquisition and preparation

- Experimentation and simulation.
- Joint appearance and morphologies
- Mechanical performance and fracture morphology.
- Heat transfer characteristics

Fig. 1 The flowchart of this thesis.

2. Materials and Experimental Methods

To systematically investigate joining process for Al alloys and CFRTP, this chapter developed the joining apparatus, and analytical methods. A physically stable and repeatable hot-press platform was designed and manufactured to decouple thermal and mechanical factors in the joining process, enabling controlled exploration of process–structure–property relationships. Surface functionalization of the Al alloy was implemented using a silane coupling treatment to promote chemical bonding with the polymer matrix. Essential interfacial features such as bonding layer thickness, defect morphology, and chemical reaction states were characterized using SEM, XPS, and Raman spectroscopy. In addition, a finite element heat transfer model was constructed to simulate the temperature history at the joint interface, providing thermal descriptors that correlate with observed microstructural evolution. A data-driven modeling framework was also introduced, laying the groundwork for quantitative prediction and interpretation in subsequent chapters. This chapter is organized as follows:

Section 2.1 describes the materials and interfacial surface treatment.

Section 2.2 details the hot-press joining apparatus and joining procedure.

Section 2.3 introduces the experimental characterization techniques.

Section 2.4 presents the interface temperature modeling using finite element analysis.

Section 2.5 outlines the data preprocessing and regression modeling strategy.

2.1 Materials and interface treatments

The material system investigated in this study comprises Al alloys and carbon fiber reinforced thermoplastic composites (CFRTP), which serve as representative constituents of lightweight structural components in mobility applications. The metallic component consists of two industrial-grade Al alloys: A5052-O and A6061-T6. Both alloys belong to the 5xxx and 6xxx series, respectively, and are widely employed in automotive and aerospace sectors due to their favorable combinations of density, mechanical performance, corrosion resistance, and formability.

A5052-O is a non-heat-treatable wrought Al-Mg alloy that contains approximately 2.2–2.8 wt% magnesium and 0.15–0.35 wt% chromium. The “O” temper indicates a fully annealed state, resulting in the softest and most ductile condition for this alloy. This allows for excellent formability and deep drawability, which is advantageous for processing and deformation during joining. While the strength of A5052-O is lower than strain-hardened tempers such as H32, its high ductility and thermal conductivity make it an ideal choice for experimental joining studies that involve heat and pressure, as it allows for better plastic compliance and temperature uniformity during the process. A5052-O also exhibits exceptional corrosion resistance in marine and chemically aggressive environments, and is commonly used in fuel tanks, containers, and panel applications where formability is prioritized over strength.

A6061-T6, in contrast, is a heat-treatable Al alloy containing magnesium (0.8–1.2 wt%) and silicon (0.4–0.8 wt%) as principal alloying elements. The T6 temper refers to solution heat treatment followed by artificial aging, resulting in significantly higher tensile and yield strength than A5052. Despite its higher strength, AA6061 maintains excellent machinability and corrosion resistance. It is commonly employed in structural frames, extrusions, and load-bearing components. The different alloying systems and heat treatment responses of A5052 and A6061 provide valuable comparative insight into how alloy chemistry affects interfacial bonding behavior and joint strength when coupled with polymer-based counterparts.

The polymeric component in this study is a carbon fiber reinforced polyamide-6 (CF/PA6) thermoplastic composite, selected for its superior strength-to-weight ratio, toughness, and thermal and chemical stability. Polyamide-6 (PA6), also known as Nylon 6, is a semicrystalline polymer formed by ring-opening polymerization of ε-caprolactam. It features high polarity due to the presence of amide groups (–CONH–), which facilitate hydrogen bonding and enable reactivity with functionalized metal surfaces via coupling agents. Based on differential scanning calorimetry (DSC) and thermogravimetric analysis (TGA) results obtained in the previous study [11], the melting temperature (Tm) was around 220 °C, and the thermal decomposition was observed at approximately 340 °C for CF/PA6. Joining temperatures exceeding this threshold risk inducing matrix degradation, gas evolution, and interfacial void formation, which deteriorate joint strength. The composite formulation used in this study includes two fiber volume fractions (20% and 40%) and two fiber length regimes: short fibers (mean length 0.2~0.6 mm) and long fibers (mean length 0.6~2 mm). The properties and characteristics of the above materials at room temperature are shown in Table 1.

Table 1 Properties and characteristics of materials

Materials	Length of CF (mm)	Thickness (mm)	Tensile strength (MPa)	Young's Modulus (GPa)
A5052-O	\	2	204	72
A6061-T6	\	2	310	68.9
20% short CF/PA6	0.2~0.6	3	154	11.3
20% long CF/PA6	0.2~2	3	155	11.7
40% short CF /PA6	0.2~0.6	3	163	12.5

The surfaces of the Al alloy and CF/PA6 sheets were wet-grinded with 800# emery paper and dry-grinded with 240# emery paper for 10 min to attain uniform roughness. Then, the SCA surface treatment was applied on the overall overlap surface of Al alloy plate using OFS-6040 (3-Glycidoxypropyltrimethoxysilane, $C_9H_{20}O_5Si$), as shown in Fig. 2(a). In the distilled water, the methoxysilane ($-Si-COH_3$) in OFS-6040 was transformed into silanol (-Si-OH) and ethanol (CH_3OH) after a series of complex hydrolysis reactions. Subsequently, silanol was bonded to the hydroxide groups on the Al surface and dehydrated at a temperature higher than 120 °C to form Si-O-Al bonds, as shown in Fig. 2(b) and (c). The green spheres represent the functional groups on the silanol coupling agent that other substances can chemically activate. The amide groups at the end of PA6 in CFRTP can react with the epoxy groups in silanized Al surface at a certain temperature through an insertion reaction, which was applied in this study as a theoretical basis for the bonding of CFRTP and SCA. Subsequently, an additional reaction to replace the hydrogen in the amide group was realized, as shown in Fig. 2(d).

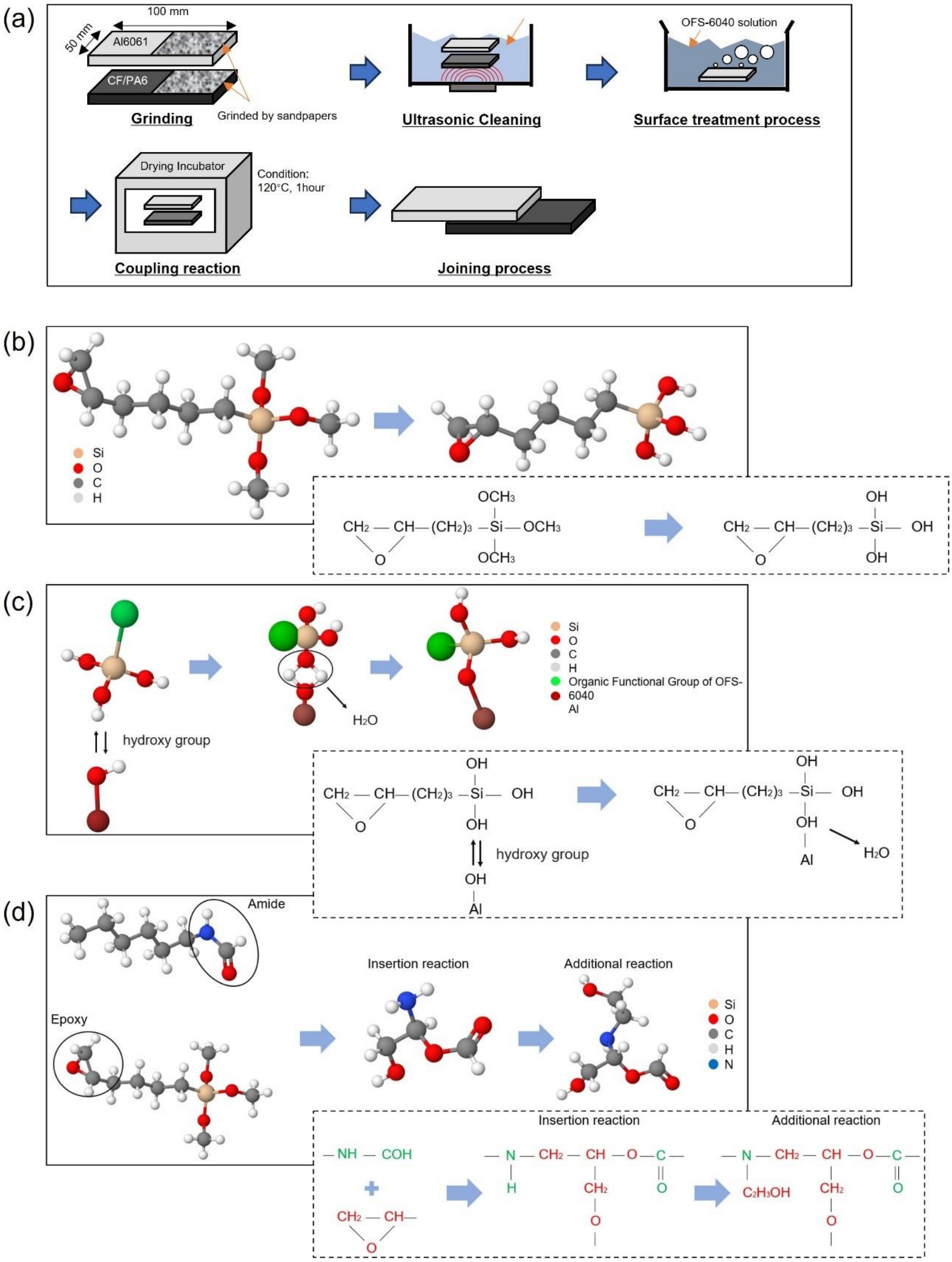

Fig. 2 Schematic of the (a) preparation process for joining sheets, (b) Hydrolysis transformation mechanism between methoxysilane and silanol in distilled water, (c) Bonding mechanism between the SCA and original Al surface, and (d) Insertion and

additional reactions between amide groups in CF/PA6 and epoxy groups in silanized Al surface.

2.2 Joining method and equipment

Al alloy and various CF/PA6 sheets were hot-pressed together using our custom-designed constant-temperature hot-pressing apparatus, as shown in Fig. 3(a). Temperature and loading force were controlled using a direct heating system at the bottom and a pneumatic pump actuator system at the top, respectively. In the system, the different download generated by the pressure plate are realized by adjusting the amount of compressed air into the cylinder. In addition, we use a down pressure control block to adjust the gap between the pressure plate and the heating plate, through which the movement of the loading pressure was controlled. As shown in Fig. 3(b), at the beginning of the experiment, the fixing of top side CFRTP sheet contact intimately with the upper pressure plate by air-pressure suction (shown in Fig. 3(a)) from the several holes inside the pressure plate. The Al alloy sheet was accurately pre-positioned on the top surface of a copper heat-conductive plate using distance instrument before joining, which was heated using a nickel alloy resistive heating element in contact with the heat-conductive plate. Once the Al sheet reached a steady temperature, the CFRTP sheet was moved with the downward pressure plate and then maintained lap contact on the Al alloy sheet. After a certain heating time, the heat source was removed and the lap-joined Al/CFRTP on the heat-conductive plate was cooled in an air environment. To control the thinning displacement, the pressure plate was stopped and maintained at its current position when it reached the specified stroke.

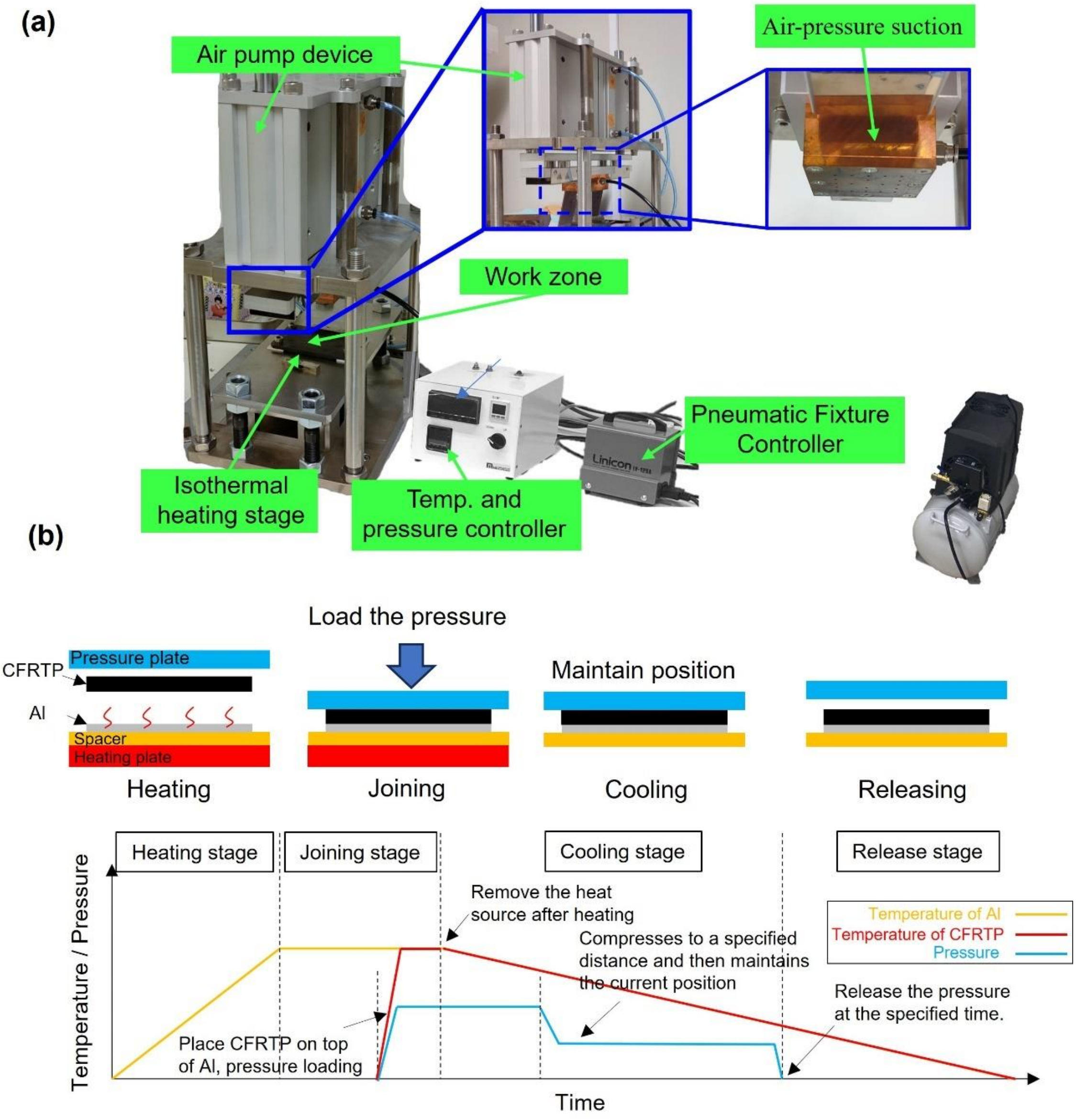

Fig. 3 The illustration and schematic of (a) Hot pressing machine, (b) Process of isothermal-pressing joining.

2.3 Characterization methods

To evaluate the changes in the organic compounds at the interface and analyze the chemical reactions, XPS analysis was conducted with JPS-9010MX using a 100 W Al-Ka X-ray source. Furthermore, to identify the variations in the organic compounds at the Al/CFRTP interface, Raman spectroscopy was performed using a HORIBA LabRAM

ARAMIS instrument with a 532-nm laser light source. Thermocouples were used to measure the temperatures of the joints, and the locations of the measurements are shown in Fig. 4(a).

The mechanical properties of the bonded Al/CFRTP joints were evaluated by a tensile shear test conducted at ambient temperature (approximately 20 ℃) and a rate of 1 mm/min using a universal testing machine (SHIMADZU AGSX). As shown in Fig. 4(b), two shims were used to mitigate the effects of rotational asymmetry along the central axis on the mechanical properties. The clamping position of the tensile machine grippers are located 5mm from the weld overlap area and kept the same for all tensile test specimens in the experiment. Force–displacement curves were derived from the tensile–shear tests, with the maximum tensile–shear force averaged across multiple specimens. Observations of the macroscopic fracture surfaces and cross sections of the Al/CFRTP joints were conducted using optical microscopy and scanning electron microscopy (SEM, HITACHI SU70).

(a)

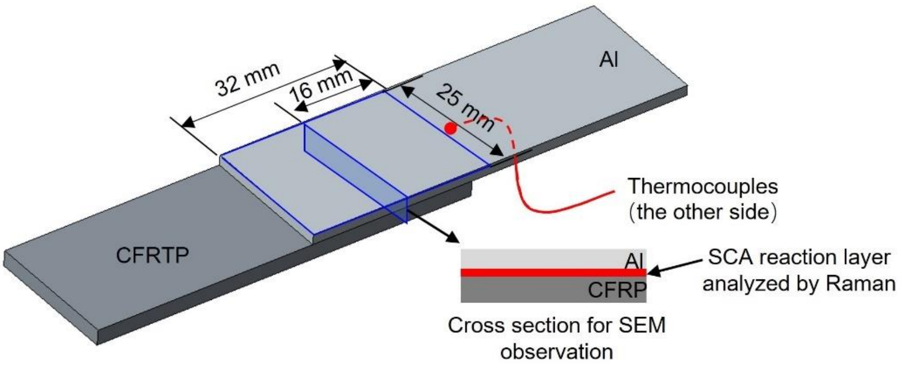

(b)

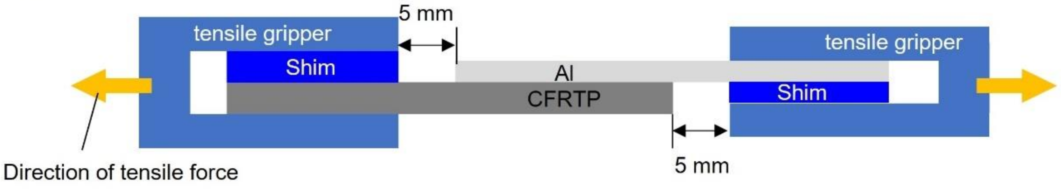

Fig. 4 Schematic of (a) the positions for optical observation and Raman analysis, and (b) the lap tensile shear experiment.

2.4 Heat transfer analysis for hot-press joining

The duration time of interface temperature higher than the melting point was significant, impacting the completeness of the chemical reaction between silane film and molten polyamide. In the current investigation, a simplified heat transfer model was developed based on the commercial finite element analysis (FEA) software Abaqus to predict temperature histories. It would help better understand the effects of different joining temperatures on interface bonding strength in isothermal-pressing joining. Fig. 5 shows the information on the FEA model. The fine mesh size of ~0.1 mm, which was proven to be sufficiently accurate to predict interface temperature according to the preliminary mesh size sensitivity analysis, was applied to the region close to the Al/CFRTP interface due to the large temperature gradient. A constant heat transfer coefficient of 20 W/(m^2·K) was used to calculate the heat loss in the air environment. A higher heat transfer coefficient of 200 W/m^{2}K was applied to the bottom of Al surface after 2 s of the end of the heating stage because the joined Al/CFRTP was placed on the steel test bench and cooled to the room temperature of 20 ℃. According to the research study of thermal contact conductance between metals and polymers by Sridhar et al. [20], a simplified constant value of 2000 W/(m·K) was determined in this model based on the temperature comparison with experiment measurement. The thermal parameters of the materials used are as Table 2.

Table 2 Properties and characteristics of two workpiece materials

Materials	Thermal Conductivity (W·m^{-1}·K^{-1})			Specific Heat (J·g^{-1}·K^{-1})		
	20℃	100℃	200℃	20℃	100℃	200℃
Al 5052		150			1.0	

CF/PA6	0.4	0.43	0.51	1.31	1.95	2.86

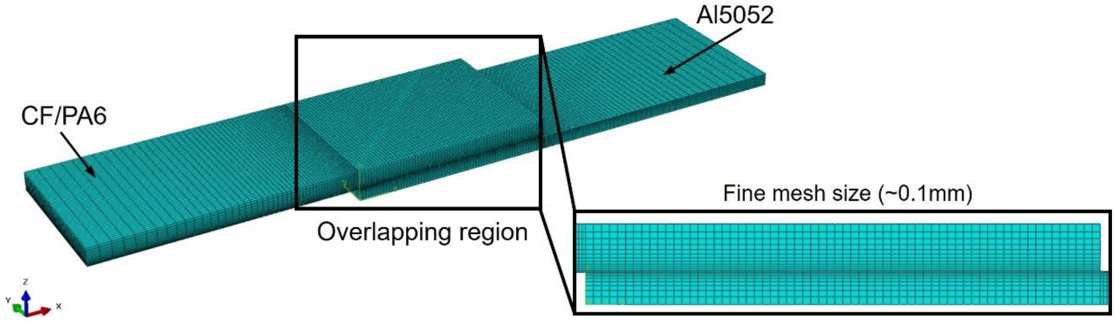

Fig. 5 Schematic diagram showing heat transfer model of isothermal-pressing joining arrangement between Al and CF/PA6.

2.5 Quantitative modeling

The GBDT method was used to construct three types of quantitative relationship between models: mapping of process conditions to microstructure features, mapping of microstructure features to mechanical properties, and direct mapping of process conditions to mechanical properties, respectively. The model performance is evaluated through the metrics of the coefficient of determination (R^2), mean squared error (MSE) and mean absolute error (MAE) on the training and test sets. The formulas for MSE and MAE are given below:

$$MSE = \frac{1}{n}\sum_{i=1}^{n}(y_i - \hat{y}_i)^2 \quad (1)$$

$$MAE = \frac{1}{n}\sum_{i=1}^{n}|y_i - \hat{y}_i| \quad (2)$$

Also, generalization capability analysis is performed to ensure the model's adaptability beyond specific parameters. Additionally, key factors affecting various response variables are identified through feature importance analysis. The key factors will be used to analyze the physical relationship between process parameters-microstructure-mechanical properties.

As illustrated in Fig. 6(a), generalization capability analysis is performed to ensure the model's adaptability beyond specific parameters. Additionally, key factors affecting various response variables are identified through feature importance analysis. The key factors will be used to analyze the physical relationship between process parameters-microstructure-mechanical properties. To address the “black box” problem of GBDT models in terms of interpretability, the study further introduces a model distillation strategy to extract simplified function expressions from the original prediction models. The correlation and interpretability analyses between features were first performed to eliminate redundant variables and simplify inputs as shown in Fig. 6(b). Subsequently, the mathematical expressions are extracted by fitting the functional relationships between key features and compared with the original GBDT model to improve the accuracy, thus enhancing the engineering applicability and theoretical value of the model.

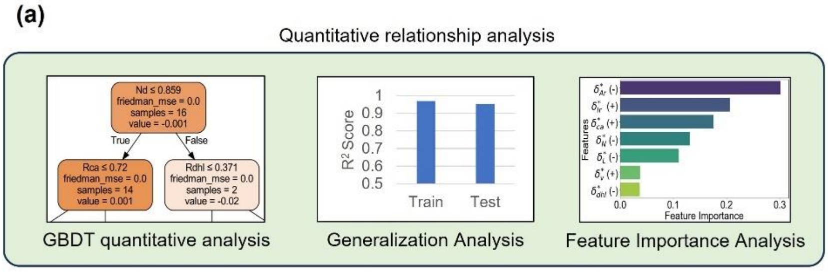

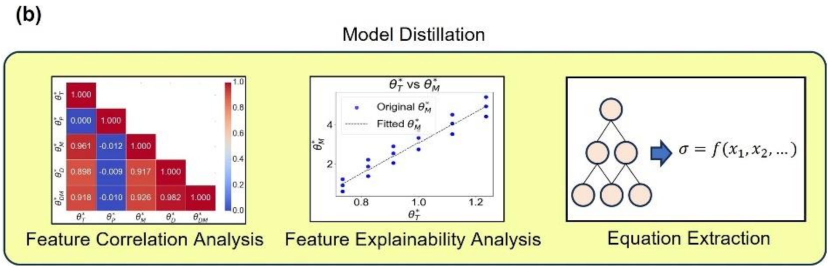

Fig. 6 (a) Quantitative modeling and (b) model distillation.

3. Hot-press joining mechanisms, microstructures, and properties under various thermal-mechanical conditions

This chapter investigates the influence of thermal conditions—specifically joining temperature and holding time—on the interfacial structure and mechanical performance of Al/CFRTP hybrid joints fabricated via hot-press joining. While the previous chapter outlined the experimental setup and materials used in this study, the present chapter focuses on the relationship between thermal input and the evolution of bonding mechanisms at the joint interface.

In hot-press joining, temperature plays a crucial role in controlling the softening and flow behavior of the thermoplastic matrix, promoting interfacial contact and chemical interactions. To evaluate how thermal history governs joint formation, a series of experiments were conducted under different heating conditions. Tensile-shear testing was employed to quantify mechanical performance, while optical and scanning electron microscopy (SEM) were used to observe fracture morphology and joint integrity. In addition to mechanical evaluation, this chapter also emphasizes microstructural and chemical characterizations of the joint interface. Raman spectroscopy and X-ray photoelectron spectroscopy (XPS) were employed to detect chemical bonding states. The morphology and thickness of the reaction layer were further examined using SEM and transmission electron microscopy (TEM), providing direct evidence of thermal-induced interfacial reactions. These analyses offer insights into the chemical bonding mechanisms and help to clarify how thermal input influences joint formation at the microscopic level. Overall, the findings in this chapter aim to uncover the fundamental thermo-chemical interactions occurring at the Al–CFRTP interface under varying thermal conditions, thereby laying the groundwork for controlled interface engineering in joining. This chapter is organized as follows:

Section 3.1 describes the process parameter matrix and experimental design.

Section 3.2 describes the macroscopic morphologies and formation of the joint.

Section 3.3 analyze the microstructural and chemical characteristics of the joint interface.

Section 3.4 presents the mechanical testing results and fracture morphology.

Section 3.5 summarizes the key findings and highlights their implications for the next chapter.

3.1 Process parameter matrix and experimental design

To investigate how thermal joining conditions to influence the interfacial evolution and mechanical performance of Al- CF/PA6 joints, a controlled process parameter matrix was designed. In this study, the hot-press joining platform developed in Chapter 2 was employed to ensure a stable and reproducible joining environment, enabling the isolation of thermal effects under constant mechanical boundary conditions. Given the thermo-sensitive nature of PA6, whose melting point is approximately 220 °C and decomposition temperature is around 380 °C, the joining temperature was selected in the range of 240°C to 300°C. This range was chosen to ensure sufficient polymer flow and interfacial wetting, while avoiding thermal degradation. Meanwhile, joining time was varied from 1 s to 3 s, which was sufficient to allow chemical reaction initiation and partial diffusion at the interface, based on preliminary trials. During all joining trials, the applied pressure was maintained constant at 0.2 MPa, and the heating interface was kept isothermal by the direct-contact resistive heating system described in Section 2.2.

The custom-designed hot-press apparatus ensured precise positioning and thermal pre-conditioning of the aluminum sheet before CF/PA6 placement. The CF/PA6 sheet was held in place by a vacuum suction mechanism on the upper platen, allowing a clean, uniform downward movement during pressing. The lap area was defined as 25 × 32 mm^2, consistent across all samples. To limit additional variables, both materials were joined in a single-lap configuration with fixed stacking order (Al on bottom, CF/PA6 on top), and all specimens were processed using the same equipment settings except for temperature and time. The thermal conditions are summarized in Table 3. For each temperature-time combination, three replicate specimens were prepared to ensure statistical reliability. These selected process conditions are expected to affect both the interfacial bonding mechanisms (e.g., chemical reaction extent, wetting, defect formation) and the final joint strength, which will be systematically evaluated in the following sections.

Table 3 Thermal conditions

Thermal condition	Values
Joining temperature (℃)	240, 270, 300
Residence time (s)	1, 2, 3

3.2 Macroscopic morphologies and formation

The macroscopic morphologies of Al-CF/PA6 at different joining temperatures and joining times are shown in Fig. 7(a). After isothermal-pressing joining, no inclination of the CFRTP matrix in the overlapping area existed for each condition, suggesting the flow and extrusion of molten resin were relatively uniform in the process. There were no obvious visible macro-defects from the overlapped edge and lapped interface for the studied conditions. The molten resin of the CF/PA6 flowed sufficiently during the process, and significant outflowed resin was re-solidified outside the overlapping region at higher joining temperatures and residence times. As a result, this reduced the thickness of CF/PA6 in the overlapping area. As shown in Fig. 7(b), the average thinning ratio of the CF/PA6 thickness was measured from the cross-section. The thickness reduced as the joining temperature or time increased. This introduced some negative factors for the Al-CF/PA6 bonding, such as extensively damaging the CF/PA6 substrate or reducing the integral load-bearing capacity of the lapped region. The thinning of the CF/PA6 substrate was due to the extrusion of the molten-state resin under the applied pressure.

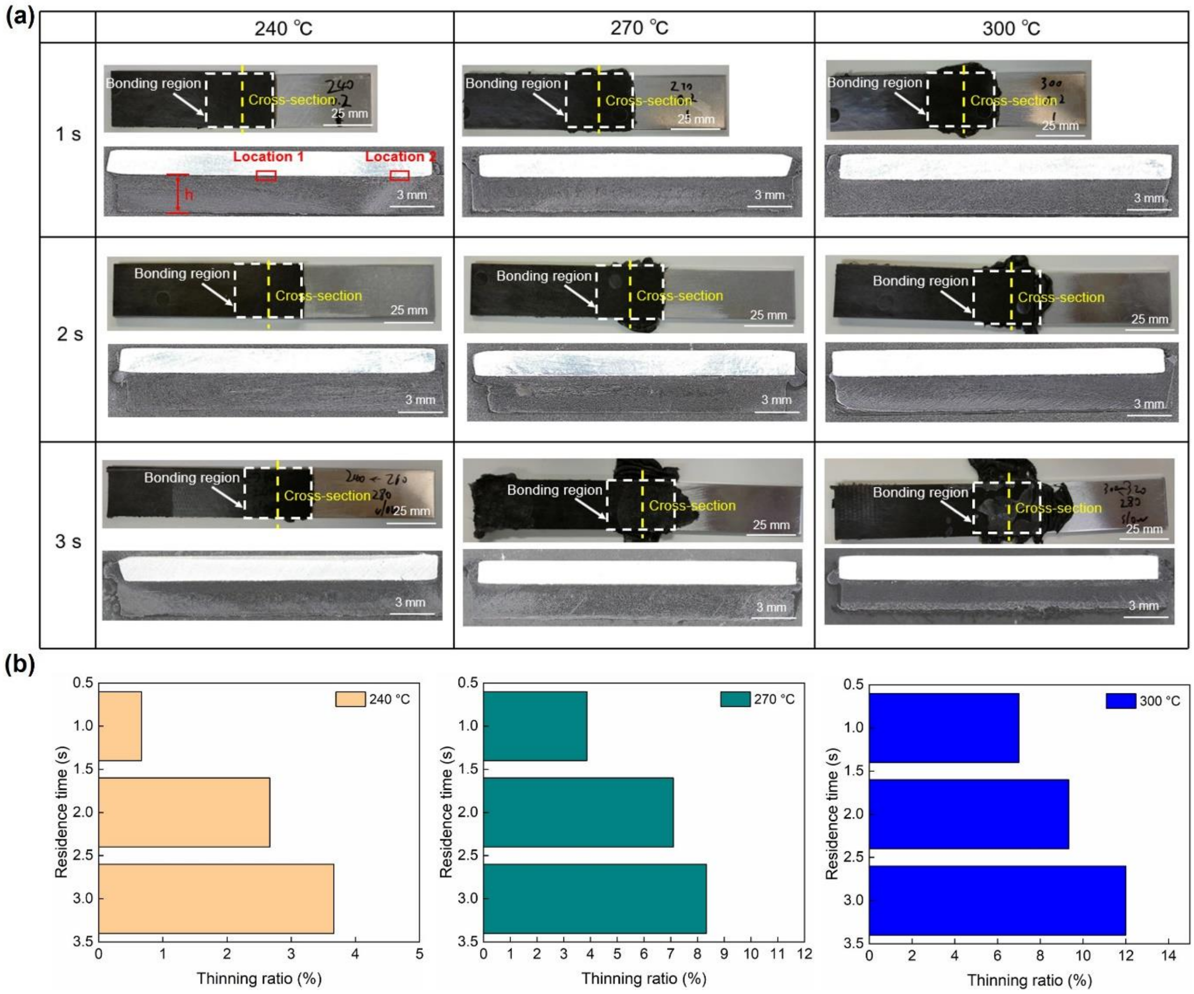

Fig. 7 Macroscopic morphology of Al5052/CFRTP joints produced at residence times of (a) 1 s, (b) 2 s, (c) 3 s at three different joining temperatures, and (d) thinning ratio of CFRTP sheet at different conditions.

The illustration presented in Fig. 8 displays the predicted temperature histories at various points along the Al/CFRTP interface during the joining process, where the joining temperature ranges from 240 ℃ to 300 ℃ and the residence time is fixed at 3 seconds. Fig. 8(a) illustrates the temperature distribution at the center of the Al/CFRTP contact surface, along the length of the specimen. The thermal conductivity of Al being greater than that of CF/PA6 (as indicated in Table 2), resulted in uneven heat dissipation in the lengthwise direction, where the temperature was observed to be higher near the Al side (at position N5) as compared to the position far from the Al side (at position N1) at the same instance. On the other hand, Fig. 8(b) highlights that the temperature distribution was uniform in the direction perpendicular to the length. Fig. 8(c) shows a half-overlapping cross-section at welding temperatures of 240 ℃, 270 ℃ and 300 ℃ with a residence time of 3s. At the Al/CFRTP boundary, the lateral flattening of carbon fibers was observed, which could be attributed to the deformation of the carbon fibers resulting from the high temperature melting and outflow of PA6. The temperature prediction results further indicated the presence of a thin layer of high temperature at the Al/CFRTP boundary. Fig. 8(d) compares the thickness of the high-temperature zone from the experimental results (represented in blue) and the temperature prediction (represented in orange). The predicted thickness of the high-temperature zone (in orange) appears to be slightly greater than the actual thickness, as the prediction model did not take into account the thickness variation caused by material flow. However, the results show a satisfactory degree of consistency. The temperature history curve of the joining interface was measured by implanting a thermocouple on the surface of CF/PA6 near the Al edge (as N1 in Fig. 8(a)) during the actual joining process. The comparison between the simulated model temperature and the experimental results is also depicted in Fig. 8(e), indicating good agreement between the two.

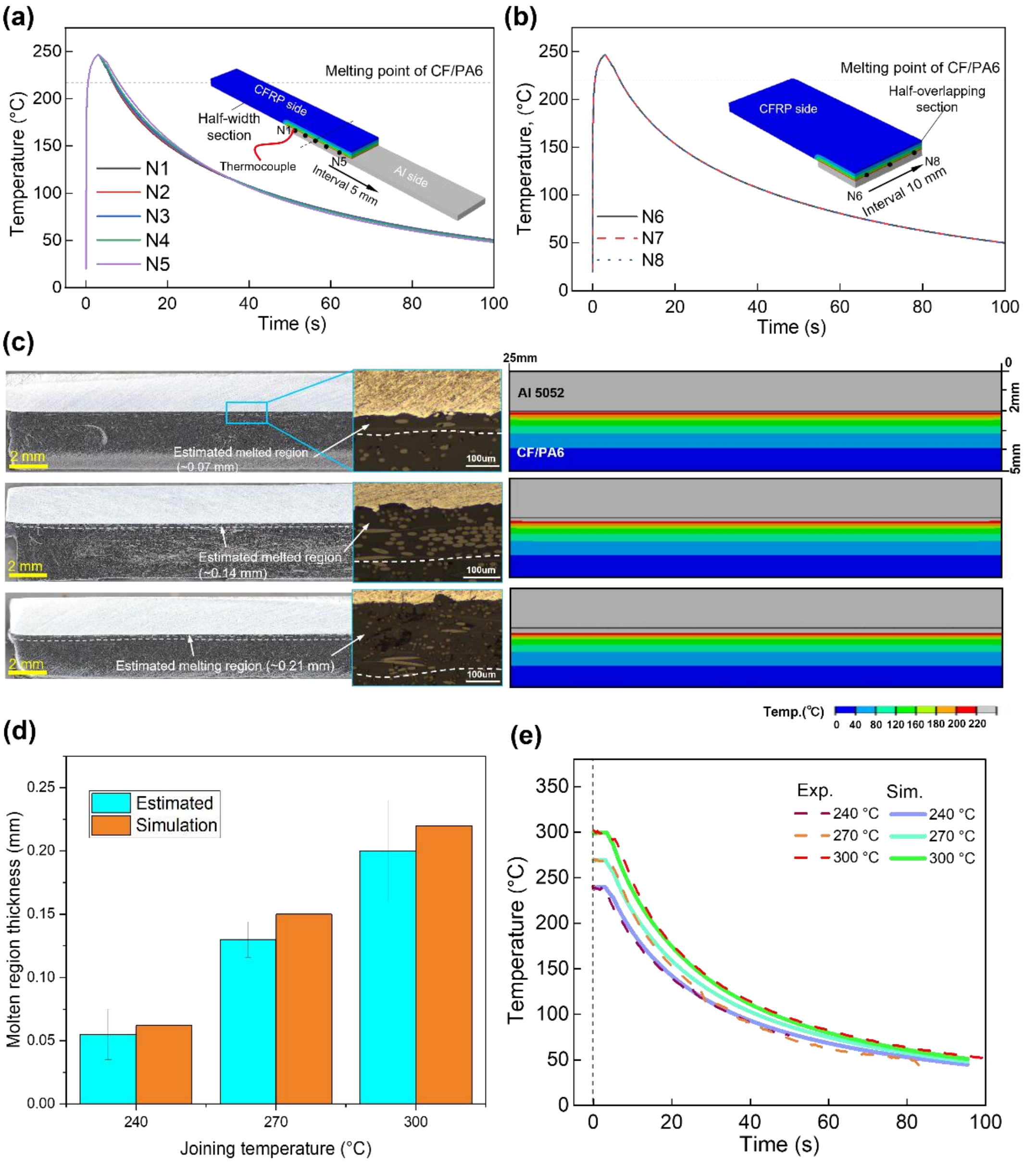

Fig. 8 (a) The temperature history prediction curves along the length direction and (b) along the perpendicular to the length direction, the experimental and predicted (c) half-overlapping cross-section, and (d) predicted high-temperature layer thicknesses and (e) temperature history curves of N1 position shown in Fig. 8(a).

Fig. 9 shows the distribution of high-temperature duration time at each position (as shown in Fig. 8(a)) for varying joining temperatures and times. The melting point of PA6 (220 °C) serves as the reference for high temperatures. As indicated in Fig. 9, the high thermal conductivity of Al leads to a prolonged high-temperature residence time near the Al side, regardless of the joining conditions. Furthermore, with an increase in either the joining temperature or the joining time, more heat is transferred to the Al/CFRTP boundary, leading to an extended high-temperature duration time.

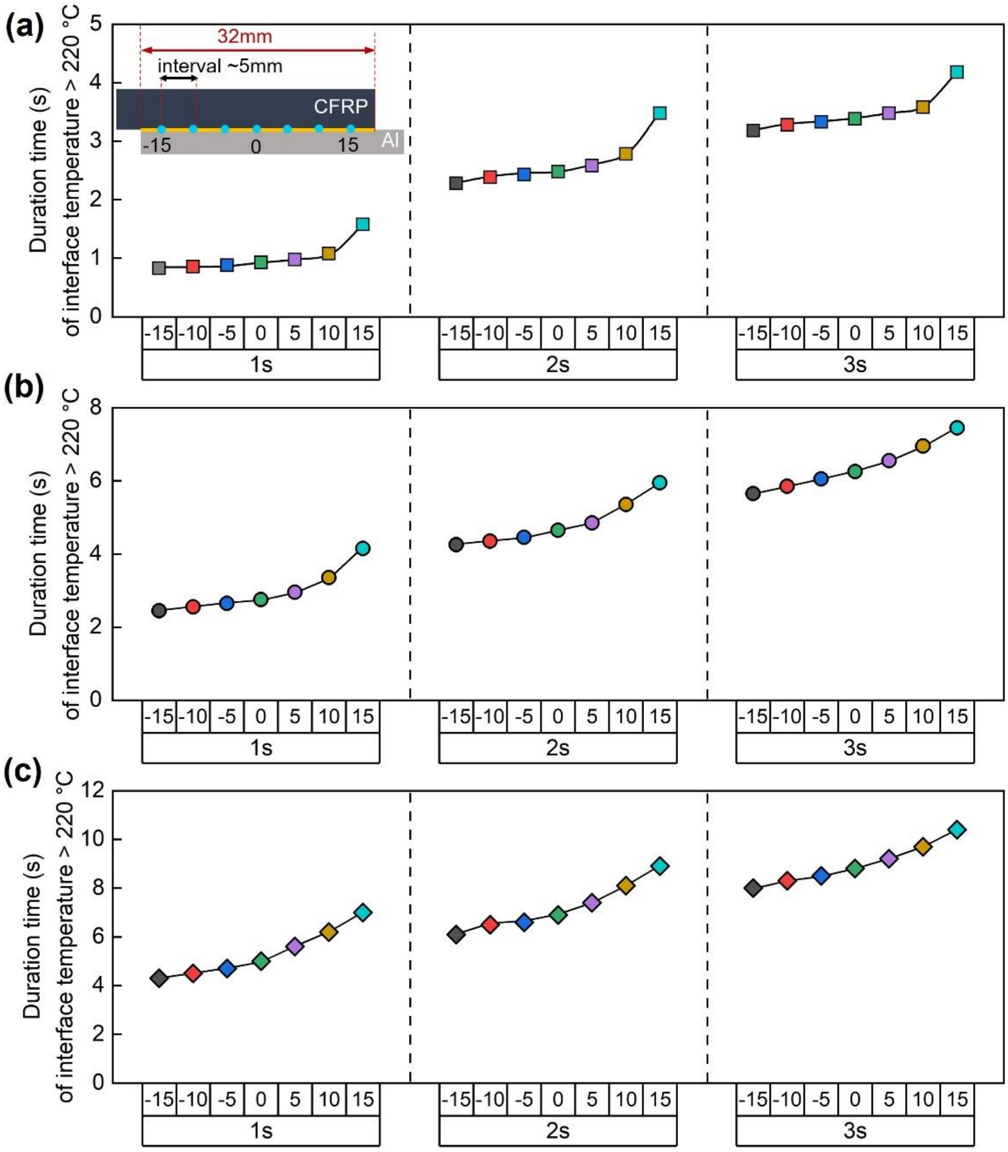

Fig. 9 Predicted duration time of Al/CFRP interface temperature (higher than 220 °C) at different locations in different joining conditions of (a) 240 °C, (b) 270 °C, and (c) 300 °C.

3.3 Microstructural and chemical characteristics

SEM images of the interface morphology of the Al/CFRTP joint and elemental diffusion under different conditions are shown in Fig. 10. The observed locations were at the center (location 1) and outside (location 2), as shown in Fig. 7(a). The Al surface exhibits grooves and protrusions for each condition owing to its original roughness, rendering micro-mechanical interlocking of the Al/CFRTP joining. Moreover, Al and CFRTP are bonded tightly due to the molten resin flowing into the grooves on the Al surface. Under the adopted joining conditions, no pores or bubbles induced by the thermal decomposition of molten resin were found in the overall bonded interface of the joint, even those with the highest temperature and longest residence time. Additionally, carbon fibers seemed to concentrate slightly at the bonding interface due to the excessive molten resin ejection during the process, which may adversely affect the interfacial strength. This phenomenon could be improved by reducing the pressure and interface temperature. As shown by the red arrows in Fig. 10(a), it is worth noting that some micro-porosities existed at local regions of re-solidified resin close to the interface at the highest temperatures (300 °C) or the highest residence times (3 s). From the micro-morphologies, these micro-porosities formation might be attributed to the local uneven cooling shrinkage of the molten resin. Fig. 10(b) shows the EDS line scanning results at the center location. The Al and C elements on both sides changed abruptly across the interface area. The distribution of the Si element well reflected that the thickness of the joined interface was in the micron or even nanometer scale, approximating 1~2 μm from EDS results.

Further TEM analysis of the Al/CFRTP interface is shown in Fig. 11. Fig. 11(a) exhibited the sampling position of the TEM specimen using Focused Ion Beam (FIB) technology. In Fig. 11(b), a significant silane coupling layer (SCL) of ~1 μm thickness existed between Al alloy and CF/PA6. The SCL was well attached to the Al and CFRP sides, and no micro defects existed, as shown by a local high-magnified view in Fig. 11(c). The selected area diffraction (SAD) at the position marked by the white arrow in Fig. 11(c) indicated the diffraction characteristics of the amorphous layer for SCL. Across the interface, the EDS line scanning in Fig. 11(d) proved that the chemical reaction zone for the interfaces between Al oxidation and SCL and between SCL and re-solidified resin occurred within the area of less than ~100 nm, revealing the molecular scale bonding. In addition, the Al and C elements form a transition at the Al surface, where the concentration of O elements was slightly higher than that in the SCL, suggesting an oxidation film on the Al surface. The ratio of the atomic numbers of O and Al was approximately 1:3, which implied that the oxidation might be Al_3O [21]. Fig. 11(e) shows the dark field TEM image and SAD of the Al surface. There were many scattered spots around the central spot in the diffraction spot distribution of the Al surface, indicating the possible presence of aluminum oxides. In contrast, the dark-field TEM image and SAD of the internal Al matrix in Fig. 11(f) showed a regular arrangement of the diffraction spots.

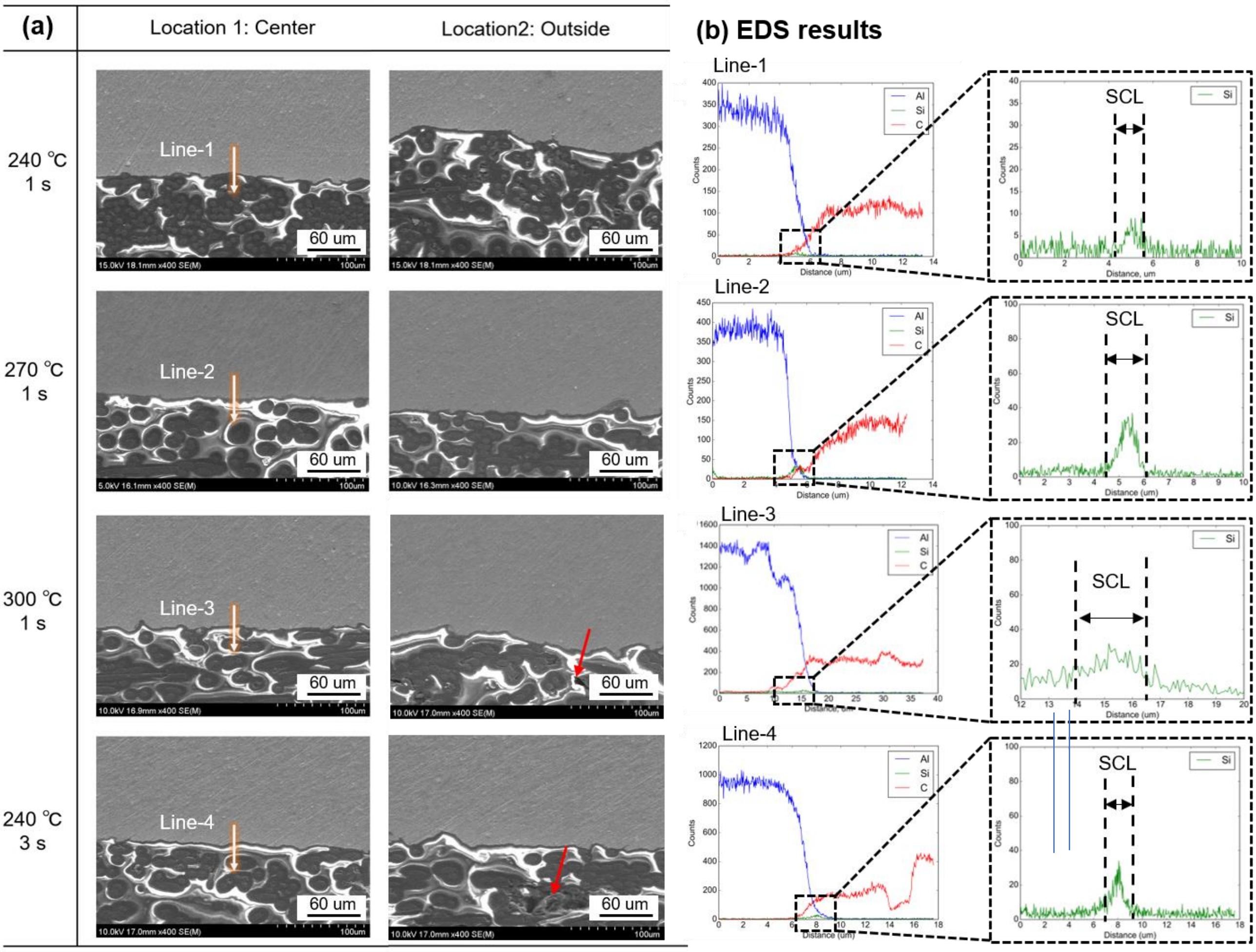

Fig. 10 SEM and EDS analysis of Al/CFRTP interface: (a) micro cross-sectional morphology and (b) the main elements distribution along the lines marked in Fig. 10(a).

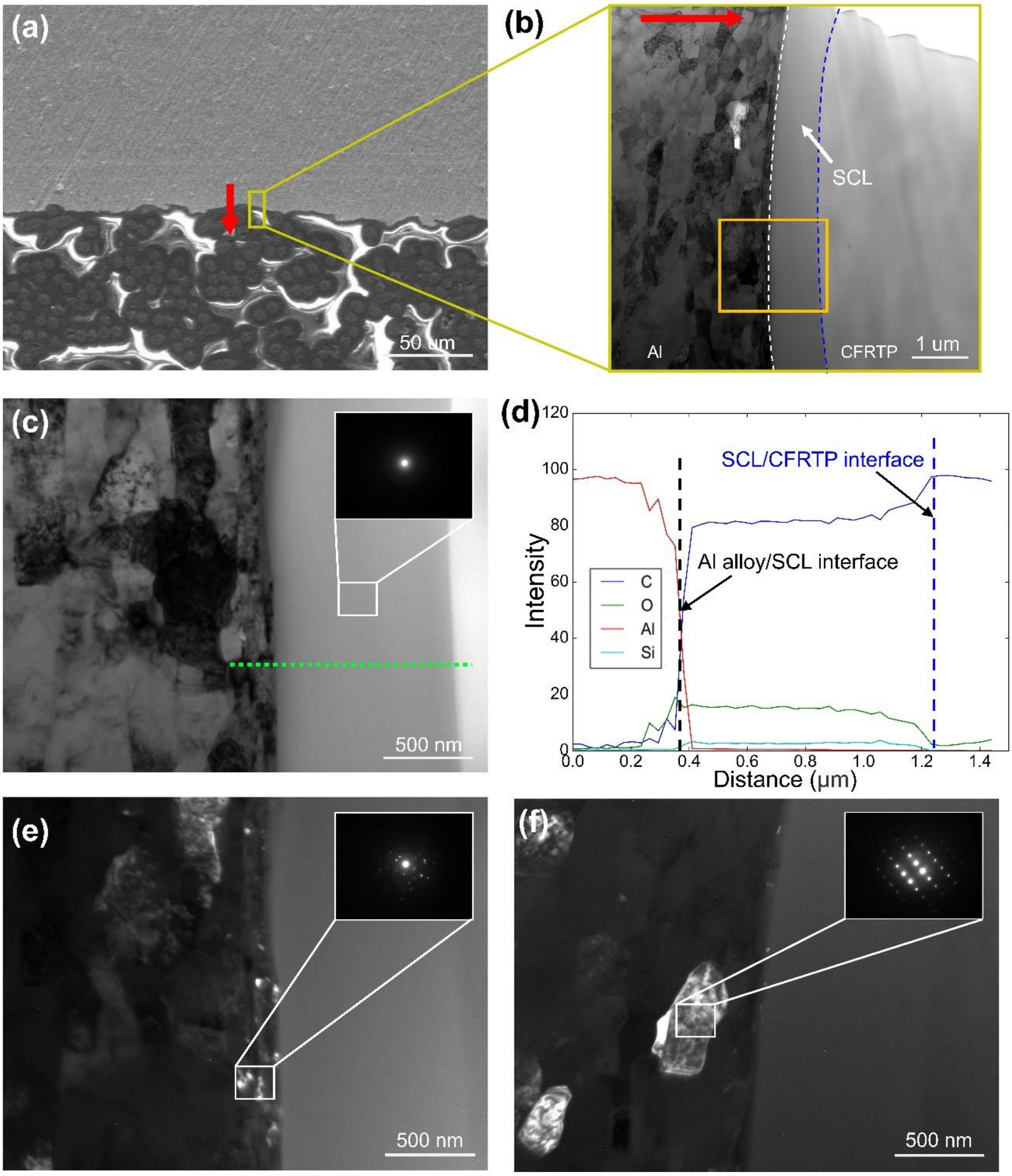

Fig. 11 Details of TEM analysis for lapped Al/CFRTP interface obtained by the condition of 240 °C and 1 s: (a) FIB sampling position of TEM observations, (b) TEM image of Al/CFRTP interface, (c) Local high-magnified view of the rectangular region marked in Fig. 11(b), (inserted image showing selected area diffraction (SAD) marked by white arrow), (d) TEM-EDS linear scanning analysis of the location marked by the green dotted

line in Fig. 11(c), (e) Dark field TEM image and SAD of the Al alloy surface, and (f) Dark field TEM image and SAD of the Al alloy.

Raman spectroscopy was used to quantify the chemical reactions at the Al/CFRTP bonded interface. Based on the reaction principle shown in Fig. 2, the epoxy group in the SCL was consumed through an insertion reaction with the amide group in the PA6. Therefore, this study used the epoxy group content as a quantitative criterion to evaluate the chemical reaction state. To reduce the influence of stray light and instrument noise on the experimental results, we developed a script in Python based on the open-source modules RAMPY and LMFIT to correct the tilt of the Raman spectrum and perform the split-peak fitting. Fig. 12(a) compares the Raman spectrum distribution between the CFRTP and the Al/CFRTP interface under different residence times with a joining temperature of 240°C processed by the above script. The results for the bonding interface were averaged over several points at the interface. Table 4 lists the chemical bonds corresponding to each frequency shift peak. Since the matrix of the studied CFRTP was PA6, the Raman spectrum of CFRTP emerged predominantly from various carbon chain components [22]. In addition, an amide was attached to the PA6 end of the CFRTP, and the Amide III peak (N-H stretching vibration) and Amide I peak (C=O stretching vibration) were observed at 1242 cm^{-1} and 1656 cm^{-1} in the Raman spectrum, respectively [23]. Since the bonding interface of Al/CFRTP was relatively thin, the distribution of its Raman spectrum was affected by the surrounding CFRTP matrix. Thus the Raman peaks of the CFRTP matrix were also included in the results of the bonding interface. The Raman spectrum distribution at the bonding interface had peaks at 520 cm^{-1} and 780^{-1}, representing Si and epoxy, respectively [24–26], whereas the Raman spectrum of the CFRTP matrix did not have these two peaks. Regardless of the changes in the joining conditions, the concentration of Si in the SCL did not change throughout the reaction; therefore, the Raman peaks of Si under different joining conditions showed similar intensities. In contrast, the Raman spectrum intensity of the epoxy varied with the joining conditions due to the different completeness of the chemical reaction, resulting in different residual amounts of epoxy. To accurately quantify the extent of the chemical reaction, the Raman spectrum intensity ratio of epoxy to Si in Eq. (3) was used to represent the relative epoxy concentration (similar techniques have been reported in [27–29]).

$$\Delta c = \frac{i_{epoxy}}{i_{Si}} \tag{3}$$

where, Δc represents the relative concentration of epoxy. i_{epoxy} represents the Raman intensity of epoxy, and i_{Si} represents the Raman intensity of Si. The variation in the relative concentration of epoxy under different joining conditions was statistically calculated, and the statistical and distributional results are presented in Fig. 12(b), where the transition periods between each joining condition were expressed using linear interpolation. Increasing the joining temperature or extending the residence time caused a decrease in the relative concentration of epoxy, which might represent the chemical reaction more complete. Moreover, the variation in the relative concentration of epoxy tended to be smooth after temperature and time increased to a certain extent, possibly because the chemical reaction had fully completed between the SCA and the PA6 of molten resin.

Table 4 Raman frequency shift peaks of key constituents.

Chemical bonding	Raman shift (cm^{-1})
C-C, CH2, CH3	1000-1500 [22]
Amide I	1242 [23]
Amide II	1656 [23]
Si	520 [24]
Epoxy	780 [25,26]

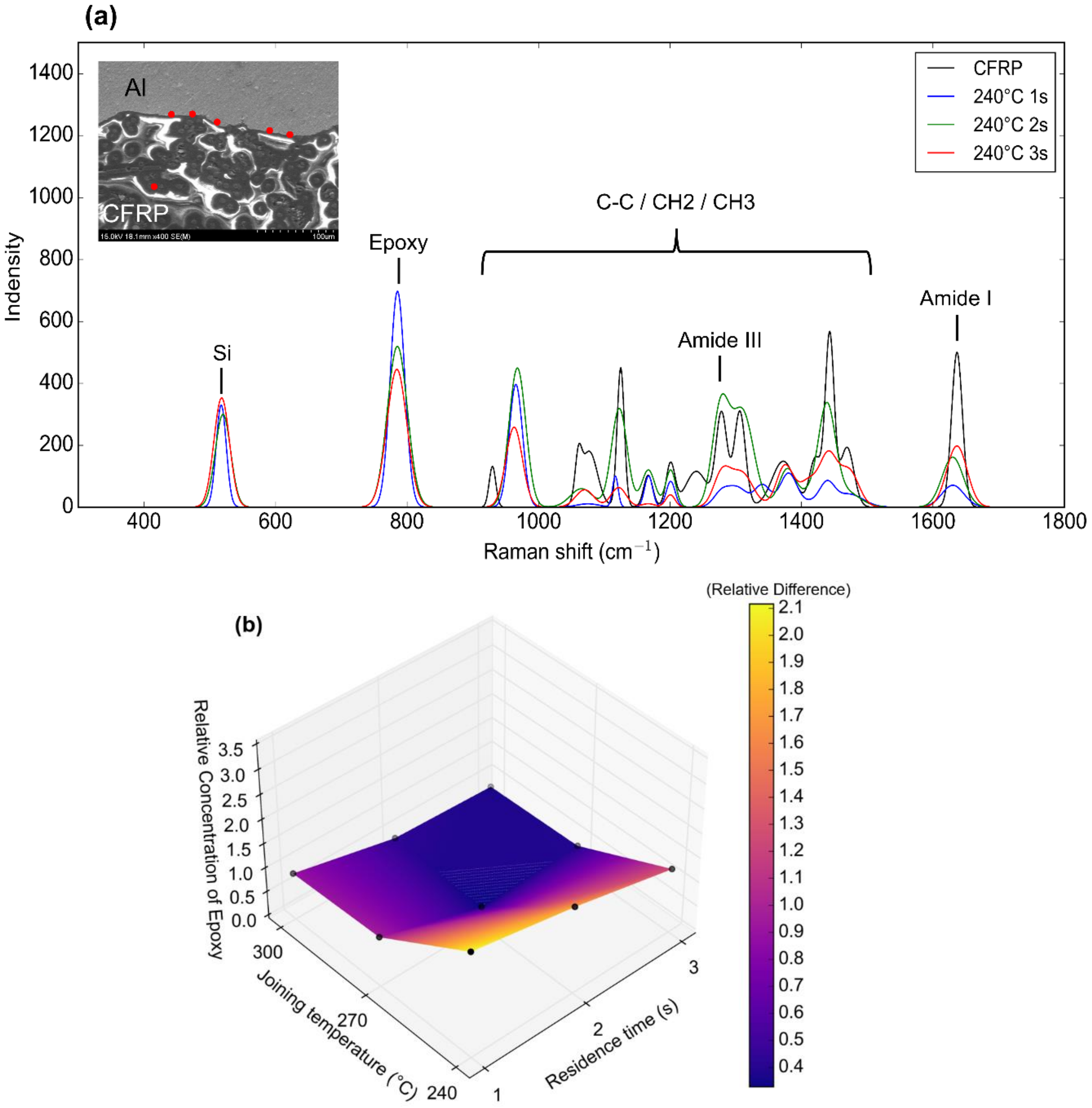

Fig. 12 (a)The typical Raman spectrum distribution of the CFRTP and the bonding interface of Al/CFRP under different residence times at 240 °C and (b) Plotted map showing the relative concentration of epoxy of different joining conditions.

3.4 Mechanical testing results and fracture morphology

Fig. 13 shows the maximum tensile shear force of lapped Al/CFRTP joints for different joining conditions. The maximum tensile shear force increased as the joining temperature or residence time increased. Once the temperature rose to 300 °C and the joining time reached nearly 3s, the maximum tensile shear force reached a steady plateau stage. This was because increasing the temperature and extending the reaction time promoted the chemical reaction between the silanized Al surface and molten resin of CFRTP, providing a higher chemical bonding strength.

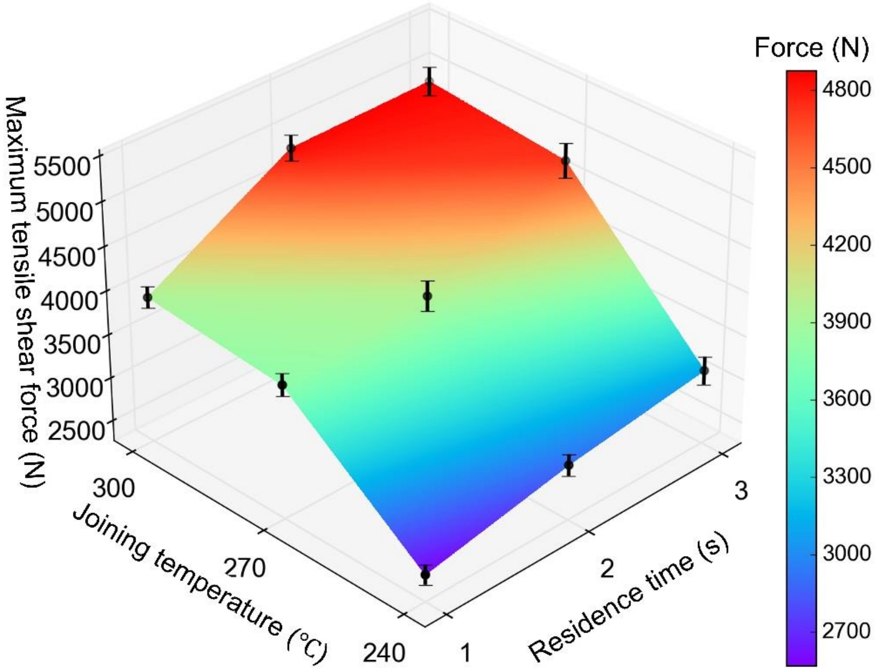

Fig. 13 The maximum lap tensile shear load at different joining temperatures and joining times.

Fig. 14(a) shows the macro-fracture morphology for each joining condition, where the fracture occurred at the interfacial zone between the silanized Al and CFRTP at low temperatures or short residence times. The distribution area of residual CF/PA6 attached on the Al surface surrounded by the red dashed line in Fig. 14(a) gradually increased as the joining temperature or time increased. In these areas, the chemically bonded strength of SCL and resin on the CFRTP side exceeded that of the CFRTP itself, leading to the shifting of crack propagation. Table 5 and Fig. 14(b) quantitatively describe this process in terms of the ratio of the area of the residual CFRTP to the total overlapping area, where the value of 1.0 indicates the case of fracture passing through CFRTP base material. The results were consistent with the chemical reaction state in Fig. 12 and interfacial strength in Fig. 13.

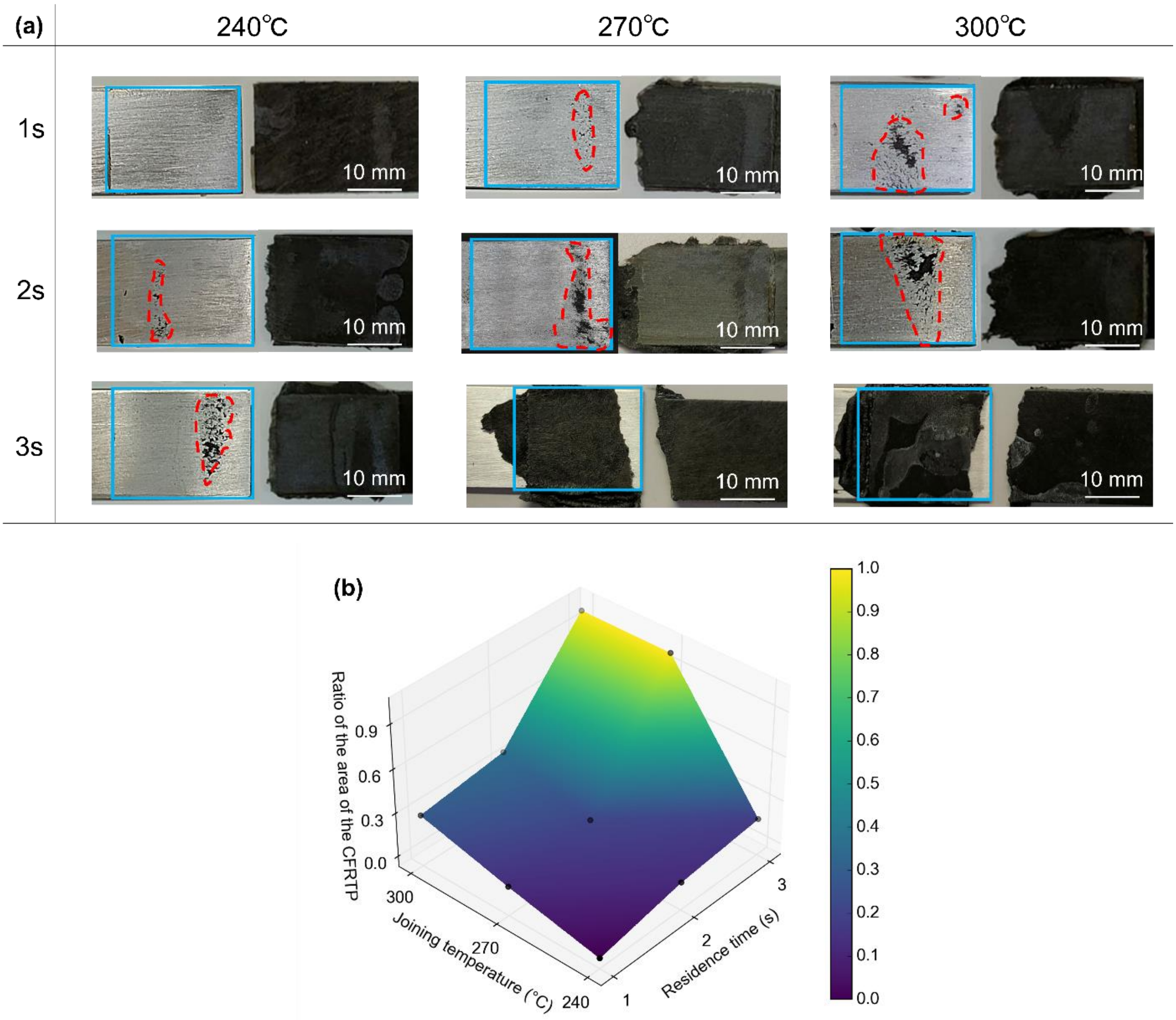

Fig. 14 (a) The macro fracture morphology at different joining temperatures and times and (b) the ratio of the area of the CFRP attached to the Al side to the total overlapping area.

Table 5 The area ratio for the residual CFRTP attached to the silanized Al surface

Joining temperatures and residence time	240 ℃	270 ℃	300 ℃
1s	0%	13%	28%
2s	12%	21%	36%
3s	18%	/	/

SEM and EDS analysis were further used to investigate the fracture characteristics of lapped Al/CFRTP joints under the joining conditions in correspondence with that in Fig. 10(a), where two positions in Fig. 15, A and B, were located near residual CFRTP on silanized Al surface in macroscopic view. Notedly, for the case of 240 °C and 1 s in Fig. 15(a), no CFRTP residue existed on the overall fracture surface of the silanized Al side at the macroscopic scale. The original micro-grooves after wet-water grinding could be easily captured on the fracture surface of the silanized Al side. Even though these grooves would provide micro-mechanical interlocking, the incomplete wetting of molten resin on the Al surface in low temperatures and the short chemical reaction time significantly reduced the interfacial strength, resulting in the fracture passing through the interface of SCL and CFRTP. Notably, the two positions had different distribution amounts of detected elements. This phenomenon might be because the thickness of the pretreatment silanized film on the Al surface was non-uniform.

In the cases of 270 °C and 300 °C at 1 s shown in Fig. 15(b) and (c), micro-morphologies of residual CFRTP appearing on the fracture surface at the macroscopic scale were exhibited clearly in the two positions, where the transition between the SCL/resin interface and the re-solidified resin could also be determined from the distribution of Al, C, and Si elements detected by EDS analysis. In the case of 300 °C, position A showed a relatively low distribution of Si and a high content of C, indicating that the re-solidified resin covered this area. Some short rod-like carbon fibers could be observed in the resin file attached to the Al fracture surface. In addition, the strip marks remaining from fractures between short carbon fibers and re-solidified resin matrix were observed in these two cases, and their amounts seemed to be more significant in the case of 300 °C. In the case of 240 °C and 3 s shown in Fig. 15(d), the element distribution at position A was similar to that in the case of 300 °C and 1 s, where the re-solidified resin matrix completely covered the fracture surface. The continuous re-solidified resin film adhered to the SCL indicated higher residence time promoted the chemical reaction of SCL and resin matrix.

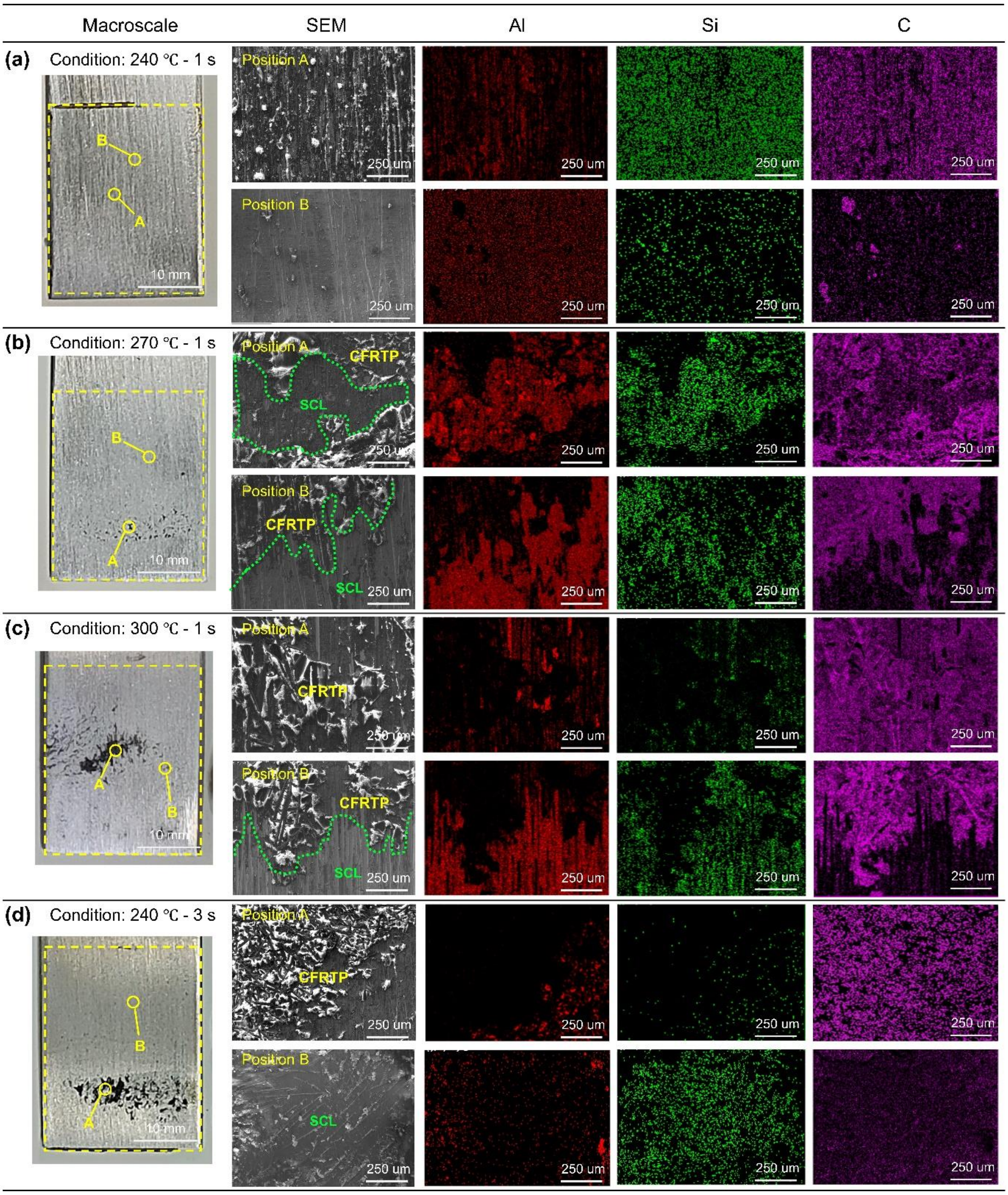

Fig. 15 SEM images and EDS results at two different positions of the fracture surfaces on the salinized Al surface in the case of (a) 240 °C-1 s, (b) 270 °C-1 s, (c) 300 °C-1 s, and (d) 240 °C-3 s.

Fig. 16 shows the XPS analysis results of the original and fracture surface of 5052 Al alloy. Fig. 16(a) schematically shows the inspection location on the Al fracture surface. As shown in Fig. 16(b), alloying elements such as Al and Mg, and elements such as C, O, and N that form oxide layers with Al were detected on the surface of the Al alloy base material. After pretreatment with the SCL, the main components, such as Si, O, and C, were detected on the surface, as shown in Fig. 16(c), with the disappearance of the peaks of the alloying elements. This suggested a dense silane coupling film on the Al surface. As shown in Fig. 16(d), the SCL composition, such as Si and O, and the Al alloy matrix composition, such as Al and Mg, were detected on the fracture surface at the joining condition 240 °C-1 s, implying that fracture was located on the SLA side of the SCL/PA6 reacted interface. In contrast, in the results shown in Fig. 16(e) and (f) for the joining conditions of 240 °C-3 s and 300 °C-1 s, the chemical reaction proceeded more sufficiently due to longer bonding time or higher temperature. As the chemical reaction proceeded, the SCL/CFRTP bonding gradually became reinforced, and more CFRTP adhered to the fracture surface. This phenomenon caused the Si intensity of the fracture surface to decrease compared to that of the freshly pretreated surface.

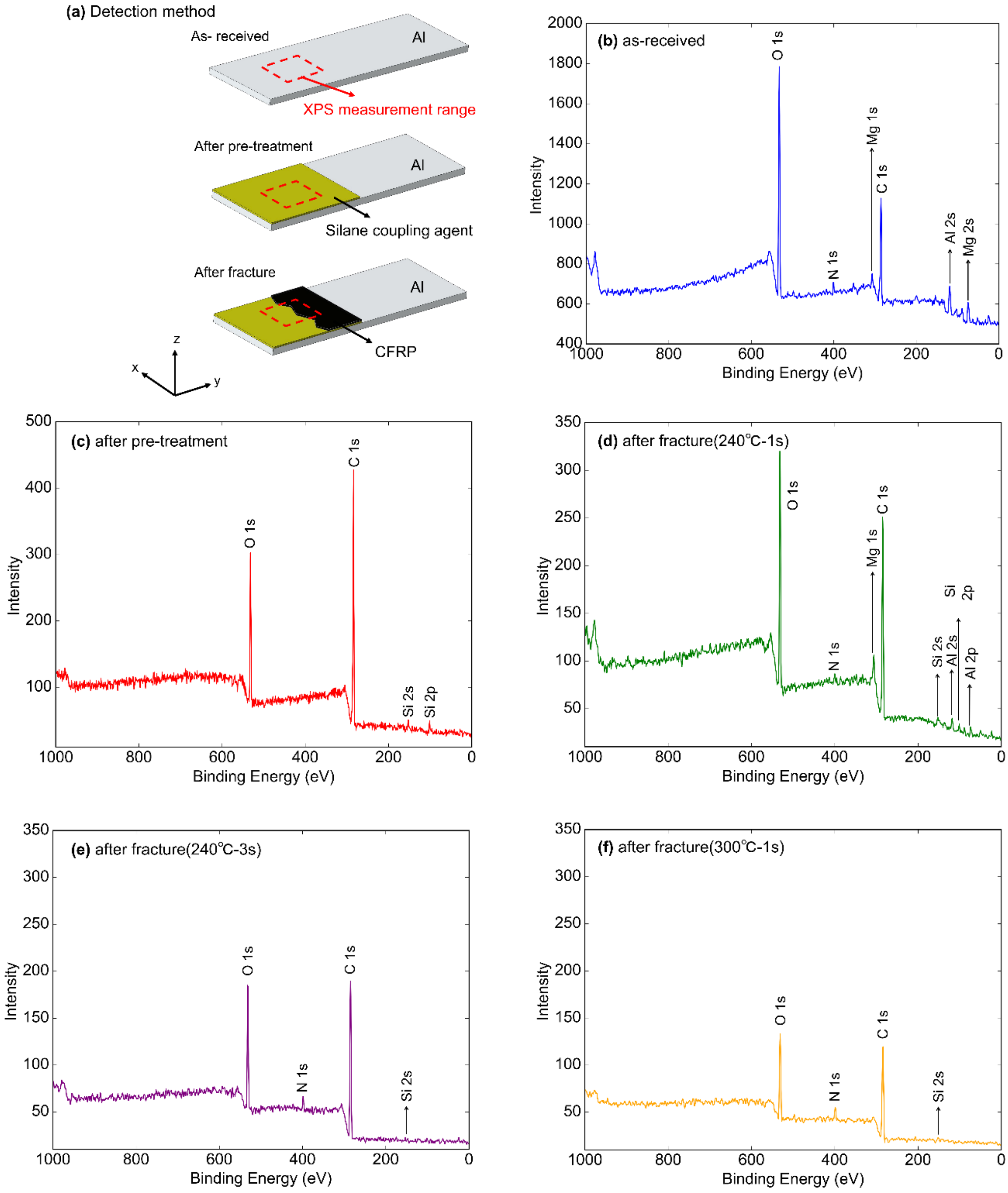

Fig. 16 X-ray photoelectron spectroscopy (XPS) analysis of original and fracture surfaces on silanized Al alloy side: (a) The sampling position for detection specimen of XPS, and the XPS results of (b) as-received Al surface, (c) pretreatment Al surface, (d) fracture surface at 240 °C-1 s, (e) fracture surface at 240 °C-3 s, and (f) fracture surface at 300 °C-1 s.

3.5 Key findings and highlights

3.5.1 Failure mode of silanized Al/CFRTP interface

Based on the experimental observations, when silane coupling treatment was performed on the as-received Al alloy, a thin SCL within the thickness scale from several nanometers to hundreds of nanometers was formed on the surface of the 5052 Al alloy by the reactions described in Fig. 2. In the isothermal-pressing joining process, the chemical bonding force of covalent bonds creating at both the interface between the SCL and CFRTP matrix PA6, and the interface between the SCL and 5052 Al alloy, resulted in the firmly joining between 5052 Al and CF/PA6. From the fracture morphologies in Figs. 14 and 15, the fracture mechanism of the lapped Al/CFRTP interface was mainly characterized by three types: pure adhesive fracture, hybrid adhesive and cohesive fracture, and pure cohesive fracture, which was related to the chemical reaction state between the SCL and the PA6 matrix at different joining condition.

Fig. 17 schematically shows the different fracture crack propagations with the increase in joining temperatures and residence times, exhibiting the correlation of the joint failure mode with the thermal condition. At a low temperature slightly higher than the melting point of CF/PA6, the fracture crack mainly propagated along the interface of the SCL and re-solidified PA6, where an incomplete chemical reaction state offered weak chemical bonding forces and less molten-state resin led to poor wetting on the silanized Al surface. As shown in Fig. 17, increasing residence time could limitedly improve the chemical reaction state and physical wetting. The crack would transfer into the re-solidified resin in some local regions. Increasing the joining temperatures would enhance the interfacial strength between the SCL and CFRTP matrix PA6, resulting in the crack propagation mainly occurring inside the PA6 matrix adjacent to the overlapped interface. This phenomenon was more significant when the joining temperatures increased. Except for the improved chemical reaction state, more resin matrix was melted at higher joining temperatures, enhancing the physical and mechanical bonds to a certain extent. However, the chemical bonds predominated the interfacial strength among them. In particular, when the joining temperatures reached a value close to the thermal decomposition point of the CF/PA6, the promotion effect of increasing temperature on chemical reaction completeness was more significant, resulting in the fracture crack propagating throughout the inner re-solidified PA6 matrix in lager overlappiong areas. Notably, because of the negative effect of the CFRTP thickness reduction in the overlapping area, the fracture initiated from the re-solidified resin close to the SCL/CFRTP interface and passed through the CFRTP matrix along the thinning thickness direction.

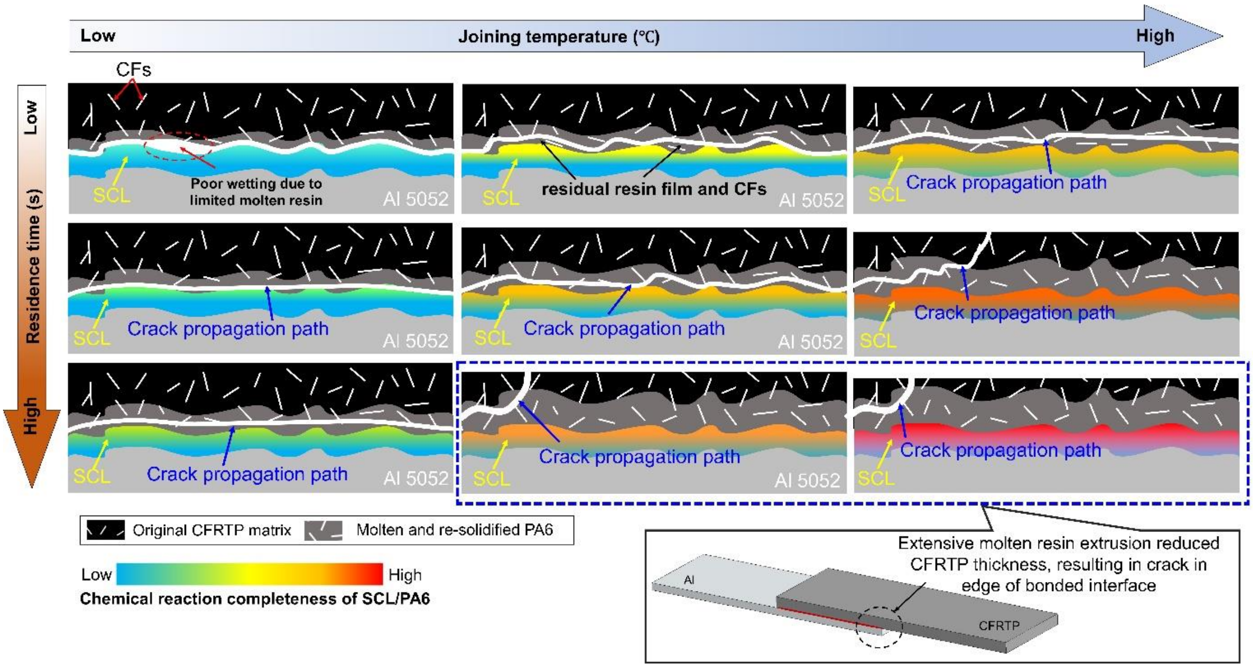

Fig. 17 Schematical diagram showing failure mode of isothermal-pressing joined Al/CFRTP different joining conditions.

3.5.2 Adequacy of chemical reaction state related to thermal condition

The current investigation demonstrated that increasing joining temperatures could stimulate the activity of elements or polar functional groups and accelerate the covalent bonds through a chemical reaction. At a given joining temperature higher than the melting point of the CF/PA6, determining the critical joining time to achieve the complete chemical reaction will help optimize the residence time in the isothermal-pressing joining process or even other heat-assisted joining processes between silanized Al alloy and CF/PA6.

Fig. 18 presents the average duration time of interfacial high-temperature above 220 °C for different joining conditions and the tested maximum tensile shear forces of joints. The results indicated that increasing the joining temperature or prolonging residence time produced a longer high-temperature duration time, exhibiting a positive linear correlation with the maximum tensile shear force in a certain range. In this study, an average critical joining time of approximately 6.0 s to achieve the complete chemical reaction state could be determined from the relationship between high-temperature duration time and the maximum tensile shear force. The determined time was relatively shorter in comparison to previous studies conducted by Choi et al. [13], Xia et al. [8], and Tao et al. [7], where the critical duration times were ~8.8 s, ~8.0 s, and ~7.1 s, respectively. This difference could be attributed to the applied pressure in the different experiments, which also played a vital role in the hot-pressing experiment by affecting the wettability and flow of the molten resin on the Al surface, stimulating the contact thermal conduction and enhancing the physical bonding. This is not the scope of the current study, and it will be investigated in future studies.

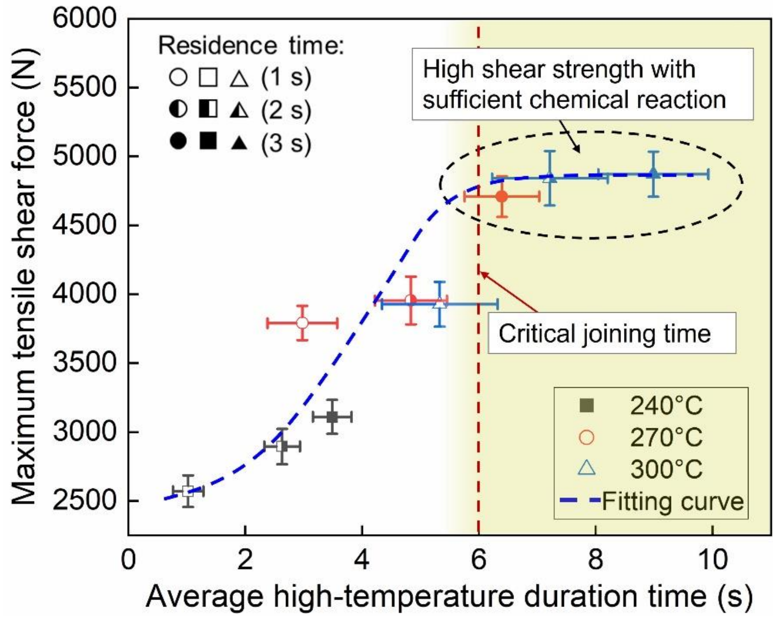

Fig. 18 Correlation between maximum tensile shear force and average high-temperature duration time in different joining conditions.

Additionally, as shown in Fig. 18, with the high-temperature duration time increasing above 6.0 s, the maximum tensile shear forces were close for the cases of 270 °C-3 s, 300 °C-2 s, and 300 °C-3 s. Moreover, the joints in the cases of 270 °C-3 s and 300 °C-3 s were fractured on the matrix of CFRTP, and the maximum tensile shear forces could not reflect their interfacial strength. Therefore, miniature shear testing was further performed in the current study to evaluate their interfacial strength. Fig. 19(a) schematically exhibited the sampling position of miniature shear testing. The shear test results are shown in Fig. 19(b), where each experimental condition was tested three times and averaged to obtain the standard deviations. For the case of 300 °C-3 s, the maximum strength could reach ~31 MPa. However, the average shear strengths for the three experimental conditions were mainly concentrated in the range of 22–25 MPa, without significant strength differences. This demonstrated that the bonding strength of lapped Al/CFRTP reached its peak and did not continue to increase with a higher joining temperature or longer joining time. In other words, this also revealed that the complete chemical reaction state occurred in these three cases. Fig. 20 details the strength comparisons of Al alloy/CFRTP joints made by different heat-assisted joining processes. From the cited literature shown in Fig. 20, the maximum joint strength between Al alloy and PA-based CFRTP was approximately ~33 MPa, due to the predominated mechanical interlocking [30,31]. The current findings proved that chemical bonding could provide comparable interfacial strength, and even a higher interfacial strength could be realized by further enhancing the chemical reaction state.

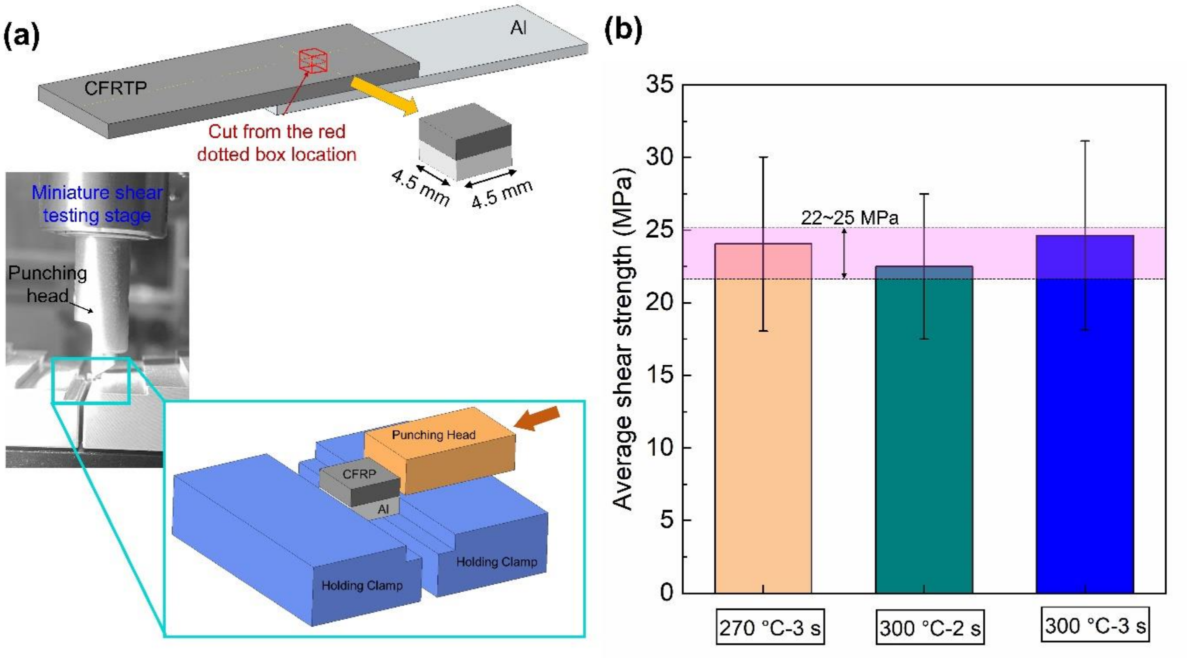

Fig. 19 Additional miniature shear testing and results for the Al/CFRP joint fractured in CFRP matrix: (a) the preparation of tested specimen (b) test results of different joining conditions.

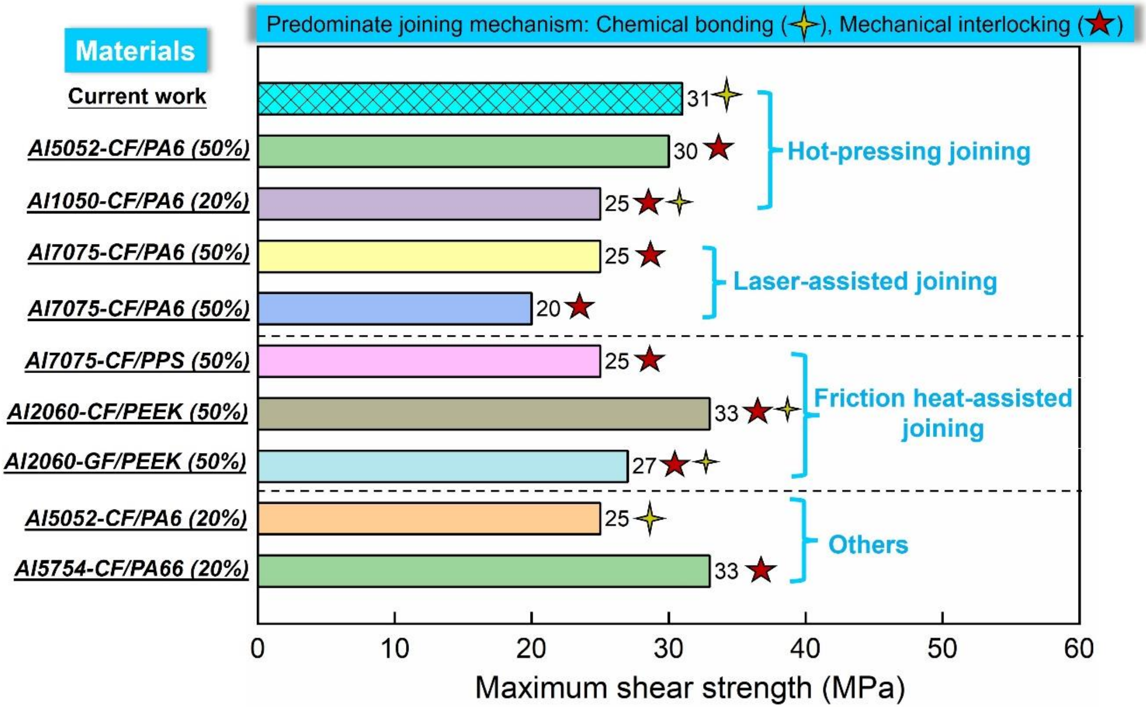

Fig. 20 Comparison of the maximum shear strength of different heat-assisted joining processes for Al/CFRTP joint. Hot-pressing joining of Al5052-CF/PA6 [32] and Al1050-CF/PA6 [33]; Laser-assisted joining of Al7075-CF/PA6 [34,35]; Friction heat-assisted joining of Al7075-CF/PPS [36], Al2060-CF/PEEK [31] and Al2060-GF/PEEK [37]; Others are ultrasonically welding of Al5754-CF/PA66) [30] and resistance spot welding of Al5052-CF/PA6 [11].

3.6 Summary

The summary and conclusions from the current study are as follows:

(1) The high-strength joints of CF/PA6 and 5052 Al sheets were achieved using an isothermal-pressing joining process. A homogeneous SCL between CFRTP and Al was formed at a microscopic scale for different studied conditions. No significant interfacial defects existed at the joined interface, while limited micro-porosities caused by cooling shrinkage existed in the re-solidified resin close to the interface. Lowering the interface temperature and reducing the outflow of molten resin would alleviate this issue.

(2) The CF/PA6-5052 Al alloy joining was achieved through a chemical reaction between the amide group on the CFRTP and the epoxy group of the silanized Al surface. Raman spectroscopy detected the residual epoxy groups in the bonded interface, showing that the chemical reaction was more pronounced with increasing joining temperature.

(3) The single lap shear test of the joint obtained at a joining temperature of 300 °C and a joining time of 3 s achieved the maximum tensile-shear force of 4.8 kN. Increasing joining temperature and time would increase joint strength. The overall fracture zone was mainly located at the SCL/Al and SCL/CFRTP interfaces for joints obtained at low joining temperatures and short joining times. However, higher temperatures and times resulted in fracture at the SCL/CFRTP interface of the joint, or the crack initiated at the re-solidified resin and subsequently through the thickness of CF/PA6.

(4) Further shear strength testing for the joints fractured at the CF/PA6 side showed that average interfacial shear strength achieved a high value above ~22 MPa, which was comparable to the optimized strength of other heat-assisted joining technologies of Al and CFRTP. At a constant pressure of 0.2 MPa, a critical high-temperature duration time of ~6.0 s at least was recommended to achieve high-strength joining between 5052 Al alloy and CF/PA6.

4. Strength and Fracture Behavior of Pressure-Controlled Hot-Pressed Joints

While previous investigations in Chapter 3 revealed how joining temperature and duration time influence the interfacial evolution and mechanical performance of Al/CF–PA6 joints, the role of pressure—an equally critical process parameter—remains less thoroughly explored. In conventional hot-pressing processes, pressure is often treated as a fixed input. However, variations in pressure, particularly under elevated temperatures, can significantly influence resin flow, fiber distribution, defect formation, and ultimately, joint strength. To address this gap, this chapter introduces a thinning-controlled hot-pressing strategy, wherein a constant vertical displacement of the pressure plate (i.e., a fixed thinning distance) is maintained throughout the joining process. Under this constraint, all specimens experience the same geometric boundary conditions. As the joining temperature increases, the softened polymer becomes more deformable, resulting in different levels of effective pressure at the Al/CFRTP interface—even though the machine-controlled displacement remains unchanged. This experimental strategy enables a physically grounded modulation of effective pressure, intrinsically coupled with the thermal response of the material system, without requiring additional process complexity. This chapter investigates how these variations in effective pressure, induced by the thinning-controlled setup, affect joint strength, interfacial microstructure, chemical bonding, and failure modes. Special attention is given to the dual effects of pressure—facilitating resin infiltration and intimate interfacial contact at moderate levels, but also potentially causing resin depletion or void formation under high thermal input. By systematically analyzing the coupling between temperature, pressure, and holding time, this chapter provides new insights into the underlying mechanisms of interface development and performance degradation in thermally assisted joining of dissimilar materials. The findings presented here complement those of Chapter 3 and collectively support the development of predictive process–structure–property models in Chapter 5. This chapter is organized as follows:

Section 4.1 introduces the results of the thinning-controlled hot-pressing method.

Section 4.2 presents experimental results on joint strength and fracture behavior under different thermal–mechanical conditions.

Section 4.3 analyzes interfacial chemical bonding evolution via Raman spectroscopy and resin flow behavior, fiber distribution, and void formation using SEM imaging.

Section 4.4 discusses fracture behavior of the thinning-controlled hot-pressing.

4.1 Effectiveness of the improved hot pressing

To investigate how thermally induced variations in effective pressure affect the joint formation process, a thickness-controlled hot-pressing strategy was employed in this chapter. In this configuration, the vertical displacement of the upper pressure plate was fixed during joining, thereby constraining the final joint thickness and allowing the effective pressure to vary in response to polymer softening. This method enables pressure modulation through material flow behavior itself, without altering external load inputs, and serves as a practical way to study the pressure–temperature coupling effect in hot-press joining. Fig. 21(a) and Fig. 21(b) show the morphological appearance and cross-section of the Al-to-20% short CF/PA6 lap joints fabricated by conventional and thinning-controlled hot-pressing joining processes under different experimental conditions. For Al-to-20% short CF/PA6 lap joints fabricated using conventional hot-pressing joining in a previous study[38], the absence of thinning control resulted in unconstrained extrusion of the molten resin from the CF/PA6 near the interface between the two sheets, as shown in Fig. 21(a). By contrast, the thinning displacement control mode produced an Al-to-CF/PA6 lap joint with a significant reduction in the amount of molten resin extruded, as shown in Fig. 21(b). Comparisons of the average joint strength characterized by the maximum tensile-shear force of the lap joints shown in Fig. 21(c) indicated that the improved hot-pressing joining process with thinning displacement control achieved comparable joint interface strength but better joint formation quality without excessive resin extrusion. Based on the preliminary experiment, by applying a higher joining pressure with a 0.2-mm thinning displacement, a sufficiently high lap tensile-shear force was achieved in a shorter heating time with a lower joining temperature.

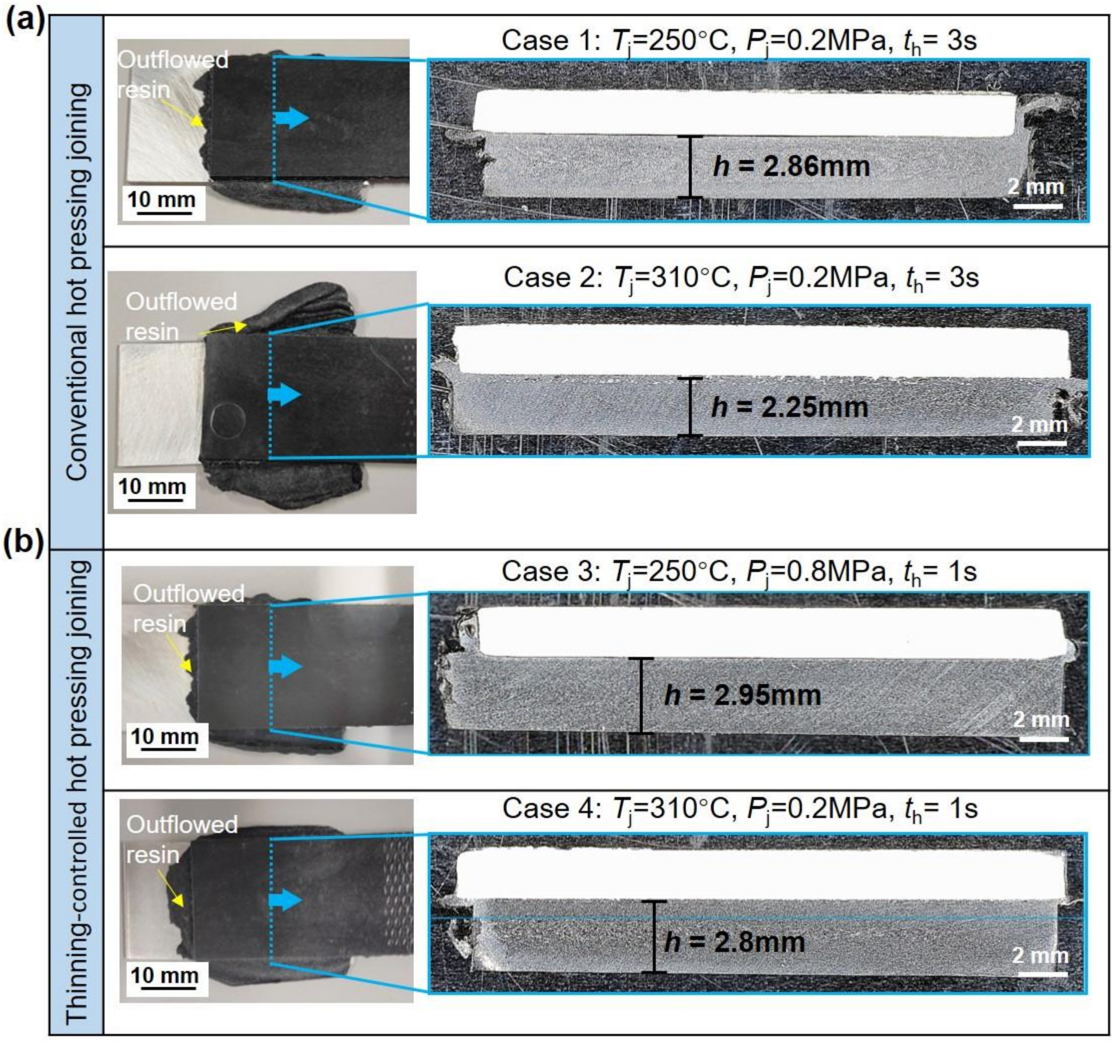
(a)
Conventional hot pressing joining
Case 1: T_j=250°C, P_j=0.2MPa, t_h= 3s
Outflowed resin
10 mm
h = 2.86mm
2 mm
Case 2: T_j=310°C, P_j=0.2MPa, t_h= 3s
Outflowed resin
10 mm
h = 2.25mm
2 mm
(b)
Thinning-controlled hot pressing joining
Case 3: T_j=250°C, P_j=0.8MPa, t_h= 1s
Outflowed resin
10 mm
h = 2.95mm
2 mm
Case 4: T_j=310°C, P_j=0.2MPa, t_h= 1s
Outflowed resin
10 mm
h = 2.8mm
2 mm

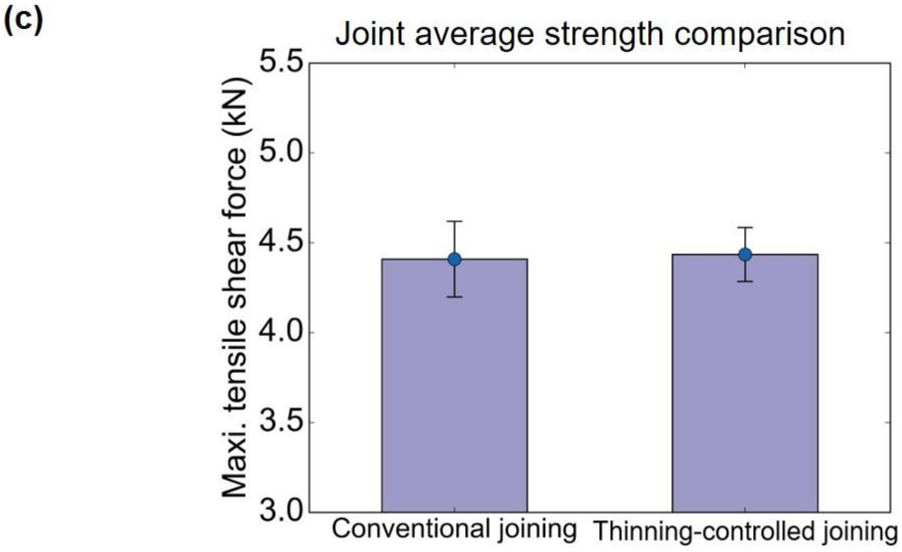
(c)
Joint average strength comparison
Maxi. tensile shear force (kN)
5.5
5.0
4.5
4.0
3.5
3.0
Conventional joining
Thinning-controlled joining

Fig. 21 The morphology of (a) conventional hot pressing joining and (b) Thinning-controlled hot pressing joining and (c) compared maximum tensile-shear strengths of the original and improved process.

4.2 Experimental results on joint strength and fracture behavior

Fig. 22 shows the maximum tensile-shear forces of the lap joints between the 5052 Al alloy and CF/PA6 with three different fractions of short and long fibers obtained by thinning-controlled hot-press joining under different joining conditions (the raw curve data is shown in Appendix A). The shaded areas in yellow and blue indicate the trend range of the tensile-shear forces. The three types of Al-to-CF/PA6 lap joints showed similar strengths and trend changes under each constant joining pressure. This indicates that the difference in the volume fractions and morphologies of carbon fibers in CF/PA6 did not significantly impact the bond formation between the molten resin and silane-treated Al alloy surface under the same joining conditions, even though the presence of carbon fibers did have some influence on the flowability of the molten resin. Therefore, in the subsequent analysis and discussion of the interface structure and fracture behavior, only the 20% short CF/PA6 joints were selected as representatives for a detailed examination in this study. As shown in Fig. 22, over a fairly wide temperature range, the joint strength gradually increases as the joining temperature or the heating time increases for joining pressures of 0.2 MPa and 0.8 MPa; meanwhile, it exhibits a decreasing tendency with a higher heating time or joining temperature as it approaches the decomposition temperature of the CF/PA6. Compared to a low joining pressure, the critical joining temperature at which a decrease in strength occurs is relatively lower under a higher joining pressure. This indicates that, for the thinning-controlled hot-press joining process, increasing the pressure enhances the interface bond strength to a greater extent at lower temperatures. However, at higher temperatures, the strength improvement resulting from the increased pressure gradually diminishes, even falling below the interfacial strength achieved under low pressure conditions.

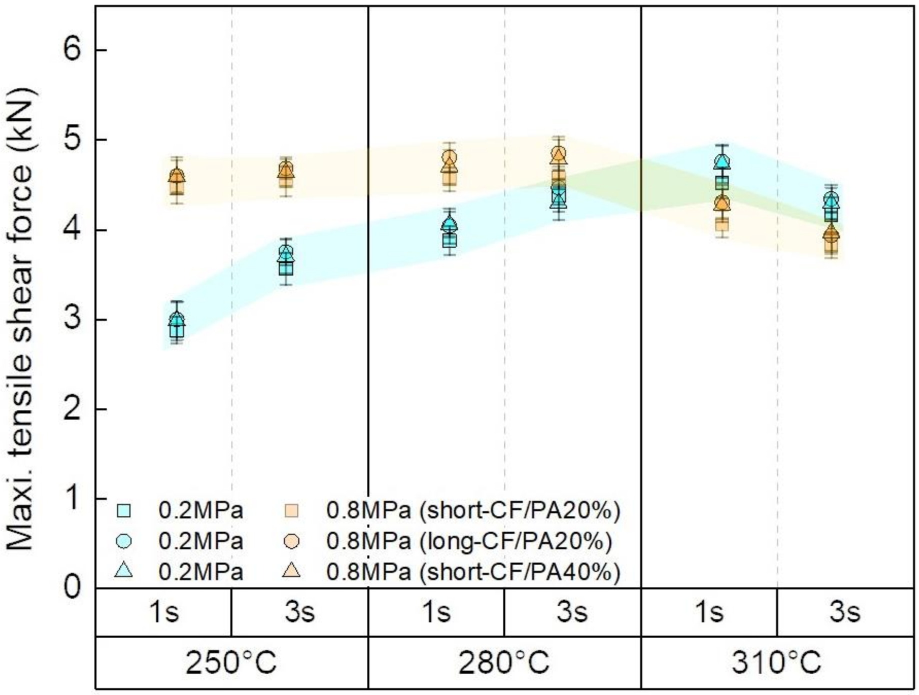

Fig. 22 The maximum tensile-shear forces of lap joints between 5052 Al alloy and three different CF/PA6.

Fig. 23 shows three typical fracture characteristics of the studied lap joints between the Al alloy and the 20% short CF/PA6. For a fractured lap joint with a low tensile-shear force, the fractured Al surface exhibited a metallic luster with no macroscopically visible black CFRP residual components. Further microscopic results obtained by EDS analysis revealed the homogenous dispersion of Si across the Al surface. Meanwhile, the absence of Al and Si and the aggregation of C appeared in localized regions, as indicated by the arrows in Fig. 23(a), indicating the presence of resin that covered this area. The present fracture characteristics indicate that in some localized regions of the CFRTP, fracture may occur mainly between the resin matrix and the SCA, accompanied by tearing inside the reconsolidated resin near the SCA.

Fig. 23(b) shows a more complex mixed fracture pattern in which bright metallic lusters and some resin and black carbon fiber residues can be observed on the surface of the fractured Al. Furthermore, the EDS results show a larger area of Al and Si elemental deficiencies and C element aggregates compared to Fig. 23(a), accompanied by the appearance of carbon fibers represented by short rod-like C aggregates. This indicates that the fracture passed through the CFRTP and SCA from the starting position and partially extended inside the CFRTP matrix, with a greater amount of resin and a certain amount of carbon fiber rods remaining on the Al surface. Fig. 23(c) shows a joint with a high tensile-shear load, where the fracture passes through the CFRTP itself instead of advancing along the CFRTP/Al interface, resulting in the fracture of the CFRTP base material.

(a) T_j= 250°C, P_j= 0.2MPa, t_h= 1s

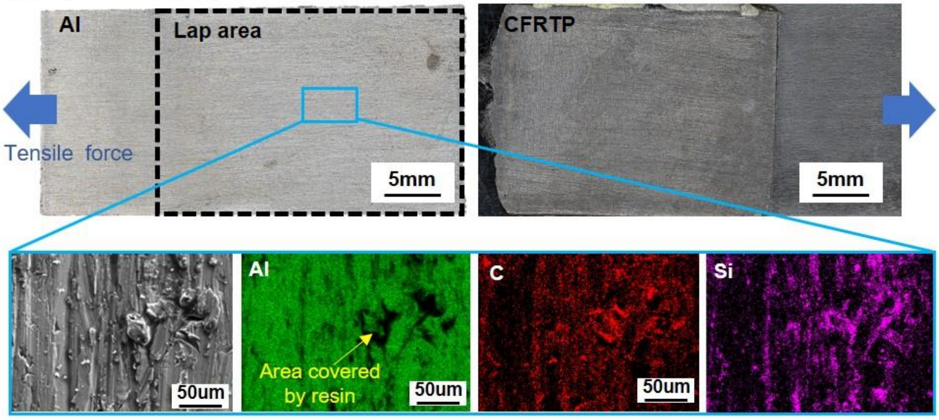

(b) T_j= 250°C, P_j= 0.8MPa, t_h= 3s

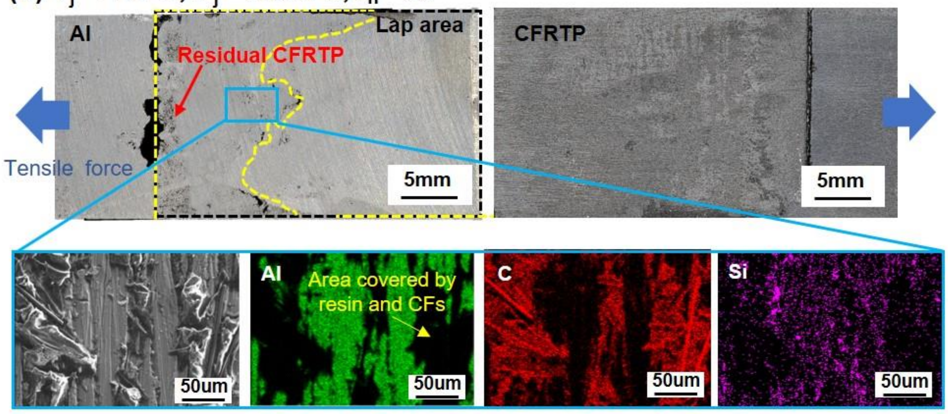

(c) T_j= 280°C, P_j= 0.8MPa, t_h= 1s

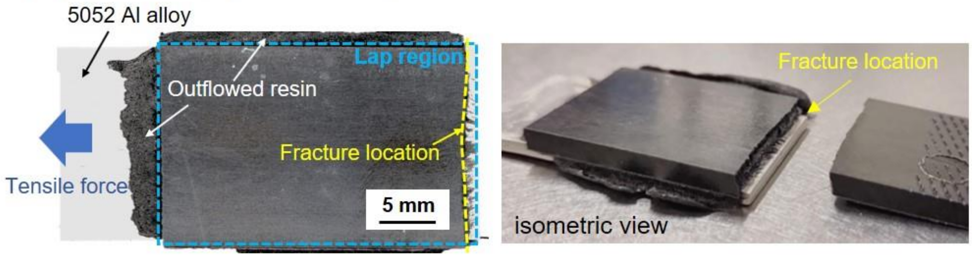

(d) T_j= 310°C, P_j= 0.8MPa, t_h= 3s

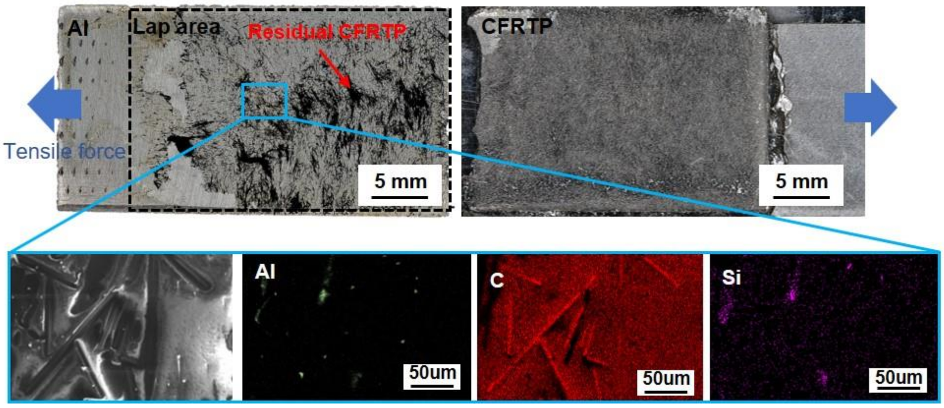

Fig. 23 Typical post-fracture Al surface morphologies and EDS results.

Fig. 24 illustrates the proportion of the area of CFs remaining on the Al surface to the area of the overlapping region of the joint between the CFRTP material and Al under different welding conditions, with the case of Fig. 23(a) as zero and the case of Fig. 23(c) as one. In Fig. 24, colors of lines are used to distinguish the joining times, while line forms are used to distinguish different joining pressures. Before 310°C, the percentage of CFRTP residual area on the Al surface is positively correlated with the joining temperature. Under the same temperature, the percentage of CFRTP residual area is also shown to be positively correlated with the joining time and pressure. Both fracture patterns shown in Figs. 23(b) and (c) occur under the joining conditions of T_j= 280 ℃, P_j = 0.8 MPa, t_n = 3 s and T_j= 310 ℃, P_j = 0.2 MPa, t_n = 1 s , resulting in an error range of 0.8 to 1 for the area ratio of residual CFRTP. The highest joint tensile forces are observed at this point. In contrast, when the residence time or pressure continues to increase at a temperature of 310 °C, as shown in Fig. 23(d), the increase of internal defects leads to a decrease in strength, with a significant amount of CFRTP remaining on the Al surface. EDS showed that the Al surface was covered by carbon, indicating that the fracture occurred almost exclusively inside the CFRTP.

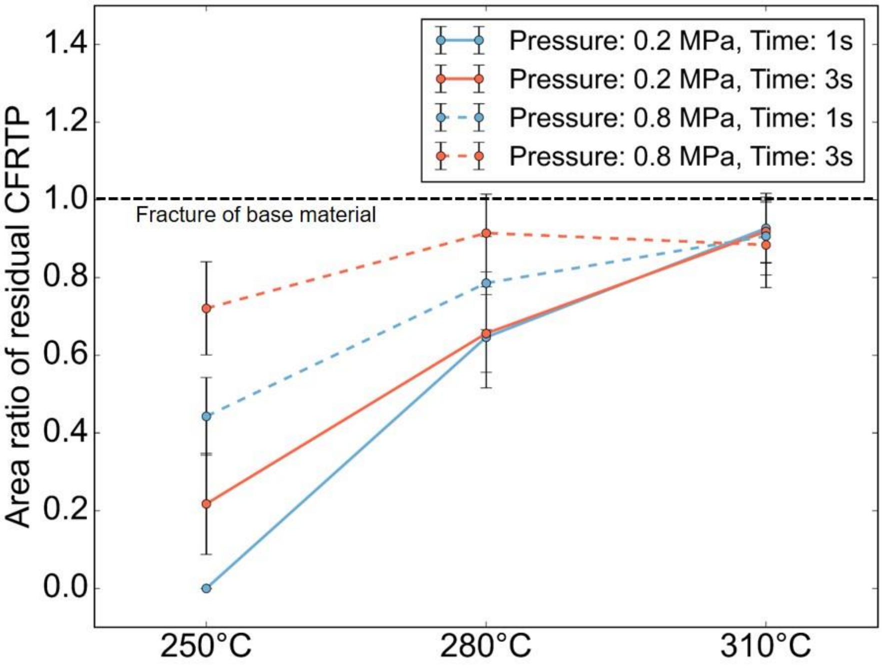

Fig. 24 The area ratio of residual CFRTP on the Al surface after fracture.

4.3 Chemical bonding and near-interface structure

The strength of the interface between the silane-treated Al alloy surface and CF/PA6 in thermal-assisted joining is governed predominantly by the state of the interfacial chemical bonding. This involves a complex interplay between various factors, including the extent of the chemical reaction completion, bond strength, bond density, molten state of the resin in contact with the silane film, thermal conditions, and reactivity of the functional groups participating in the bonding process. To understand the effects of various joining conditions in thinning-controlled hot-pressing joining between the 5052 Al alloy and CF/PA6, the chemical bonding state and near-interface structures, including the mixing state of the resolidified resin and CFs and the existence of decomposition defects, were investigated in this study.

Fig. 25(a) shows the variation in the relative content of epoxy groups in the SCA lapped with resin or carbon fibers under the different welding conditions. The relative content of the epoxy groups in contact with the resin was lower than that with the carbon fiber, indicating that the SCA layer on the Al surface reacted chemically with the PA6 resin. Carbon fibers in contact with the Al surface were embedded in the SCA layer, resulting in an insufficient chemical reaction. However, the relative content of the epoxy groups in the SCA in contact with the resin decreased slightly with increasing temperature or pressure but remained almost constant. The temperature histories of the Al interface during the cooling stage at different temperatures and pressures are shown in Fig. 25(b). Air-cooled joints experienced melting residence times ranging from 60 to 120 s under the studied joining conditions. Epoxy and amide groups fully react with each other during a sufficiently high-temperature residence time. Consequently, the epoxy groups were fully consumed and remained at the same level, even under different joining conditions.

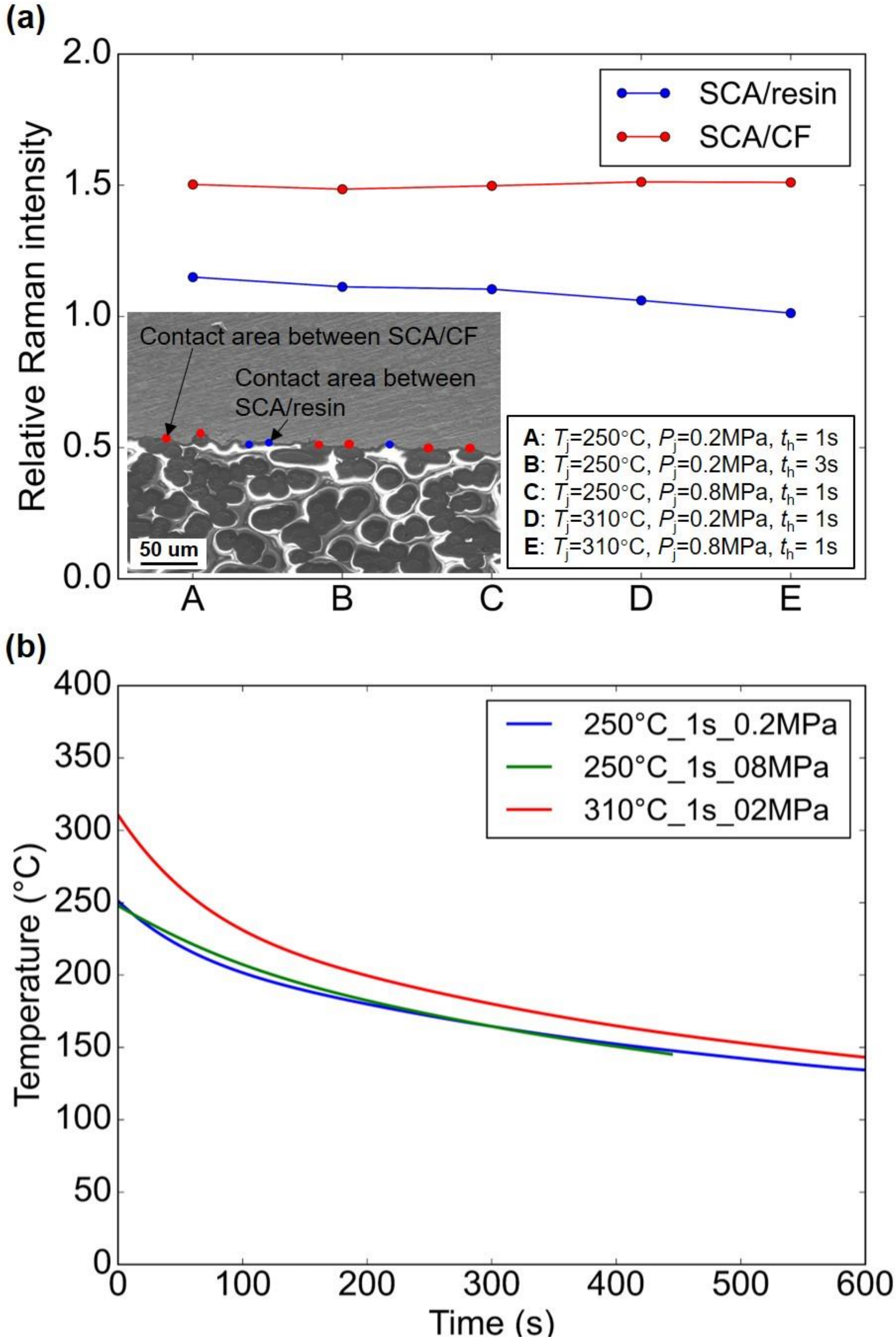

Fig. 25 (a) The variation of the relative content of epoxy groups measured by Raman spectroscopy and (b) temperature history of joints at different temperatures and pressures during the cooling stages.

Fig. 26 shows the near-interface microstructure analyzed using SEM. The location of the Al-to-CF/PA6 interface was obtained from a cross-sectional section located at the midpoint of the overlapping surface. The CFRTP near the interface after hot pressing results from the mixing of molten resin and CFs during heating and subsequent re-solidification during cooling. For different joining conditions, the center and edge positions of the lap joints had similar structural distributions, indicating that uniform Al/CFRTP joints were obtained. The gray area on the upper side of each image is Al. The bright white area on the lower side, due to the charging effect, is the PA6 resin matrix. The cylindrical black part wrapped in the resin is the carbon fiber.

According to the analysis corresponding to the phenomenon shown in Fig. 25, it is reasonable to assume that only the contact between the PA6 resin and SCA layer is effective in interfacial bonding, while the contact between the carbon fiber and SCA does not contribute significantly to the strength of the Al/CFRTP joints. As shown in Fig. 26(b), the carbon fibers and PA6 resin matrix near the Al/CFRTP interface showed a relatively homogeneous distribution at 250 °C. A limited SCA layer on the Al surface contacts the PA6 resin to form chemical bonds. A significant amount of bright white PA6 resin aggregates near the Al/CFRTP interface when the temperature rises to 310 °C, as shown in Fig. 26(c), and the black carbon fibers are far away from the interface. It is reasonable to assume that the molten PA6 resin at high temperatures has high flowability, whereas the carbon fibers have insufficient mobility. The PA6 resin is pushed through the carbon fibers to the Al surface under a certain pressure, forming full contact with the SCA and conducting chemical reactions, resulting in the formation of strong chemical bonds. Fig. 26(d) illustrates the time enhancement scenario from 1 to 3 s, with only a limited increase in the PA6 resin near the interface. It is believed that although the flow of PA6 is sustained for a longer period, the enhancement in the number of chemical bonds per unit area of the interface is limited because of the restricted flow at low temperature and pressure conditions.

As shown in Fig. 26(e), more bright white resin appears in the region near the Al/CFRTP interface when the pressure is increased from 0.2 MPa to 0.8 MPa. Similar phenomena were reported by Harper et al. [39] in their study on the curing of epoxy resins for pre-impregnated carbon fibers, in which they found that the resin was able to infiltrate the carbon fibers faster when the curing pressure was increased, resulting in composites with fewer defects and a higher density. In contrast, Leclerc et al. [40] found that increasing the injection pressure led to higher injection speeds, a higher resin filling rate, and a lower void defect content in the molded product. Amico et al. provided a theoretical explanation for this phenomenon in their fluid investigation of resin transfer molding [41]. They derived an equation for the penetration thickness x of the resin into the fiber preform based on Darcy's law, as shown in Eq. (4), where the applied mechanical pressure P_m is a positively correlated quantity that enhances penetration.

$$x^2 = \frac{2\kappa}{\mu\varepsilon}(P_m + P_c)t \tag{4}$$

Therefore, it is reasonable to believe that the increased pressure caused the resin to flow faster, penetrating the slow-moving carbon fibers and filling the silanized Al surface in a short period, resulting in a sufficient chemical reaction with the SCA layer and the formation of a sufficiently strong chemical bond, the impregnation mechanisms of which are shown in Fig. 26(g).

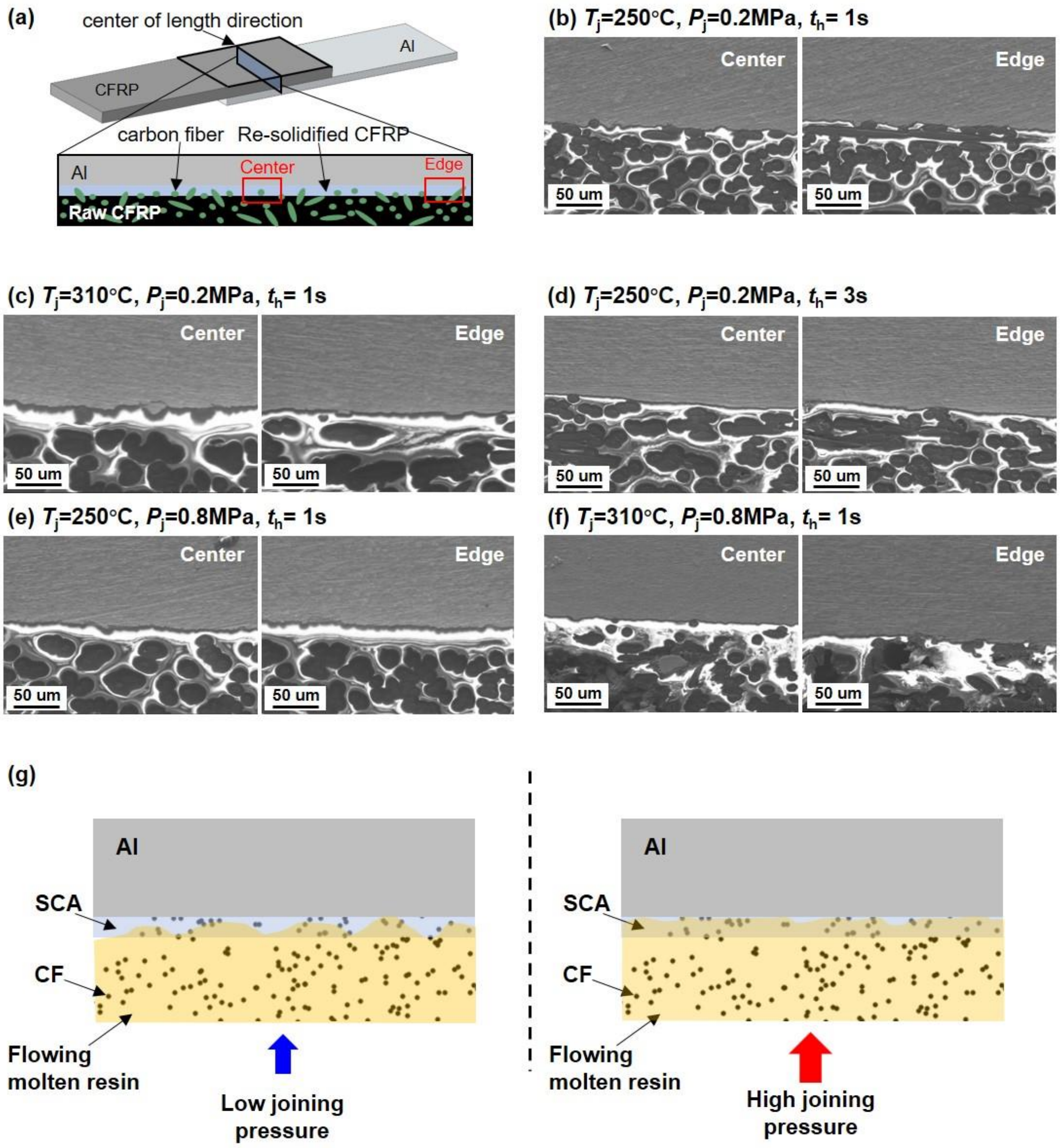

Fig. 26 (a) Observation position and (b–f) SEM images at the Al/CFRTP interface and (g) Schematic of the impregnation mechanism.

Fig. 27 shows the percentage of the silanized aluminum surface in contact with the resin over the total Al/CFRTP contact and the corresponding tensile-shear load of the joints, as statistically determined from the cross-section of the joints for each of the conditions presented in Fig. 25. The resin percentage and tensile-shear load show a very similar trend reaching 310 °C, 1 s, and 0.2 MPa, indicating that increasing the contact between resin and silanized aluminum can improve the bond strength when the resin and the silanized aluminum are sufficiently reacted. However, when the pressure reaches 0.8 MPa while other conditions remain unchanged, the defects inside the resin substrate of CFRTP lead to a decrease in bond strength, which shows an opposite trend to the percentage of resin contact. Therefore, varying the physical conditions (e.g., pressure) to improve the compositional distribution of the composite is also an effective way to achieve high-strength bonding compared to varying thermodynamic conditions such as temperature and time. Both were effective in increasing the amount of PA6 resin per unit volume involved in the chemical reaction. However, as shown in Fig. 26(f), when both the temperature and pressure were elevated, the resin within the CFRTP decomposed, leading to the creation of porous defects.

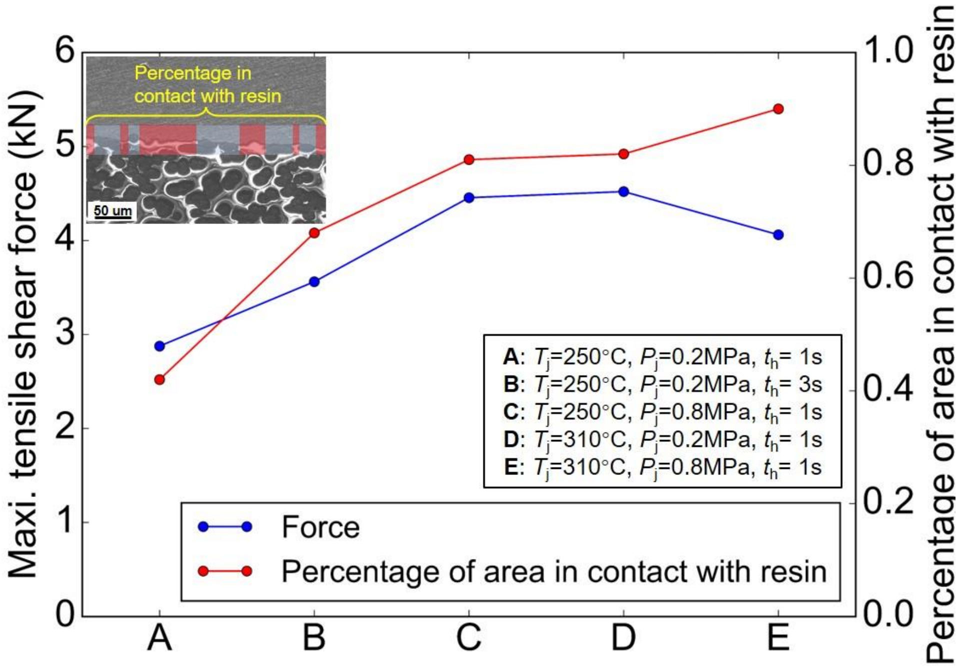

Fig. 27 Percentage trend of the silanized aluminum surface in contact with the resin.

4.4 Fracture behaviors

The results of increasing the bonding pressure are somewhat similar to those of increasing the temperature and bonding time, mainly due to their ability to enhance the strength of the aluminum/CFRTP interface. In terms of the underlying mechanism, changing the carbon fiber and resin components at the interface by increasing the joining pressure mechanically increases the number of bonds per unit area of the interface, resulting in higher-quality welded joints at lower joining temperatures and shorter heating time. Fig. 28 schematically shows the interface bonding zone of lap Al/CFRTP under different joining conditions and the corresponding crack propagation path during tensile-shear testing.

Under low temperature and low pressure conditions, the fluidity of the melted resin in the CFRTP is restricted, some CFs stay at the Al/CFRTP interface, resulting in the SCA layer being in contact with both the carbon fibers and the resin. The analysis in Fig. 25 shows that CFs are difficult to form chemical bonds with the SCA, which limits the amount of chemical bonding per unit area (chemical bonding density) between the silanized Al and the CFRP. Therefore the overall joint strength is low for this condition. During the evolution of fracture, cracks first occurred at the Al/CFRTP edges where stress concentrations existed, and subsequently extended along the CFRTP/silanized Al interface. A limited amount of resin was left on the silanized Al surface after fracture as shown in Fig. 23(a).

Upon increasing the joining pressure at the interface at low temperatures, as shown in Fig. 26(e), the molten resin near the CFRTP-silanized Al interface flowed rapidly and filled the Al surface. A greater chemical bonding density was formed between the resolidified resin and the SCA, which improved the bond strength. During the fracture process, cracks propagated from the interface between the CFRTP and the silanized Al inside the CFRTP owing to the increased strength of the CFRTP-silanized Al interface, resulting in the fracture of the resolidified resin. Compared to the low-pressure condition, a larger amount of resin, together with the encapsulated carbon fibers, remained on the Al surface after fracture.

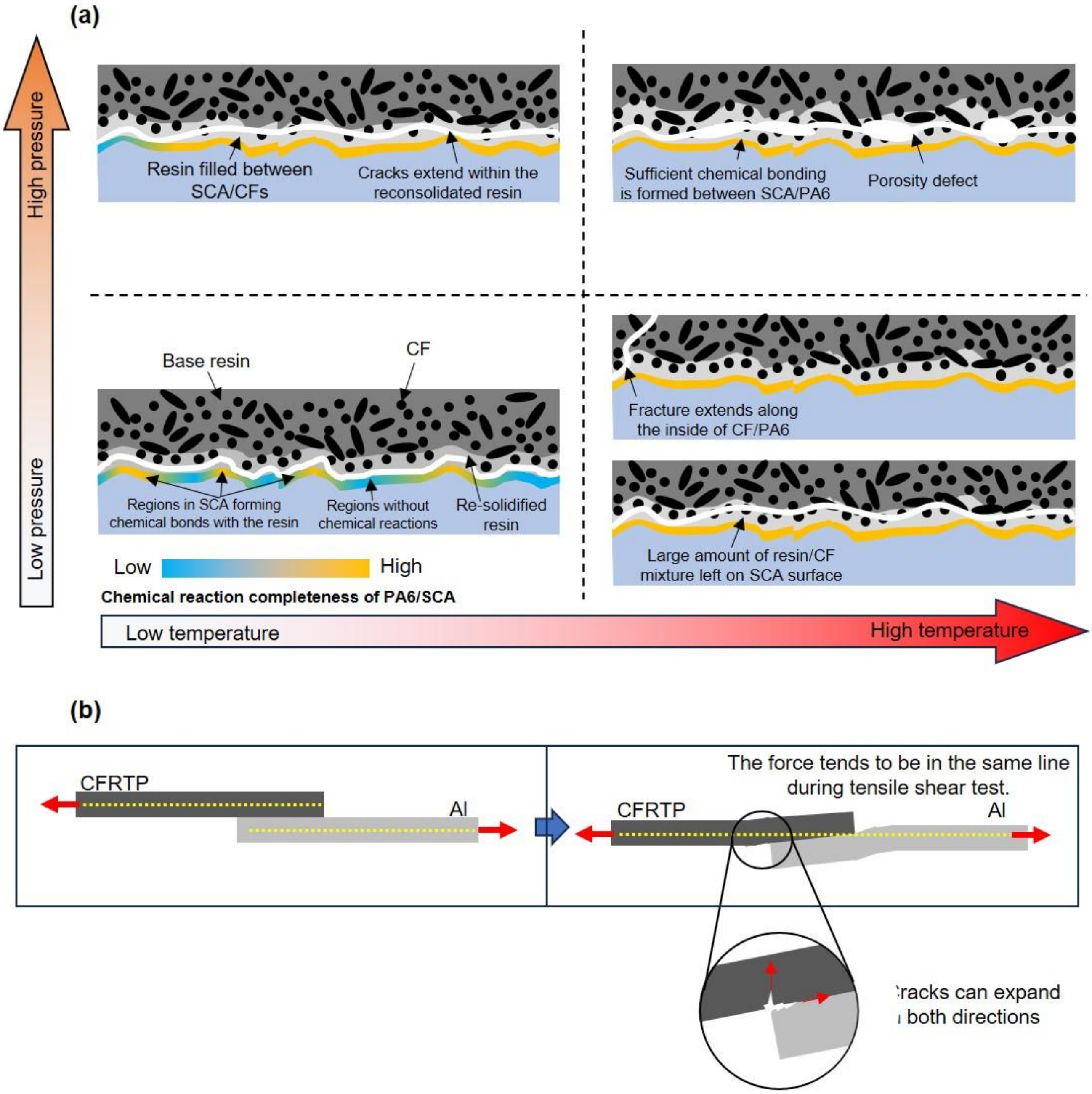

Fig. 28 (a) Fracture patterns and (b) crack extension modes.

Conversely, the effect of changing the pressure at higher temperatures on the interface is more complex than at lower temperatures. The viscosity of the resin in the vicinity of the interface decreases at higher temperatures, enabling lower pressures to sufficiently promote resin flow and penetration through the CFs to wet the silanized aluminum surfaces, resulting in sufficient chemical bonding to produce stronger joints. Two fracture modes occur in this situation: (1) a crack occurs between the CFRTP/SCA and inside the CFRTP, resulting in a residual CFRTP on the Al surface; and (2) the crack penetrates the interior of the CFRTP, directly leading to the fracture of the CFRTP itself, as shown in Fig. 28(a). The reason for this is shown in Fig. 28(b), where the tensile force did not follow a straight line in the single-lap tensile shear experiment, even though two shims were used to maintain a balanced clamping position. As the tensile-shear test progressed, the tendency for the tensile forces to be uniform results in bending of the CFRTP perpendicular to the tensile direction in the bonding region and generates bending stresses at the location of the CFRTP close to the joint. At the edge of the bonding area, the relatively sharp edge of the bent aluminum plate is attached on the surface of CFRTP, where the edges of the CFRTP are in a state of stress concentration. Cracking first occurred near the edge of the Al/CFRTP interface owing to stress concentration, as shown in Fig. 28(b). Fractures can occur along either the Al/CFRTP interface or the thickness direction of the CFRTP, marked by red arrows, depending on which side is stronger. Once the strength of the interface was sufficiently high and exceeded a certain threshold, the cracks propagated towards the thickness of the CFRTP, resulting in a fracture inside the CFRTP. The presence of both of these mechanisms makes the fracture behavior more unpredictable. Some localized strength inhomogeneities at the microscopic level contribute more dramatically to the overall fracture of the joint. This uncontrollable microscopic factor resulted in the occurrence of both fracture behaviors in multiple repetitive lap tensile shear tests.

On the other hand, the localized temperature of the molten resin inside the CFRTP under high-temperature joining conditions approaches the resin decomposition threshold. Simultaneously, more molten resin aggregates on the surface of silanized Al under high pressure, which increases the probability of resin decomposition in the molten state. Some of the PA6 resin matrix in the CFRTP decomposes into gaseous water and carbon dioxide at this moment, producing porous defects as shown in Fig. 26(f). The presence of the defects reduces the effective bonding area of the CFRTP near the weld interface and consequently decreases the strength. When fracture occurs in tensile shear test, cracks extend along such weak defects within the PA6 resin, resulting in a large amount of CFRTP remaining on the aluminum side after fracture as shown in Fig. 23(d).

4.5 Summary

In this study, we designed experimental equipment to address the post-joining thinning of CFRTP, which significantly affects the joint strength between Al and CFRTP. Concurrently, we systematically investigated the influence of pressure, temperature, and time on the bonding strength, and the mechanism of the improved mechanical properties by improving the bonding conditions was elucidated by SEM observations. The experiments yielded high-quality Al/CFRTP joints, laying the foundation for future metal composite joining and potential industrial applications. The following conclusions were drawn from this study:

(1) Improved hot-pressing process: The incorporation of down-pressure control in the isothermal hot-pressing process demonstrated notable improvements. By controlling the amount of compression, the melted and extruded CFRTP was substantially reduced, leading to a thicker joint, as seen in the cross-sections. Moreover, higher joining pressures, when combined with down-pressure control, allowed the achievement of a high lap tensile-shear force in a shorter time and at lower joining temperatures, highlighting the effectiveness of the improved process.

(2) Role of joining pressure in chemically bond formation: This study demonstrated the significant role of applied pressure in determining joint strength. For temperatures below 280 °C, an increase in joining pressure from 0.2 MPa to 0.8 MPa improved the joint strength. However, at 310 °C, increased joining pressure resulted in diminished joint strength. This underscores the importance of calibrating the temperature, residence time, and pressure to achieve optimal joint strength.

(3) Bonding mechanism: SEM micrographs revealed the intricate details of the Al/CFRTP interface under various conditions. The results indicate that optimal bonding and joint strength are obtained by establishing significant contact between the PA6 resin and the aluminum SCA layer. Increasing the temperature or pressure contributed to the formation of more molten PA6 resin in contact with the SCA layer, which enhanced the Al/CFRTP bonding.

(4) Fracture morphologies: Various pressure, temperature, and time conditions result in the development of a distinct fracture topography. The fractures mainly occurred between the CFRTP and SCA interfaces under low temperature and pressure conditions. However, as the pressure and temperature increased, the fracture gradually extended from the SCA surface to the interior of the CFRTP. Under appropriate thermal conditions, fractures can penetrate directly through the CFRTP. However, the crack extension path can be severely affected by defects caused by excessive heat input under high pressure and temperature conditions.

5. Interpretable Data-Driven Analysis

The construction of interpretable and predictive models that relate joining process conditions to interfacial microstructure and mechanical performance is essential for advancing the intelligent design and optimization of hybrid material joints. In the case of Al–CFRTP hot-press joining, this relationship is particularly complex due to the strongly coupled thermal, mechanical, and chemical phenomena occurring at the interface. Traditional modeling approaches often struggle to capture these nonlinear interactions comprehensively and transparently, limiting their utility in both theoretical studies and industrial implementation. In the preceding chapters, extensive experimental investigations were carried out under systematically varied hot-pressing conditions. Chapter 3 focused on the effects of heating temperature and holding time under fixed geometric constraint, revealing how thermal input governs interfacial chemical bonding, polymer flow behavior, and joint strength. Chapter 4 introduced a thinning-controlled joining strategy to modulate the effective pressure at the interface, highlighting its dual role in enhancing interfacial contact and potentially triggering void formation or resin loss. Across these studies, a wide range of interfacial features—including reaction layer thickness, void content, morphological roughness, and bonding quality—were quantitatively characterized using multi-scale tools such as SEM, TEM, XPS, and Raman spectroscopy. These features, along with precise thermal histories and mechanical performance outcomes, form a robust and multi-domain dataset that supports the development of a physically grounded predictive model.

To overcome the limitations of conventional modeling and fully utilize this dataset, this chapter proposes a systematic data-driven modeling framework that integrates experimental characterization, thermal simulation, machine learning, and symbolic regression. A comprehensive dataset encompassing joining parameters, interfacial features, and joint strength was first established under controlled hot-press conditions.

Physically meaningful and dimensionless features were extracted and used to train gradient boosted decision tree (GBDT) models, which effectively captured the multi-scale correlations among process, structure, and property variables. Beyond achieving high predictive accuracy, the model was further distilled into compact, interpretable mathematical expressions, enabling a clearer understanding of the dominant mechanisms governing joint strength. Feature importance analysis highlighted the trade-offs between interfacial chemical activation and thermal degradation, offering valuable insights into the optimization of joining conditions. This interpretable modeling framework not only facilitates parameter optimization but also provides a foundational tool for the extension of mechanistic insights to other thermally assisted joining processes. The contents of this chapter are organized as follows:

Section 5.1 describes the methodology for data acquisition and preparation, including process design, feature extraction, and thermal simulation.

Section 5.2 describes the construction of dimensionless metrics for uniform feature representation,

Section 5.3 presents the process of constructing the GBDT model and the interpretable model output method.

Section 5.4 presents the quantitative modeling results and evaluates model performance and variable importance.

Section 5.5 details the distillation of interpretable equations from the trained models.

5.1 Data acquisition and preparation

This chapter presents a systematic data-driven framework to analyze the coupled relationships among process parameters, interfacial microstructural characteristics, and joint performance during hot pressing. As illustrated in Fig. 29, the framework consists of four main steps: (1) data acquisition and preparation, including process design, interfacial characterization, and simulation-assisted parameter extraction; (2)

construction of physically meaningful and dimensionless feature sets; (3) regression modeling and feature importance analysis using GBDT; and (4) interpretable mathematical modeling. The methodology integrates multi-source experimental data, thermal simulation, physical parameter structuring, Machine Learning modeling, and mathematical model distillation.

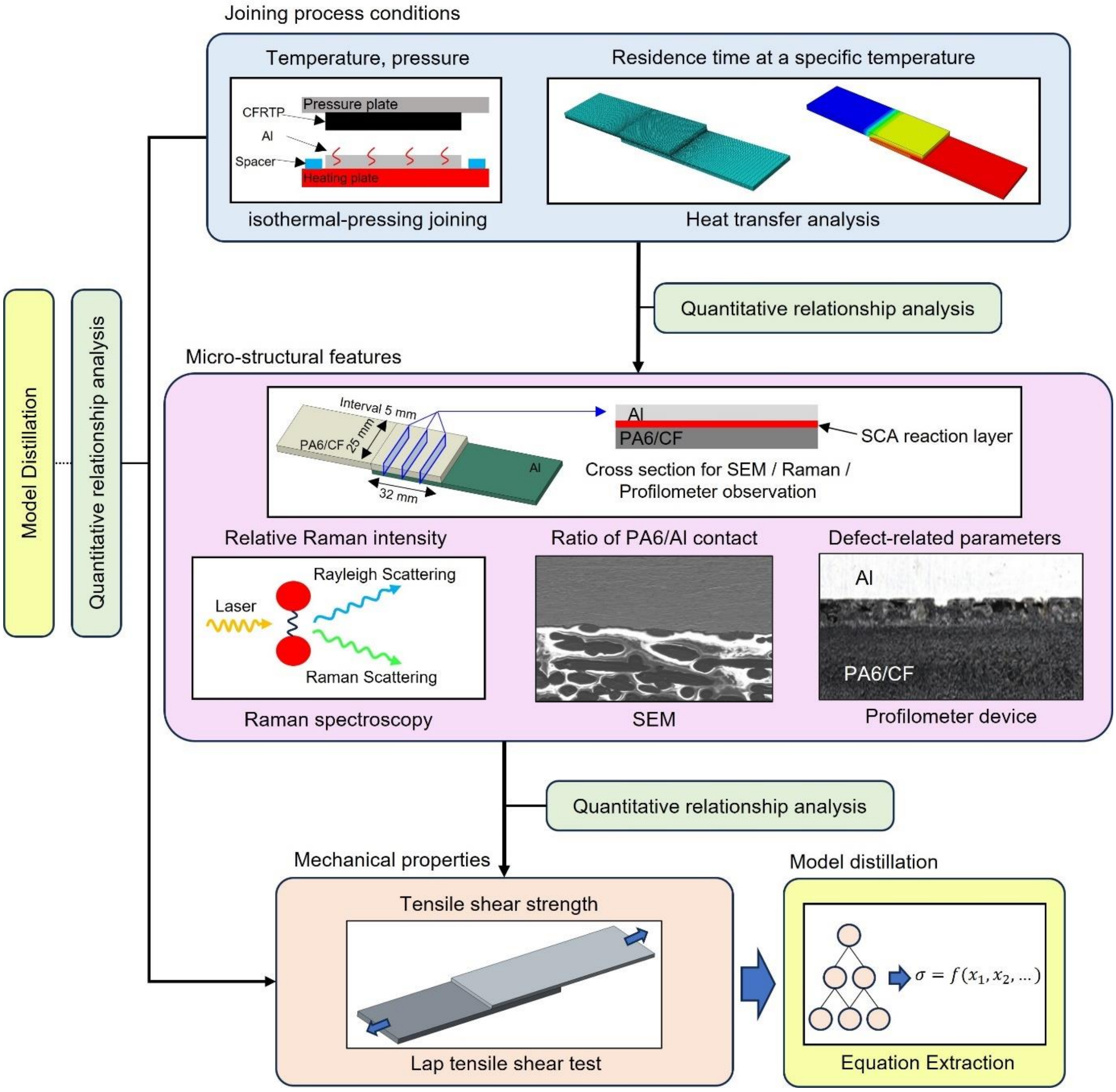

Fig. 29 Basic data-driven framework to analyze the coupled relationships among process parameters, interfacial characteristics, and joint strength of hot-pressed joined Al/CFRTP.

To enable the subsequent quantitative modeling of the joining process, this study systematically collected multi-source data related to process conditions, interfacial characteristics and joining strength. The CFRTP consisted of a 3 mm-thick PA6-based composite reinforced with randomly distributed 20 vol% short fibers, which was joined with a 2 mm-thick commercial AA5052-O. Experimental joining of Al alloy and CFRTP was carried out under well-controlled thermal and pressure conditions using a hot-pressing device. Detailed information regarding the hot-pressing device and preparation of Al and CFRTP base sheet has been provided in the chapter 2 and chapter 3. Lap joining was conducted with an overlapping area of 25 mm × 32 mm. Key joining parameters such as temperature, heating time, and pressure were precisely controlled and monitored. The studied joining parameters are listed in Table 6. To efficiently explore the key thermos-mechanical effects without incurring the high experimental cost of a full-factorial design, a space-filling sampling strategy was adopted in this study[42,43]. Specifically, the selected parameter combinations span both boundary conditions and diagonal trajectories across the parameter space defined by temperature, pressure, and heating time, as illustrated in Fig. 30. The joining strength was evaluated through single-lap shear tests under standard loading conditions. A simplified two-dimensional heat transfer model was constructed in Abaqus to capture real-time temperature distribution at the interface during hot-pressing joining. Detailed modeling information and simulation validation can also be found in the chapter 2. Key thermal indicators, such as the maximum temperature, the residence time of the bonding interface above the melting temperature (220 °C) and above the decomposition temperature range (340 °C - 420 °C) were extracted from the simulated temperature field. Detailed steps will be discussed in the following sections.

Additional data collection included interfacial chemical reaction intensity, assessed by Raman spectroscopy, and effective contact area ratio, identified via scanning electron microscopy (SEM). Defect features, such as defect count, aspect ratio, relative area, and defect layer thickness, were quantified using a 3D profilometer. For each joint, three cross-sections spaced 5 mm apart across the overlap region were selected for measurement to capture representative morphological features, and the average values were used for subsequent analysis, as shown in Fig. 29. More information on the defect feature determination is also provided in the Supplemental materials. All the extracted features were subsequently processed into dimensionless form and used as input variables for ML modeling, as described in the following sections.

Table 6 Hot pressing joining conditions used in this study.

Joining conditions	Joining temperature T_j(°C)	Heating time $t_H(s)$	Pressure $P_j(MPa)$
Value	250~420	1~3	0.2~0.8

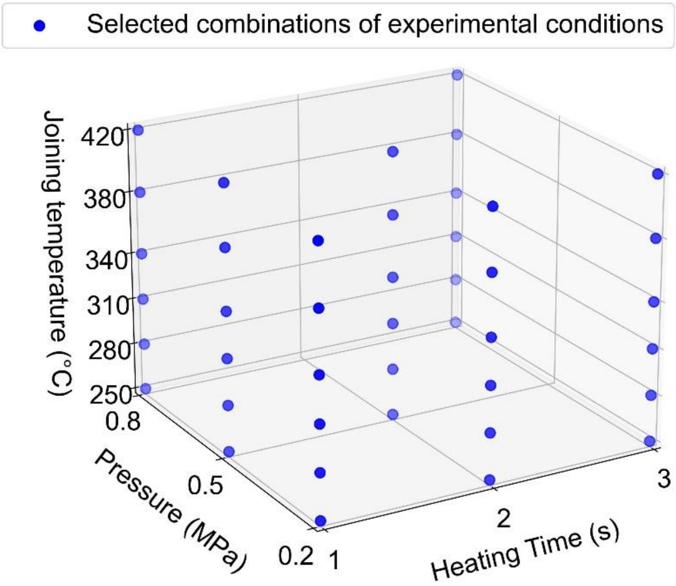

Fig. 30 Space-filling sampling strategy.

5.2 Features construction and dimensionless processing

In the modeling of multi-physics coupled systems, dimensionless processing is a commonly used and effective simplification method. It can unify different physical quantities under the same scale, which can reveal the intrinsic connection between the variables and enhance the interpretability and applicability of the model. Its theoretical basis can be traced back to the classical Buckingham π-theorem, which states that a system containing n physical variables involving k independent fundamental measures can be completely described by n-k dimensionless parameters (π-groups) to describe its behavior. In this study, the basic idea of the theorem is referred to in the dimensionless construction process. Combining with the understanding of the mechanisms of heat transfer, interfacial reaction and structural evolution in the hot-pressing, key variables are selected to construct dimensionless combination parameters with clear physical significance. In contrast to the automated parameter search method based on matrix derivation and data-driven approach, a customized "physics-driven + engineering-experience-driven" path is adopted in this paper, which emphasizes the causal connection between variables and the expression of dominant mechanisms. This approach has been widely used in CFRP-related research [44,45]. In the process of variable combination, the following construction principles are considered:

(i) Variables with clear physical meaning and significant control mechanisms are selected.

(ii) There is no redundancy between dimensionless parameters as far as possible, and the parameters are self-consistent.

(iii) The combination of variables needs to reflect the physical chain structure of "input-process-output", which is convenient for subsequent modeling and physical interpretation.

Based on this, all features collected in this study were categorized into three groups: process conditions, microstructural features, and joining strength, as summarized in Table 7. The details are described below:

i) Process conditions describe the macroscopic thermal-mechanical environment applied during joining, including the dimensionless maximum temperature θ_T^*, dimensionless applied pressure θ_P^*, and thermal exposure indicators such as melting residence ratio θ_M^*, decomposition residence ratio θ_D^*, and their combination as the decomposition-to-melting time ratio θ_{DM}^*. These features reflect the intensity and duration of thermal input affecting resin flow and degradation.

ii) Microstructure features represent interfacial chemical and physical characteristics that evolve due to heat and pressure. This includes dimensionless Raman intensity δ_{Ir}^* indicating chemical bonding strength, normalized contact area ratio δ_{ca}^* representing the bonded region, and dimensionless complex viscosity δ_v^* reflecting resin flowability. Defect-related parameters such as normalized layer thickness of defect δ_L^*, defect count δ_N^*, normalized defect area δ_{Ar}^*, and average defect aspect ratio δ_{dhl}^* characterize interfacial voids and imperfections. Among these, δ_{Ir}^*, δ_{ca}^*, and δ_v^* are classified as positive factors due to their beneficial contributions to joint performance, while δ_L^*, δ_N^*, δ_{Ar}^*, and δ_{dhl}^* are considered negative factors as they reflect interfacial degradation or instability.

iii) Joining strength is quantified by the dimensionless parameter σ_r^*, derived from single-lap shear testing divided by the tensile strength of the base resin PA6.

Table 7 Parameters and symbols after dimensionless.

Feature groups	Feature variables	Symbol
Process Conditions	Dimensionless Max Temperature	θ_T^*
	Dimensionless Applied Pressure	θ_P^*
	Melting Residence Ratio	θ_M^*
	Decomposition Residence Ratio	θ_D^*
	Decomposition-to-Melting Time Ratio	θ_{DM}^*
Microstructure Features	Dimensionless Raman intensity	δ_{Ir}^*
	Effective Contact Area Ratio	δ_{ca}^*

	Dimensionless Complex Viscosity	δ_v^*
	Normalized Layer Thickness of Defect	δ_L^*
	Defect Count	δ_N^*
	Normalized defect area	δ_{Ar}^*
	Average Defect Aspect Ratio	δ_{dhl}^*
Joining strength	Dimensionless Strength	σ_r^*

5.2.1 Process conditions of hot-pressing joining

Dimensionless Max Temperature

In the joining process, the maximum temperature reached during joining plays a critical role in determining the thermal response of the polymer matrix. To effectively describe the temperature effect in a dimensionless form, we define the *Dimensionless Max Temperature* θ_T^* as the ratio of the maximum joining temperature ($T_{joint,max}$) to the decomposition temperature of PA6 ($T_{deco,PA6}$):

$$\theta_T^* = \frac{T_{joint,max}}{T_{deco,PA6}} \tag{5}$$

where $T_{deco,PA6} = 340°\mathrm{C}$. This dimensionless parameter reflects the degree to which the joining temperature approaches the thermal stability limit of PA6, A higher value indicates that the temperature is approaching or exceeding the decomposition threshold.

Dimensionless Applied Pressure

The applied pressure significantly influences material deformation and interfacial bonding. To express this effect in a dimensionless form, we define the *Dimensionless applied Pressure (θ_P^*)* as the ratio of the applied pressure (P_{set}) to the tensile strength of PA6 at room temperature ($\sigma_{max,PA6}$):

$$\theta_P^* = \frac{P_{set}}{\sigma_{max,PA6}} \tag{6}$$

where $\sigma_{max,PA6} = 60\ MPa$.

Thermal Residence Time Ratios

The residence time during which the interface temperature exceeds specific thermal thresholds plays a critical role in the melting of CF/PA6, chemical reactions at the interface, and potential thermal degradation. Unlike traditional approaches that rely solely on preset heating durations, residence times above characteristic temperatures more accurately reflect the actual thermal environment at the joining interface [38]. In this study, heat transfer simulations were conducted to extract thermal histories at the interface, which are difficult to measure directly during the joining process. Based on these histories, as shown in Fig. 31, the average residence time along the length direction above 220 °C was defined as the **melting residence time** (t_{melt}), and which above 340 °C was defined as the **decomposition residence time** (t_{deco}). Their ratio, the **melting-to-decomposition time ratio,** reflects the balance between effective bonding time and thermal damage risk.

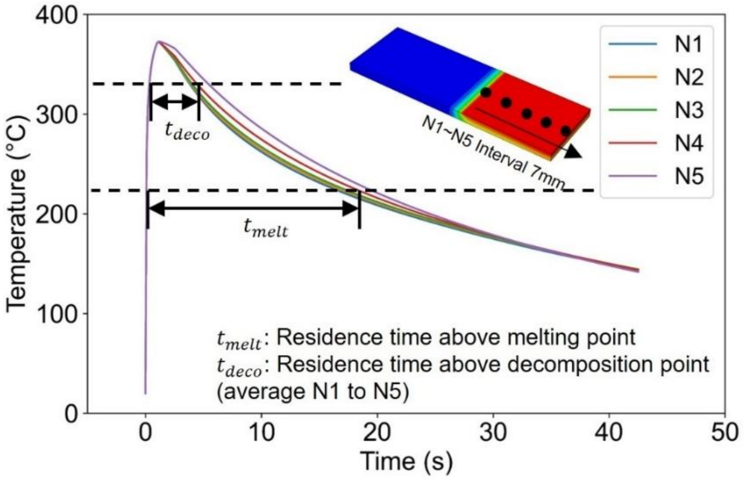

Fig. 31 The temperature histories along the length direction of the Al-CF/PA6 interface under the heating condition of 380°C - 1s.

To dimensionless these time-related parameters, we introduce the thermal diffusion time (t_{diff}) as a reference, representing the characteristic time for heat to diffuse through a given material length. The concept originates from the Fourier heat conduction equation [46,47]:

$$\frac{\partial T}{\partial t} = \alpha \nabla^2 T \tag{7}$$

Here, α denotes the thermal diffusivity, defined as:

$$\alpha = \frac{k}{\rho c_p} \tag{8}$$

where k is thermal conductivity, ρ is density and c_p is specific heat capacity. Using the separation of variables method, the solution takes the form:

$$T(x,t) = X(x) \cdot \tau(t) \tag{9}$$

After substitution and separation, the characteristic time can be derived as:

$$t_{diff} = \frac{L^2}{\alpha} \tag{10}$$

This characteristic time indicates the period required for heat to diffuse through a characteristic length L (~1mm for this study). In the context of hot-pressing joining, it represents the time scale over which the temperature field reaches a quasi-steady state within the material. To systematically evaluate the effect of heat on joint formation, we introduced the following dimensionless residence time ratios in conjunction with the thermal diffusion time:

$$\text{Melting Residence Ratio } \theta_M^* = \frac{t_{melt}}{t_{diff}} \tag{11}$$

$$\text{Decomposition Residence Ratio } \theta_D^* = \frac{t_{deco}}{t_{diff}} \tag{12}$$

$$\text{Decomposition-to-Melting Time Ratio } \theta_{DM}^* = \frac{D_r}{M_r} \tag{13}$$

where θ_M^* and θ_D^* quantify the time for the material remaining in the melt and decomposition states versus the time required for heat to diffuse through the joint, respectively. θ_{DM}^* directly compares the time for the material to remain above the decomposition and melting points, highlighting the relative thermal stability of the joining process.

5.2.2 Microstructure features

Dimensionless Raman intensity

In the joining process between Al and CF/PA6, the chemical bonding at the interface plays a critical role in determining the joining strength. The content of epoxy groups in the silanized treatment layer (SCA) on the aluminum surface decreases by reflecting with the PA6 polyamide matrix, which leads to a decrease in the intensity of the Raman intensity. To quantitatively characterize the reaction extent, the Dimensionless Raman intensity (δ_{Ir}^{*}) is defined as:

$$\delta_{Ir}^{*} = \frac{i_{epoxy}}{i_{Si}} \tag{14}$$

where i_{epoxy} is the intensity of the epoxy group peak in the Raman spectrum. i_{Si} is the intensity of the Si peak as a reference. The *Si* peak originating from the SCA itself remains relatively stable, providing a consistent baseline for comparison. This ratio directly reflects the extent of the chemical reaction between the treated Al surface and the molten CF/PA6.

Effective Contact Area Ratio

The regions where Al directly contacts PA6, or Al directly contacts CF exhibit distinct chemical reaction characteristics [48]. Therefore, we define the Effective Contact Area Ratio (δ_{ca}^{*}) as the proportion of the Al-PA6 contact length to the total interface length, as shown in Fig. 32:

$$\delta_{ca}^{*} = \frac{A_{Al/PA6}}{A_{total}} \tag{15}$$

where $A_{Al/PA6}$ is length of the interface where Al and PA6 are in direct contact. A_{total} is total length of the interface between Al and CF/PA6 (~25mm).

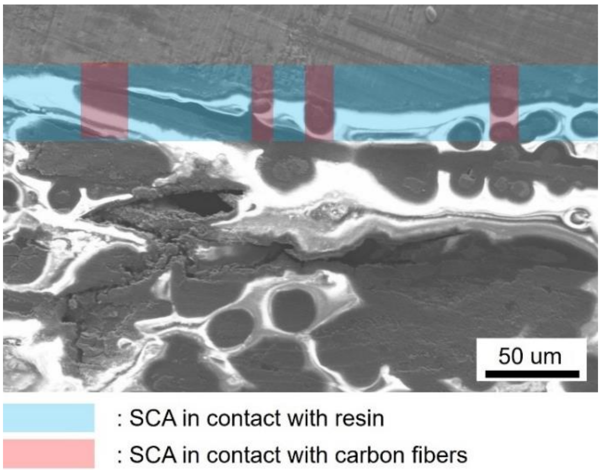

Fig. 32 The localized SEM structure of the Al-CF/PA6 interface under the heating condition of 340°C - 1s, with different contact locations marked.

Dimensionless complex viscosity

The fluidity of PA6 resin directly affects the wetting ability of the molten resin on the Al surface and the filling of voids, which indirectly affects the sufficiency of the chemical reaction. We introduce the complex viscosity of PA6 resin into the model to characterize the potential effect of flow more accurately on joint formation. The complex viscosity data of PA6 at different temperature conditions were obtained from other study [49]. For the temperature ranges not covered in the paper, we estimate them based on the reported trends of viscosity changes using a reasonable interpolation method. The typical complex viscosity of PA6 near the melting point temperature of 220°C were used as a reference value to achieve the dimensionless. The Dimensionless complex viscosity is defined as:

$$\delta_v^* = \frac{\eta_{PA6}}{\eta_{PA6,220℃}} \tag{16}$$

Defect Parameters

Interfacial defects can significantly affect joint performance and may disrupt the bonding effect between aluminum and CF/PA6. Several dimensionless parameters are introduced to characterize the morphology and distribution of defects at the bonding interface, providing a quantitative assessment of the impact of these defects on the joint properties.

Fig. 33(a) shows the height distribution of the joint cross-section obtained by scanning with the three-dimensional profiler. A defect with an area of more than 50 × 50 pixels is defined as a defect to minimize the interference caused by the unevenness of the sample. The number of defects (δ_N^*) represents the total number of defects detected in the cross-sectional image, directly reflecting the defect density at the weld interface, as a dimensionless parameter. Normalized defect area (δ_{Ar}^*) is used to characterize the ratio of defect area relative to the joint cross-sectional area and is calculated as:

$$\delta_{Ar}^* = \frac{A_{defect}}{A_{joint}} \tag{17}$$

where A_{defect} is weighted average of the defect area obtained from the cross-sectional image. A_{joint} is area of the joint cross-section (~125 mm²). In addition, the average defect aspect ratio (δ_{dhl}^*) is defined as the ratio of defect height (H_{defect}) to defect length (L_{defect}):

$$\delta_{dhl}^* = \frac{H_{defect}}{L_{defect}} \tag{18}$$

This parameter reflects the geometrical characteristics of interfacial voids or cracks and provides a direct evaluation of defect morphology changes.

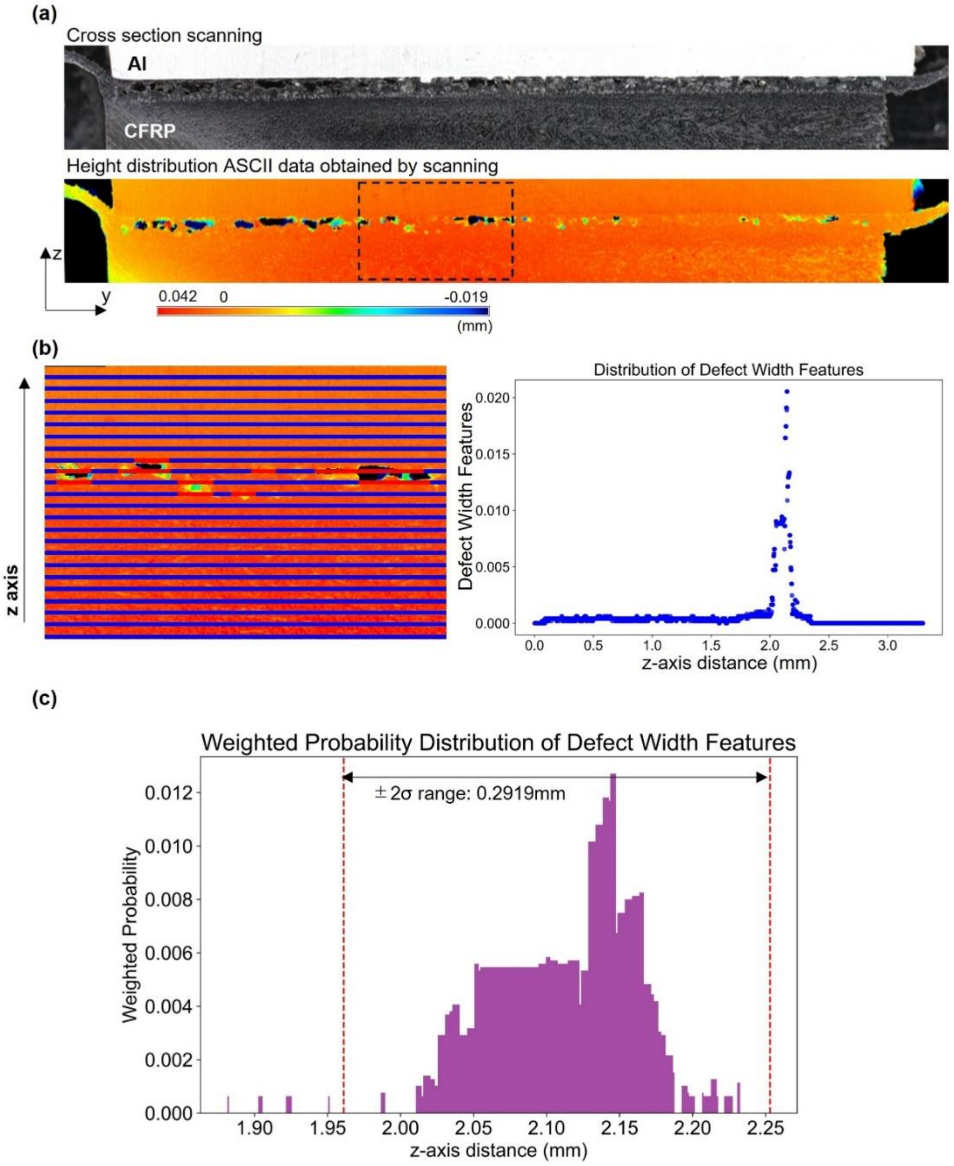

Fig. 33 (a) The height distribution obtained by profilometer scanning, (b) the pattern of detecting defect features by ASCII information and (c) the weighted distribution of defect features.

In welded interfaces, the thickness of the defect layer is also an important parameter for predicting the quality of the interface bond and the potential risk of failure. To quantify the thickness of the defective layer, we first processed the ASCII codes obtained from the profilometer, which contain three-axis coordinate information about the shape of the joint. On each scan line aligned along the Z-direction, the defect region (red line in Fig. 33b) and the total scan width (blue line in Fig. 33b) are detected using our own developed script. The ratio of the length of the red line to the length of the blue line is calculated and defined as Defect Width Features (DWF). A weighted distribution analysis of all DWF values is performed, as shown in Fig. 33(c). Based on the distribution curves, ± 2 times the standard deviation range is used as the range to define the defect layer thickness to avoid possible interference. The interface width (25 mm) was used as a reference value for us to achieve the dimensionless of the defective layer thickness, which is expressed as:

$$\delta_L^* = \frac{t_{defect}}{w} \tag{19}$$

5.2.3 Joining Strength

Joining strength (σ) obtained by single lap shear experiments is an important indicator of joint quality, defined as the maximum tensile load (F_{max}) divided by the overlap area ($A_{overlap}$):

$$\sigma = \frac{F_{max}}{A_{overlap}} \tag{20}$$

To make the joining strength comparable, we introduce the Dimensionless strength (σ_r) as a dimensionless parameter. The tensile strength of PA6 ($\sigma_{max,PA6}$) is used as the reference value for dimensionless and is defined as follows:

$$\sigma_r^* = \frac{\sigma}{\sigma_{max,PA6}} \tag{21}$$

where $\sigma_{max,PA6} = 60\ MPa$.

5.3 Quantitative modeling and functional relationship extraction

After completing the dimensionless processing, the GBDT method was used to construct three types of quantitative relationship models as shown in Fig. 29: mapping of process conditions to microstructure features, mapping of microstructure features to joining strength, and direct mapping of process conditions to joining strength, respectively. The model performance is evaluated through the metrics of the coefficient of determination (R^2), mean squared error (MSE) and mean absolute error (MAE) on the training and test sets. As illustrated in Fig. 34(a), generalization capability analysis is performed to ensure the model's adaptability beyond specific parameters. Additionally, key factors affecting various response variables are identified through feature importance analysis. The key factors will be used to analyze the physical relationship between process parameters-microstructure-strength. To address the “black box” problem of GBDT models in terms of interpretability, the study further introduces a model distillation strategy to extract simplified function expressions from the original prediction models. The correlation and interpretability analyses between features were first performed to eliminate redundant variables and simplify inputs as shown in Fig. 34(b). Subsequently, the mathematical expressions are extracted by fitting the relationship function between key features and compared with the original GBDT model to improve the accuracy, thus enhancing the engineering applicability and theoretical value of the model.

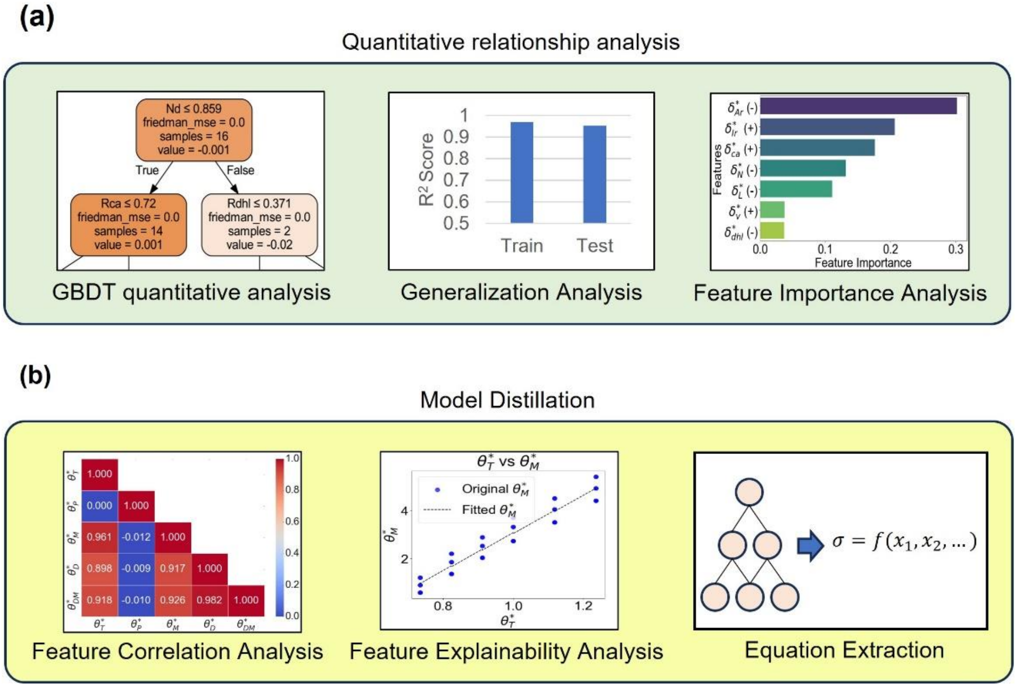

Fig. 34 (a) Quantitative modeling and (b) model distillation.

5.4 Quantification relationship analysis results and discussion

5.4.1 Process conditions and microstructure features

To quantitatively predict the effects of process conditions on microstructure features, a series of regression models based on gradient boosted decision trees (GBDT) have been developed. GBDT is a powerful machine learning algorithm that integrates multiple weak learners (i.e., decision trees) into one strong learner by iteratively minimizing the residual error. In this study, we built separate GBDT models (GBDT_model1 to GBDT_model7) for each microstructure feature, as shown in Fig. 35. The inputs to each model are the five process conditions after dimensionless quantization.

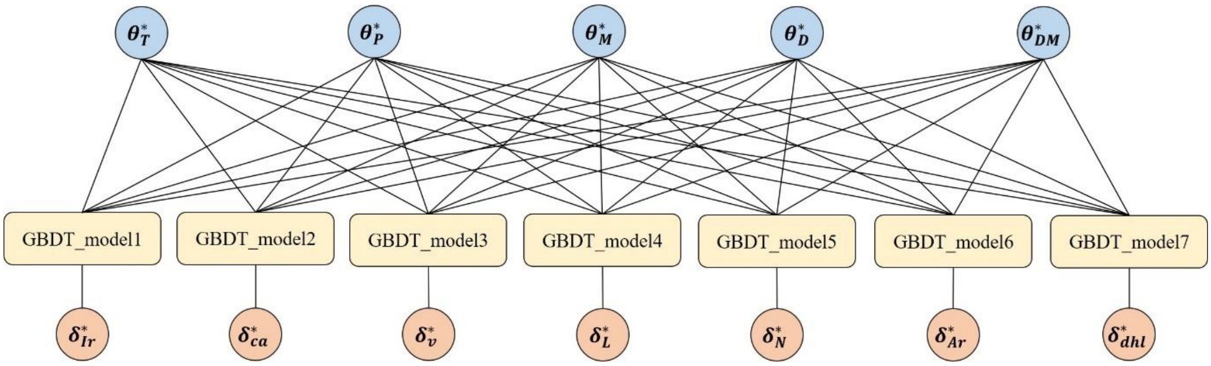

Fig. 35 Illustration of machine learning of process conditions on microstructure features.

The model hyperparameters were optimized to improve the generalization ability and stability of the model. To balance predictive accuracy and generalization capability, a combination of grid search and manual adjustment was employed for hyperparameter tuning [50], aiming to avoid overfitting and achieve robust performance on both training and testing datasets. Key parameters such as the number of estimators, tree depth, learning rate, and subsample ratio were optimized accordingly. The collected data were independently divided into 80% training set and 20% testing set, and the model performance was evaluated on these two sets to ensure that the model has sufficient generalization ability and scalability by R^2, MAE and MSE. Through this modeling approach, we aim to quantitatively link the hot-pressing conditions with the resulting microstructural features, thereby gaining a deeper understanding of the complex interrelationships between process parameters and joint performance.

Fig. 36 shows the predicted values (vertical coordinates) versus the original values (horizontal coordinates) for each micro-feature to visualize the predictive effect of the model. The diagonal line (y=x) in the plots represents the ideal state where the predicted values are in perfect agreement with the original values. The comparison shows that the predicted values of most of the features are well distributed near the diagonal line, indicating that the model fits the data better on both the training and test sets. However, the predicted values of some of the microscopic features (e.g., δ^*_{dhl} and δ^*_N) show some deviations on the test set, indicating that the model tends to overfit these features to some extent. This may be due to the fluctuation of these features by the process conditions, meanwhile, the unevenness of the scanned plane also interferes with the recognition of depressions, causing the model to show instability in processing these features.

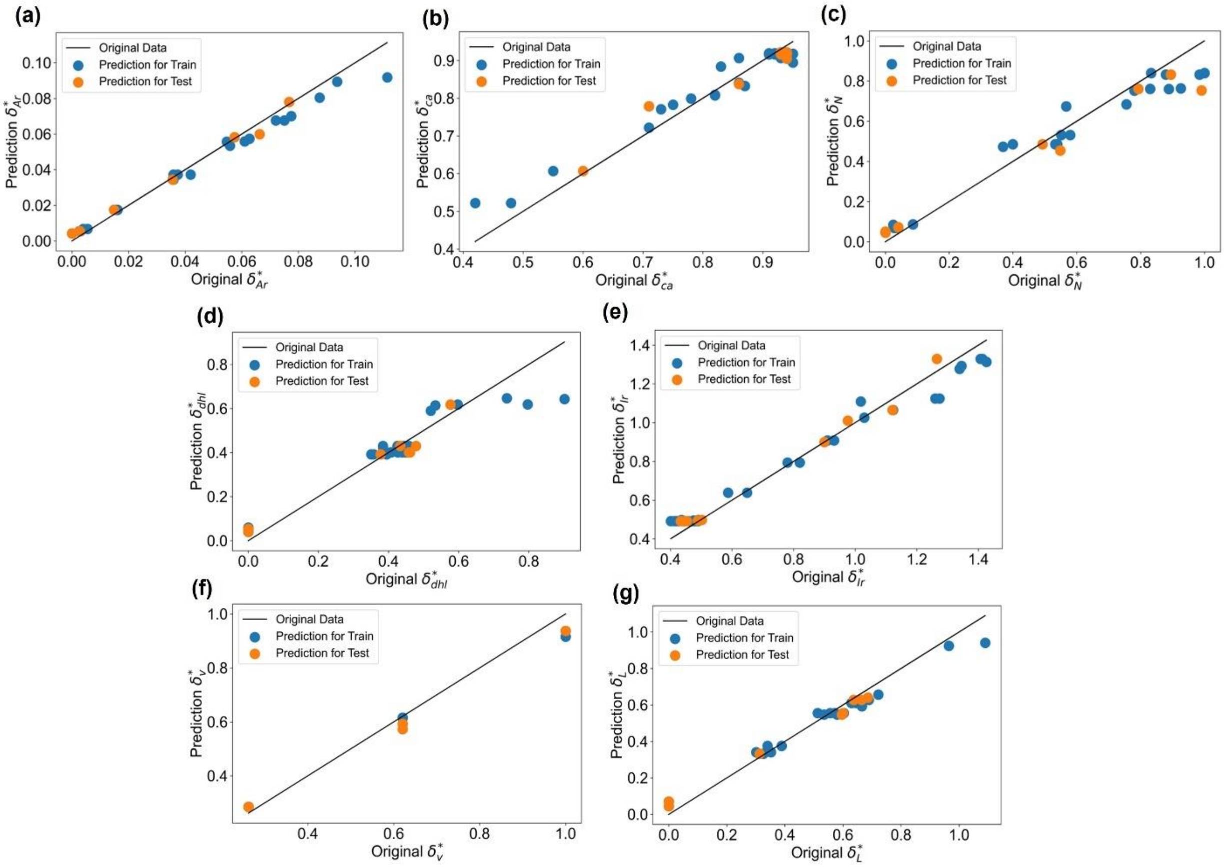

Fig. 36 The predicted values versus the original values of (a) normalized defect area-$\boldsymbol{\delta^*_{Ar}}$, (b) effective contact area ratio$-\boldsymbol{\delta^*_{ca}}$, (c) defect count-$\boldsymbol{\delta^*_N}$, (d) average defect aspect ratio$-\boldsymbol{\delta^*_{dhl}}$, (e) dimensionless Raman intensity-$\boldsymbol{\delta^*_{Ir}}$, (f) dimensionless viscosity-$\boldsymbol{\delta^*_v}$, (g) normalized layer thickness of defect-$\boldsymbol{\delta^*_L}$.

To evaluate the overall fitting performance of the model, we compared the R², MSE, and MAE metrics across the training, testing, and all-sample datasets, as shown in Fig. 37.

This allows for a global assessment of the model's prediction accuracy on both seen and unseen data. The R² of the models from different features is generally high through statistical analysis, in which the R² of the training set is generally higher than 0.92, and the R² of the test set is generally higher than 0.90, indicating that the model has a better fitting effect and a higher prediction accuracy, as shown in Fig. 37(a). The R² of features δ_{Ir}^*, δ_v^*, δ_L^* and δ_{Ar}^* reached above 0.95 on both the training and test sets, indicating that the model's prediction on these features is particularly good. In terms of errors, the MSE of most of the microscopic features is in the range of 0.0005 to 0.002, and the MAE is in the range of 0.015 to 0.05, where the errors of δ_{ca}^* and δ_{Ar}^* are relatively low, indicating that the model has a high prediction accuracy for these features, as shown in Fig. 37(b) and Fig. 37(c). The prediction errors for δ_N^* and δ_{dhl}^*, on the other hand, are relatively large, with a maximum MSE value of about 0.0086 and a maximum MAE value of about 0.067. The results of the proportions of MSE and MAE relative to the range of variation of the original data (black plots) show that the relative MSE is lower than 0.5% and the relative MAE is lower than 5% for most of the features. It indicates that the model prediction errors account for a relatively low percentage of the original data range, and the prediction effect is relatively reliable. The maximum relative MSE and MAE are obtained from δ_N^* and δ_{dhl}^*, which reached 0.86% and 6.7%, respectively, but are still within acceptable limits. These results also reflect the model's generalization capability. As shown in Fig. 37, the prediction metrics on both training and test sets are highly consistent, with typical MSE and MAE differences remaining below 0.001 and 0.01, respectively. This consistency suggests that the model avoids significant overfitting and maintains stable performance on unseen data. Features such as δ_{ca}^* and δ_v^* exhibit particularly low error variation. Relatively larger discrepancies observed in δ_N^* and δ_{dhl}^* indicate that defect-related features are more sensitive and less accurately predicted. This may be attributed to the inherent limitations of defect data acquisition, which relies on sampling from a limited number of cross-sectional planes. Such an approach inevitably introduces a degree of information loss. Enhancing the spatial resolution—either by increasing the number of cross-sections or by employing advanced three-dimensional imaging techniques—could further improve the accuracy and robustness of defect characterization and model predictions.

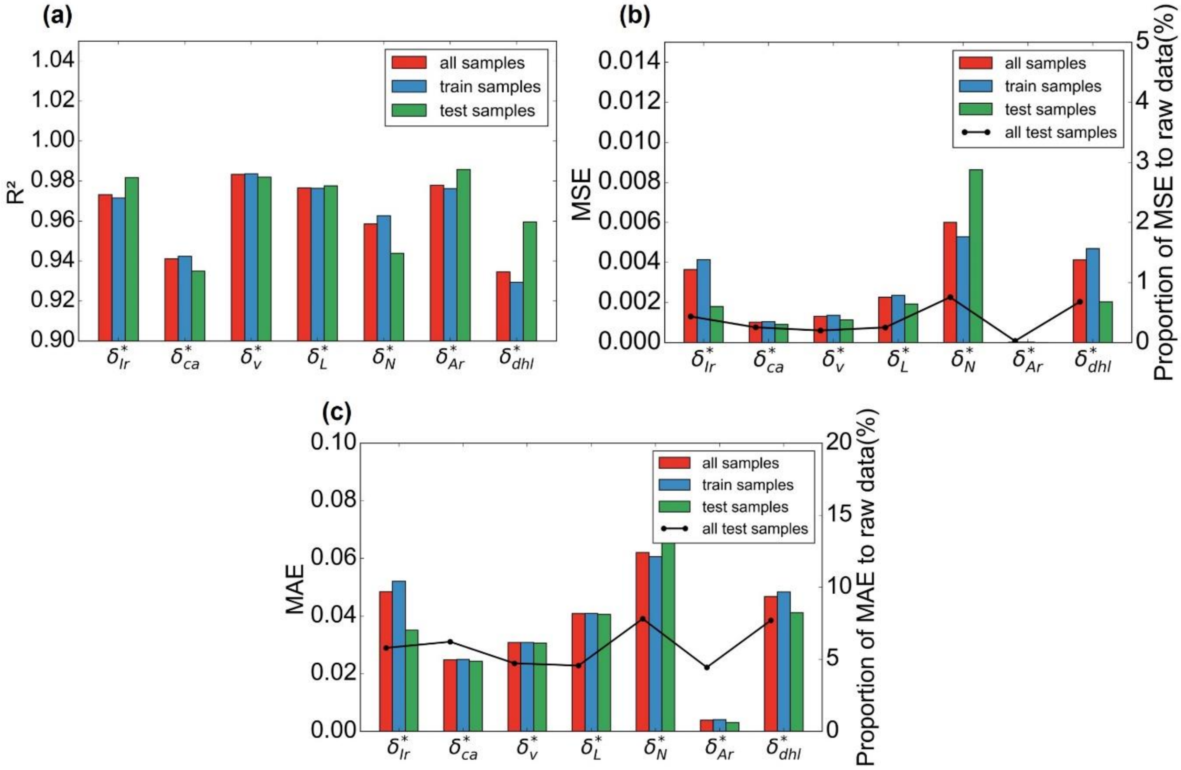

Fig. 37 Evaluation metrics for predictive capacity of each output: (a) coefficient of determination-R², (b) mean squared error-MSE and (c) mean absolute error-MAE.

As shown in Fig. 38, the influence of different process parameters on microstructural features was investigated to elucidate variations in feature importance. Additionally, Fig. 39 illustrates the response trends of key microstructure features to process conditions, with fitted quadratic regression curves highlighting the nonlinear characteristics. For microstructural indicators related to chemical bonding, such as δ^*_{Ir} and δ^*_{ca}, the highest feature importance was observed for θ^*_T and θ^*_M. This result can be physically explained based on existing studies on melt flow and interfacial chemistry. With increasing temperature and melting duration, the viscosity of PA6 resin decreases significantly, enhancing its wetting behavior at the Al interface. Molecular dynamics simulations have shown that the contact angle of thermoplastic resins reduces with temperature and time, leading to better spreading over the substrate surface [49,51,52]. Furthermore, for interfacial chemical bonding, the formation of key amide groups (amide C–N and amide N–H) between PA6 and the silane coupling agent (SCA) relies on the activation of interfacial reactions that require the cracking of epoxy groups in the SCA. Molecular dynamics simulations have shown that the interfacial binding energy of the epoxy group remains relatively stable at lower temperatures but begins to decline notably around 180 °C ~260 °C, indicating the onset of epoxy cracking and reactivity enhancement. As the temperature continues to rise, the interfacial energy decreases further and stabilizes beyond approximately 340 °C, suggesting that the epoxy groups have been fully activated and the interfacial chemical bonding process approaches completion [53,54]. This two-stage energetic behavior reflects the temperature-dependent molecular reconfiguration needed for covalent bond formation. Thus, θ_M^* ensures that sufficient wetting and molecular proximity are achieved for reactions to initiate, while θ_T^* governs whether the interface acquires enough energy to trigger epoxy opening and sustain full reaction progress. Their combined effect facilitates the formation of stable amide linkages, which is a critical mechanism for enhancing the bonding performance between PA6 and Al.

In addition, the θ_P^* helps to increase the contact area between Al and CF/PA6. Higher pressures lead to resin flow and deformation, thus inducing closer contact between PA6 in the molten state and the aluminum surface, which is consistent with experimental observations in chapter 4. Nevertheless, among all microstructural features, the θ_P^* consistently showed low importance in most prediction tasks. This may be attributed to the nature of hot-pressing process, where temperature-induced viscosity reduction plays a dominant role in resin mobility compared to externally imposed mechanical forcing.

Therefore, relaxing or simplifying the pressure control requirements, and thus reducing equipment complexity and control costs, may be feasible without seriously affecting the quality of the joint.

In contrast, for defect-related features including δ_L^*, δ_N^*, and δ_{Ar}^*, decomposition residence ratio (θ_D^*) emerges as a critical variable. This reflects the tendency of excessive thermal exposure to initiate resin degradation. PA6 is known to thermally degrade around 340–350 °C and shows rapid decomposition above 400 °C, with a sharp mass loss due to chain scission reactions [55]. Thermal degradation leads to defect nucleation and interfacial void formation, which propagates deeper into the interface as thermal penetration increases. Regression trends in Fig. 39 further reveal key threshold phenomena: δ_{Ir}^* and δ_{ca}^* approach saturation near $\theta_T^* \approx 0.9$ (~340 °C), beyond which further heating does not enhance bonding and instead promotes defect growth in δ_L^* and δ_{Ar}^*. Meanwhile, degradation indicators such as θ_{DM}^* show steep increases in δ_{Ar}^* and δ_N^* when exceeding ~0.6, indicating entry into a rapid degradation regime.

These findings underscore the trade-off between bonding enhancement and defect suppression. A single-objective parameter optimization approach cannot simultaneously satisfy the requirements of all microstructural features. Therefore, process tuning strategies must be flexibly designed according to the targeted outcomes. Striking a balance between chemical activation and thermal degradation is essential for achieving both high joint quality and structural reliability.

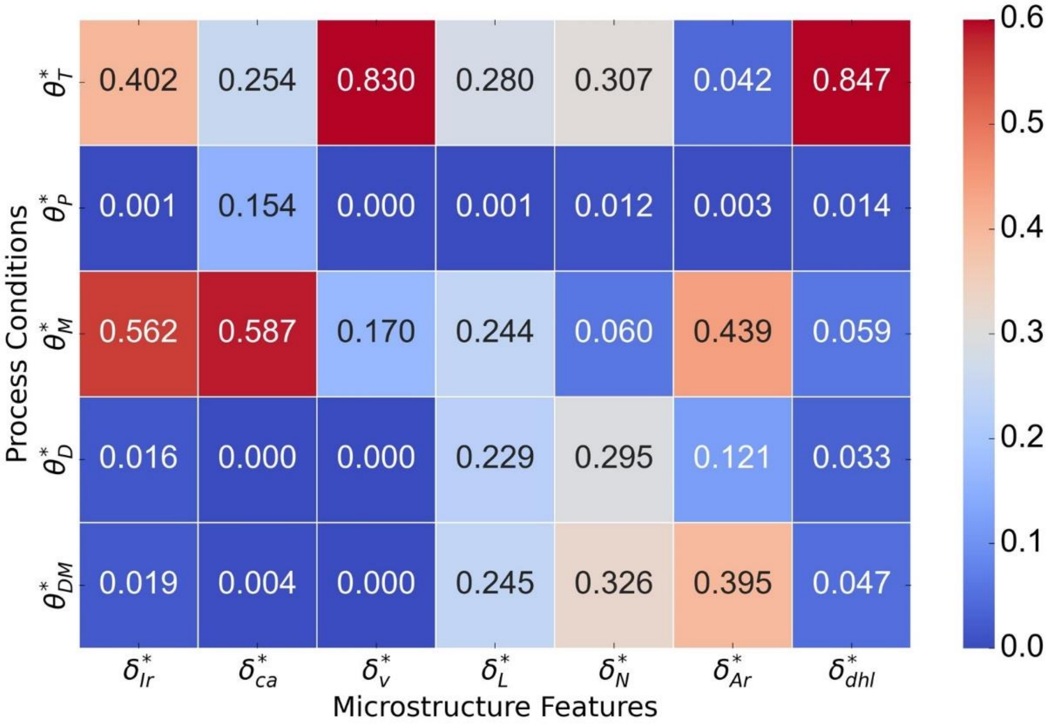

	δ^*_{lr}	δ^*_{ca}	δ^*_{v}	δ^*_{L}	δ^*_{N}	δ^*_{Ar}	δ^*_{dhl}
θ^*_T	0.402	0.254	0.830	0.280	0.307	0.042	0.847
θ^*_P	0.001	0.154	0.000	0.001	0.012	0.003	0.014
θ^*_M	0.562	0.587	0.170	0.244	0.060	0.439	0.059
θ^*_D	0.016	0.000	0.000	0.229	0.295	0.121	0.033
θ^*_{DM}	0.019	0.004	0.000	0.245	0.326	0.395	0.047

Fig. 38 The feature importance of process conditions on microstructure features.

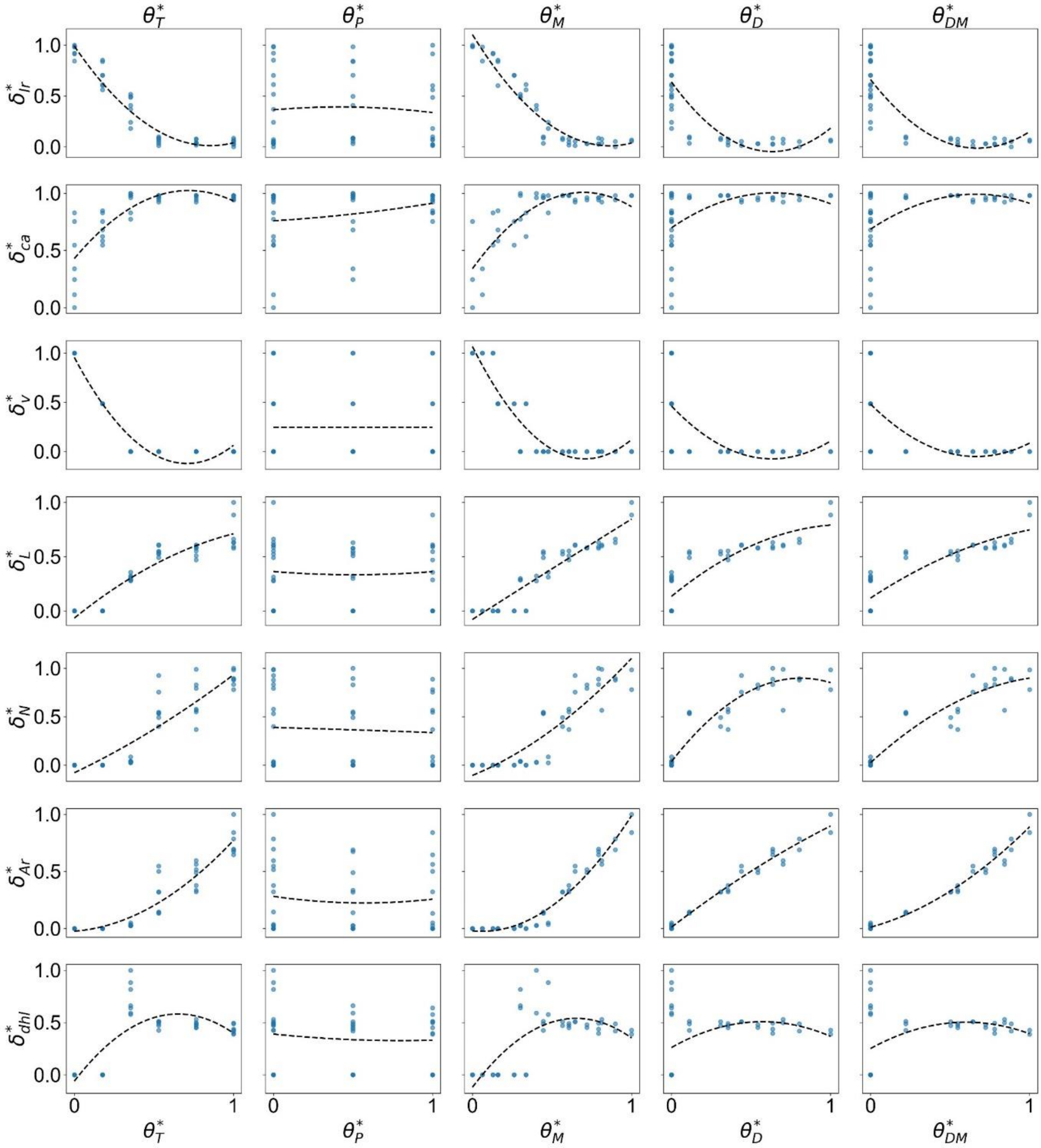

Fig. 39 The response trends of key microstructure features to process conditions.

5.4.2 Microstructure features and joining strength

To investigate the influence of microstructural characteristics on the mechanical performance of the joined joints, a GBDT regression model was established to predict σ_r^*

using the microstructural features obtained in the preceding stage. Fig. 40(a) demonstrates the comparison graph between the original data (horizontal coordinate) and the predicted values (vertical coordinate). It is evident that the predicted and true values are basically distributed near the diagonal line. The R^2, MSE and MAE values of the training and test sets were calculated to further evaluate the generalization performance of the model, and the results are shown in Fig. 40(b)-(d), respectively. The R^2 values of the model are higher than 0.90 on both the training and test sets, indicating that the predicted values are in good agreement with the true values. The model can capture the relationship between microstructure features and joining strength accurately. In terms of error assessment, the training set and test set in have small error differences, with the maximum difference of about 5×10^{-6} for MSE and 5×10^{-4} for MAE. The percentage of MSE and MAE relative to the joining strength index is statistically analyzed, and the percentage of MSE in all data is less than 0.1%, while the percentage of MAE in all data is less than 6%. The relative error ratios are in the acceptable range, showing the high reliability of the model in predicting the joining strength.

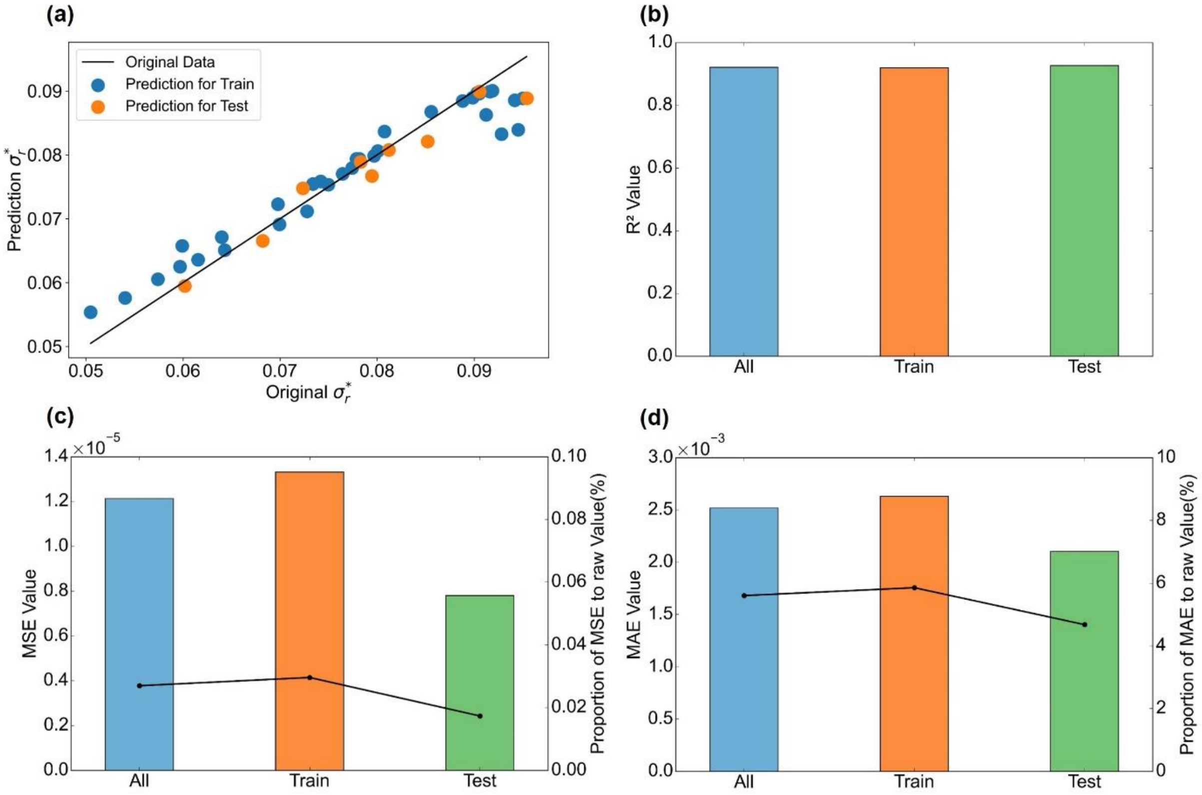

Fig. 40 (a) Predictive results of $\boldsymbol{\sigma_r}$ and Analysis of model generalization ability by (b) coefficient of determination-R², (c) mean squared error-MSE and (d) mean absolute error-MAE.

The relative importance of microstructural features in determining joining strength was evaluated through feature importance analysis of the GBDT model, as illustrated in Fig. 41. Among the positive factors, δ_{Ir}^* and δ_{ca}^* have the most significant influence on the joining strength. This suggests that the adequacy of chemical reaction and the size of the effective bonding area at the interface are the key factors to enhance the strength of the joints during the bonding between Al and CF/PA6. Among the negative factors, the δ_{Ar}^* had the most significant negative effect on the joining strength, followed by the δ_N^* and δ_L^*. This result indicates that the increased size and counts of defects significantly weakened the joining strength, especially in tensile shear experiments, where joint fracture usually depended on the expansion path of cracks. The larger size or counts of defects can accelerate the fracture failure. The effect of defect layer thickness on the joining strength was relatively small, probably because the increase in layer thickness did not significantly change the crack propagation path in the direction perpendicular to the crack direction. These findings highlight the competing roles of interfacial activation and defect formation in determining joint performance. Strength optimization thus requires a trade-off strategy: promoting sufficient interfacial chemistry while simultaneously minimizing thermally induced defects.

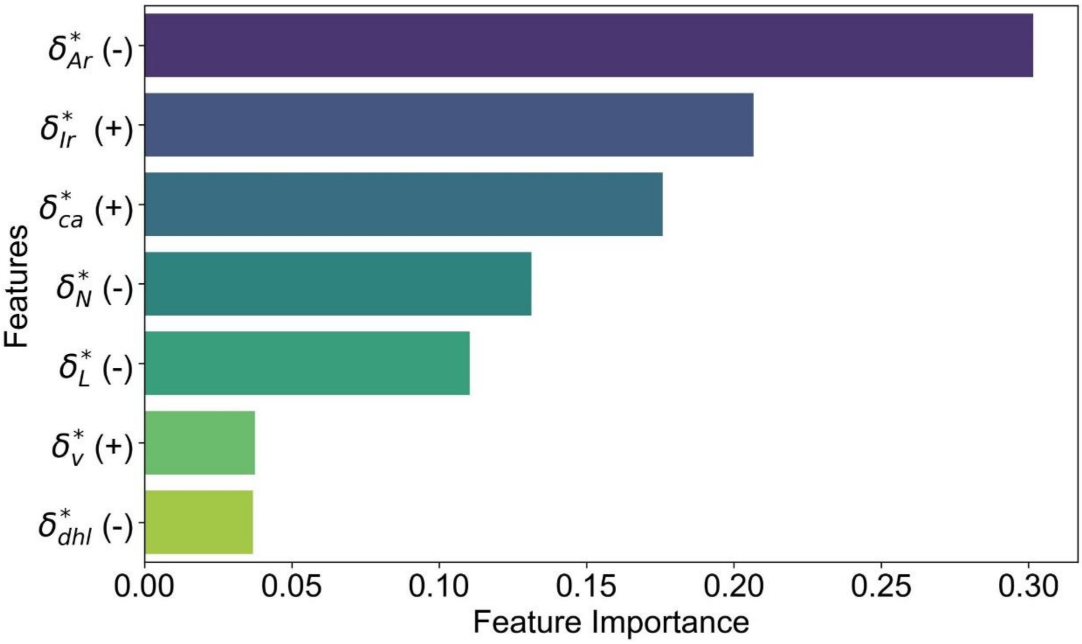

Fig. 41 The feature importance of microstructure features on joining strength.

5.4.3 Process conditions and joining strength

The relationship between process conditions and joining strength was also predicted and analyzed using the GBDT model. The model prediction performance and generalization ability are shown in Fig. 42(a). The uniform distribution of predicted values around the diagonal indicates that the model has high accuracy on both the training and test sets. Fig. 42(b)-(d) compares the R^2, MSE, and MAE values of the model on all types of datasets. The R^2 values are close to 1 on all three datasets. The MSE differences between the training and test sets are below 6×10^{-6} and account for less than 0.08% of the original data values. The differences in the MAE values are all no more than 2.0×10^{-3} and account for less than 4% of the original data values. These results indicate that the model yields stable and reliable predictions. The feature importance analysis in Fig. 43 reveals that θ_M^* is the most influential process parameter in determining joining strength. This finding is consistent with previous analyses, as prolonged residence time above the melting point improves the wettability of PA6 and facilitates interfacial diffusion. Longer residence time reduce the contact angle of polymer resins at the interface, thereby enhancing molecular-level contact between PA6 and the Silanized Al surface [51,52]. The θ_T^* also plays a central role in governing joining strength, not merely by reducing the viscosity of the PA6 resin but more critically by acting as a thermal threshold that governs interfacial chemical activity [53]. Notably, both most influential microstructural features of joining strength, namely effective contact area (δ_{ca}^*) and interfacial chemical bonding (δ_{Ir}^*), are themselves strongly driven by θ_T^*. This dual functionality—promoting both flow and reaction completeness—makes temperature a decisive factor in strength enhancement. However, this enhancement effect is not unbounded. Excessive θ_T^* may lead to thermal degradation of the PA6 matrix, particularly when temperatures exceed approximately 340–350 °C, where decomposition initiates, and accelerates rapidly beyond 400 °C [55]. This degradation results in the formation of interfacial voids and defect layers, which compromise the strength of the joint. Therefore, while θ_T^* is essential for promoting chemical bonding, its value must be carefully controlled to avoid triggering resin decomposition, which would offset the gains from improved interfacial bonding.

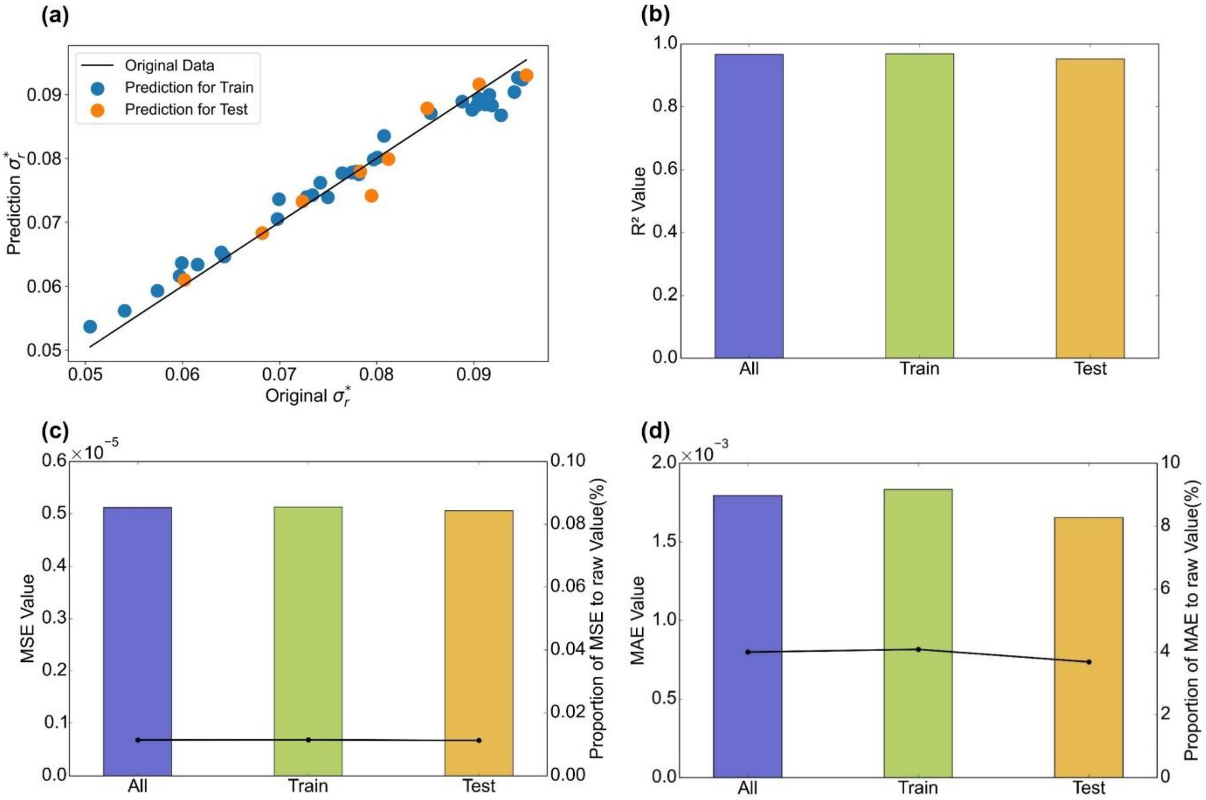

Fig. 42 (a) Predictive results of $\boldsymbol{\sigma_r^*}$ and Analysis of model generalization ability by (b) coefficient of determination-R², (c) mean squared error-MSE and (d) mean absolute error-MAE.

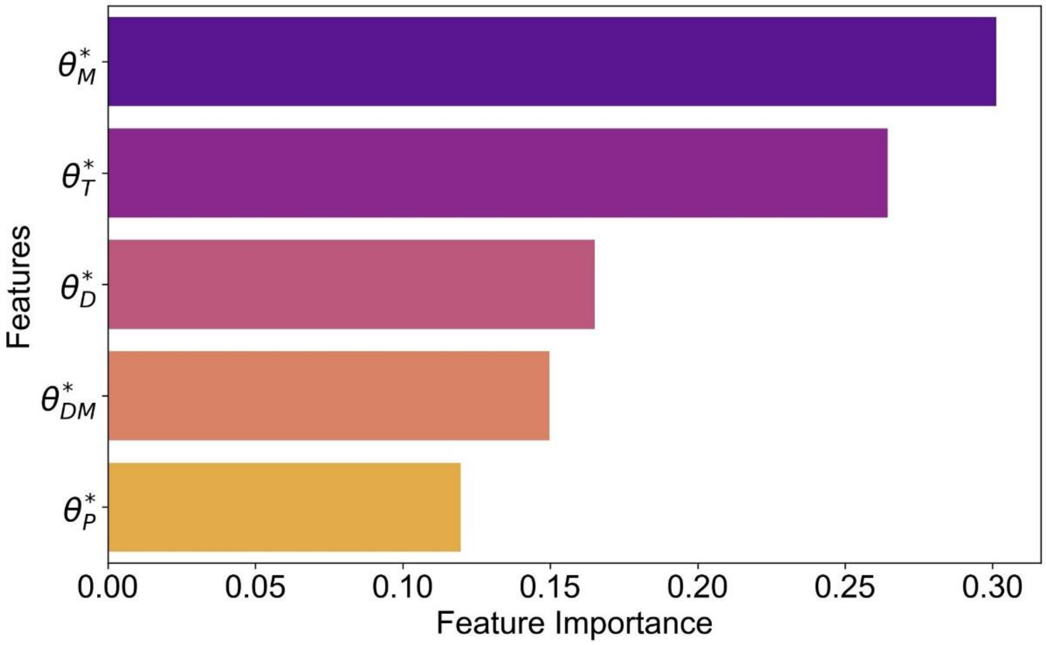

Fig. 43 The feature importance of process conditions on joining strength.

Based on the importance of the causal link between process conditions, microstructure features and joining strength as described above, an integrated Sankey diagram was constructed, as shown in Fig. 44. The diagram effectively integrates the effect of each process parameter ($\theta_T^*,\ \theta_M^*,\ \theta_D^*,\ \theta_{DM}^*,\ \theta_P^*$) on the microstructural features ($\delta_{Ir}^*,\ \delta_{ca}^*,\ \delta_v^*,\ \delta_L^*,\ \delta_N^*,\ \delta_{Ar}^*,\ \delta_{dhl}^*$) and the relationship between these microstructural features further contributing to the joining strength (σ_r^*). The flow lines from left to right indicate causality, and the thickness of each line represents the level of importance. The width of the first-column nodes (process conditions) reflects the total magnitude of influence each parameter exerts on the microstructural features, while the width of the second-column nodes (microstructural features) reflects their cumulative contribution to the final joining strength (σ_r^*). The microscopic features are divided into two categories: positive features ($\delta_{Ir}^*,\ \delta_{ca}^*,\ \delta_v^*$) labeled in green and negative features ($\delta_L^*,\ \delta_N^*,\ \delta_{Ar}^*,\ \delta_{dhl}^*$) labeled in red. As shown in the diagram, θ_T^* and θ_M^* exhibit substantial influences on both positive and negative microstructure features. A quantitative comparison of their total flow contributions reveals that θ_T^* primarily enhances positive features, with 59% of its total flow directed to δ_{Ir}^*, δ_{ca}^*, and δ_v^*, whereas θ_M^* distributes almost equally between positive (47%) and negative (53%) features. In contrast, θ_D^* and θ_{DM}^* predominantly affect negative microstructural features, with over 85% of their total influence contributing to δ_L^*, δ_N^*, δ_{Ar}^*, and δ_{dhl}^*. This analysis suggests that while θ_T^* favors beneficial microstructural evolution, other parameters like θ_D^* and θ_{DM}^* may require tighter control to mitigate negative effects on joining strength. Among the effects of microscopic features on the joining strength, the positive contributions of δ_{Ir}^* and δ_{ca}^* are particularly prominent, together with δ_v^*, accounting for approximately 42% of the total microstructure-derived influence on σ_r^*. In contrast, the negative features δ_L^*, δ_N^*, δ_{Ar}^*, and δ_{dhl}^* collectively contribute around 58%, with δ_{Ar}^* showing the strongest detrimental effect. This suggests that under the current processing conditions, the microstructural evolution imposes a more significant weakening influence on joining strength than a strengthening one. The visualization reveals the mapping relationship between process parameters and microstructure features, and clearly reflects the dual effect of process conditions on joining strength, providing guidance for futural process optimization and microstructure control.

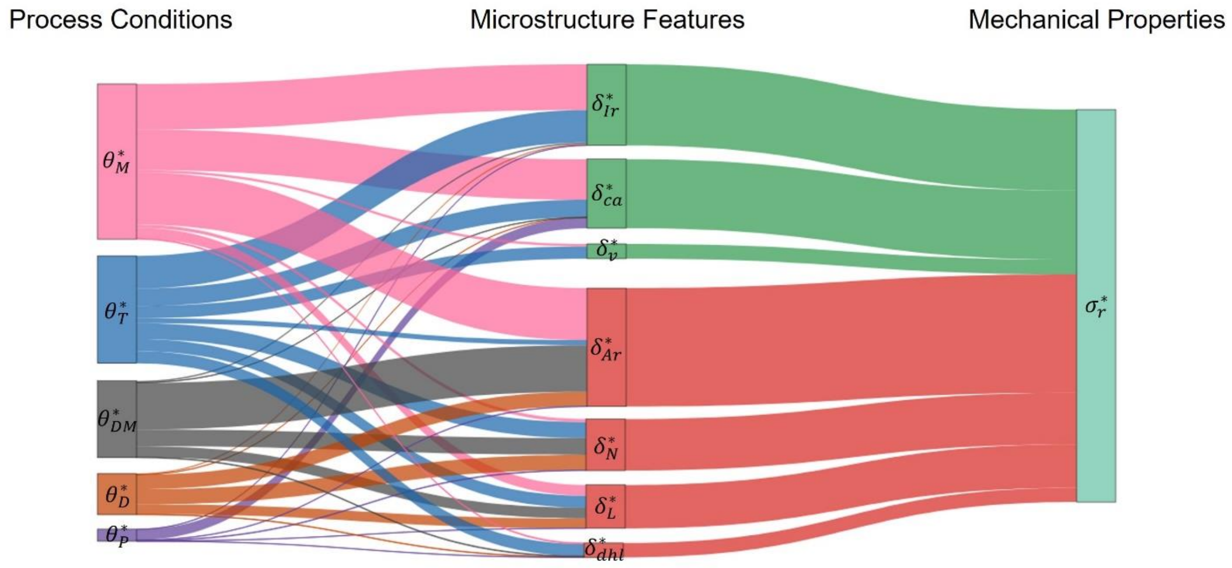

Fig. 44 The Sankey diagram of process conditions, microstructure features and joining strength.

5.5 Model Distillation

5.5.1 Distillation results and discussion

Interpretability directly affects the application value of the model, so we extract expressions with clear physical meaning and sufficient interpretability through model distillation. This not only helps to reveal the physical mechanism of the process parameters on the joining strength, but also makes the model more practicable and reliable in engineering applications by simplifying the model structure. In the process of model distillation, the rational selection of input variables is an important part of improving the model interpretability. Using highly correlated features directly for modeling may lead to multicollinearity, which in turn reduces the stability and predictive performance of the model. Therefore, the input variables were firstly analyzed for correlation, to identify possible alternative relationships. The correlation thermograms between the input variables are shown in Fig. 45(a). θ_T^* shows high positive correlation with θ_M^*, θ_D^*, and

θ_{DM}^{*} with correlation coefficients of 0.961, 0.898, and 0.918, respectively. This suggests that higher temperatures tend to be accompanied by a longer resin flow time and increased thermal diffusion. However, θ_{T}^{*} is almost uncorrelated with θ_{P}^{*}, and the correlation coefficient is close to zero, indicating that temperature and pressure are relatively independent process conditions. The linear regression results of θ_{T}^{*} on θ_{M}^{*}, θ_{D}^{*}, and θ_{DM}^{*} were further analyzed as shown in Fig. 45(b)-(d). This indicates to some extent that θ_{M}^{*}, θ_{D}^{*}, and θ_{DM}^{*} are somewhat substitutable when θ_{T}^{*} is included in the input features. Therefore, only two independent variables, temperature (θ_{T}^{*}) and pressure (θ_{P}^{*}), were ultimately retained in the model distillation to reduce model complexity and avoid the effects of multicollinearity. This choice also reflects the actual configuration of the experimental and simulation setups. Specifically, θ_{T}^{*} corresponds to the pre-set upper limit of the heating stage in the hot-pressing process, and its validity has been verified by numerical simulations to represent the peak temperature reached at the Al–CF/PA6 interface. The pressure θ_{P}^{*} directly corresponds to the applied load P_j in the experimental system, as shown in Table 6. In contrast, θ_{M}^{*}, θ_{D}^{*}, and θ_{DM}^{*} are time-based dimensionless variables calculated from temperature history data obtained at the joint interface in simulations. These variables capture the actual melt residence and degradation exposure periods experienced by the interface under different thermal profiles. Their strong correlation with θ_{T}^{*} reflects the fact that higher temperatures tend to induce longer residence and degradation times.

Notably, the inclusion of elevated temperatures—exceeding the decomposition point of PA6 resin—in the experimental design serves two purposes. First, it enables the exploration of critical defect-generation phenomena under extreme thermal conditions, which lays the foundation for the future studies of thermal–mechanical joining process. Second, as supported by the regression trends in this study, the combination of higher temperatures with shorter heating durations reveals a potential optimization path for achieving sufficient interfacial bonding while suppressing thermal degradation. Although the current heating time are on the order of 1–3 seconds, which may limit the sensitivity of melting residence time and decomposition residence time, future investigations at finer time resolutions could help distinguish more accurately the influence of short-time heating on melt behavior and reaction onset.

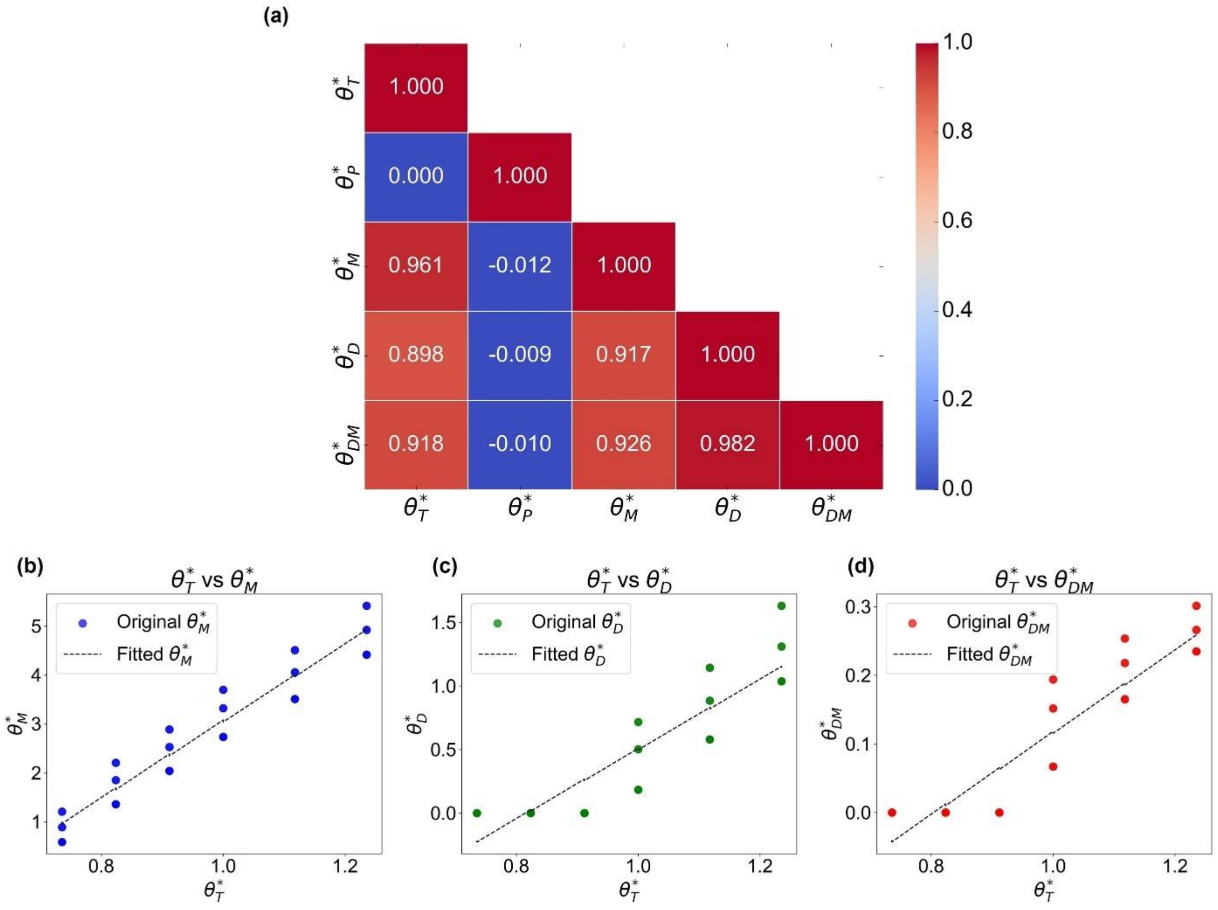

Fig. 45 The (a) correlation of process conditions and linear regression results of $\boldsymbol{\theta_T^*}$ on (b) $\boldsymbol{\theta_M^*}$, (c) $\boldsymbol{\theta_D^*}$, and (d) $\boldsymbol{\theta_{DM}^*}$.

The decomposition behavior of PA6 resin under thermal conditions leads to significant nonlinear variation in the joining strength (σ_r^*) across different temperature intervals. Specifically, the mechanical performance initially improves with increasing temperature and pressure due to enhanced resin flowability and interfacial activation but begins to decline beyond a critical thermal threshold because of resin degradation and defect formation. This convex response—characterized by an initial growth followed by decay—suggests the need for a nonlinear modeling approach capable of describing both enhancement and attenuation phenomena within a unified framework. To mathematically describe the nonlinear change of the joining strength (σ_r^*) with the dimensionless peak temperature (θ_T^*) and pressure (θ_P^*), authors (Ma, Li and Geng) developed an equation (28) using exponential and power functions referring Sato's work for welding deformation [56], which is hereafter referred as the *MLG model*:

$$\sigma_r^* = A \cdot (\theta_P^* + B)^m \cdot (\theta_T^*)^n \cdot e^{-C \cdot \theta_T^*} \tag{22}$$

where A is a strength amplification coefficient, B is a pressure offset term that ensures numerical stability under low-pressure conditions, m and n are the exponents for pressure and temperature influence respectively, and C is the exponential decay coefficient reflecting the degradation tendency at elevated temperatures. The combination of polynomial and exponential terms allows the model to describe the convex-up behavior observed in the experimental data: strength first increases with temperature, reaches a peak, and then declines due to thermal decomposition effects. Model distillation was conducted using nonlinear least squares optimization, with the Trust Region Reflective algorithm selected for its strong robustness under boundary-constrained multivariate conditions. Initial parameter values and bounds were heuristically selected based on the observed data trends to improve convergence efficiency. The model structure and parameter interface were decoupled through a wrapper function to allow flexible expression fitting within the SciPy optimization framework. The final fitted coefficients are shown in Table 8. The high positive value of n emphasizes the dominance of temperature in strength evolution at moderate levels, while the C term ensures strength attenuation beyond the peak temperature. These coefficients provide a compact, yet accurate representation of the underlying thermomechanical mechanisms observed in the joining process.

Table 8 Parameters obtained in model distillation.

Parameters	A	B	C	m	n
Values	318.29	0.00855	7.646	0.1446	6.7646

The updated comparison between the distilled model and experimental results is shown in Fig. 46, where the background contour map in (a) represents the predicted joining strength (σ_r^*) from the distilled analytical model as a function of dimensionless input conditions (θ_T^* and θ_P^*). The color contours indicate the predicted σ_r^* values derived from the MLG model, while the superimposed circular markers represent experimental measurements. Both are rendered using a consistent colormap scale to enable direct visual comparison. The alignment of marker colors with the contour gradients indicates a high level of consistency between the predicted and measured results. Notably, the model accurately captures the peak σ_r^* values near the optimal thermal region ($\theta_T^* \approx 0.82$) and successfully reproduces the decreasing trend of joining strength under excessive thermal exposure. Two-dimensional cross-sectional plots comparing the predictions of the MLG model with experimental data at selected dimensionless pressure levels (θ_P^*) are shown in Fig. 46(b). The dashed lines represent the predicted σ_r^* values, while the circular markers indicate corresponding experimental measurements. Each curve corresponds to a fixed θ_P^* value, allowing detailed evaluation of the model's local fitting performance across the θ_T^* axis. This visualization enables precise, case-by-case inspection of the model's predictive accuracy and supplements the broader trend captured in the 3D contour plot in Fig. 46(a). Despite the simplification of inputs and functional form, the distilled model not only maintains interpretability but also accurately reflects the distribution hierarchy of σ_r^* values under different process conditions. This demonstrates that the simplified formulation retains essential physical insights while ensuring sufficient predictive capability for practical use. However, compared to the results of the GBDT model from chapter 3.1.3, there is a certain degree of degradation in the prediction accuracy of the formulas. The coefficient of determination (R^2) of the distillation model is 0.746, which is slightly lower compared to the GBDT model, as can be seen in Fig. 46 (c), (d) and (e). Meanwhile, the mean square error (MSE) and mean absolute error (MAE) increased to 3.9×10^{-5} and 5.1×10^{-3}, respectively. This discrepancy mainly comes from the reasonable simplification of input parameters and the introduction of polynomial and exponential terms, which inevitably leads to some loss of information. As a result, the distilled model cannot fully capture the complexity of the multivariate nonlinear interactions present in the GBDT model. Nevertheless, the more physically interpretable structure of the distilled model remains valuable for engineering applications. In contrast to purely data-driven models such as GBDT or neural networks, the distilled expression offers a closed-form mathematical formulation that explicitly reflects the thermomechanical interactions during the joining process. This symbolic regression–like structure not only enables intuitive understanding of parameter influence, but also facilitates downstream tasks such as model simplification, boundary extrapolation, and physical insight extraction. The distilled model thus serves not only as a tool for practical process parameter selection but also as a theoretical framework for elucidating the mechanisms underlying joining strength evolution.

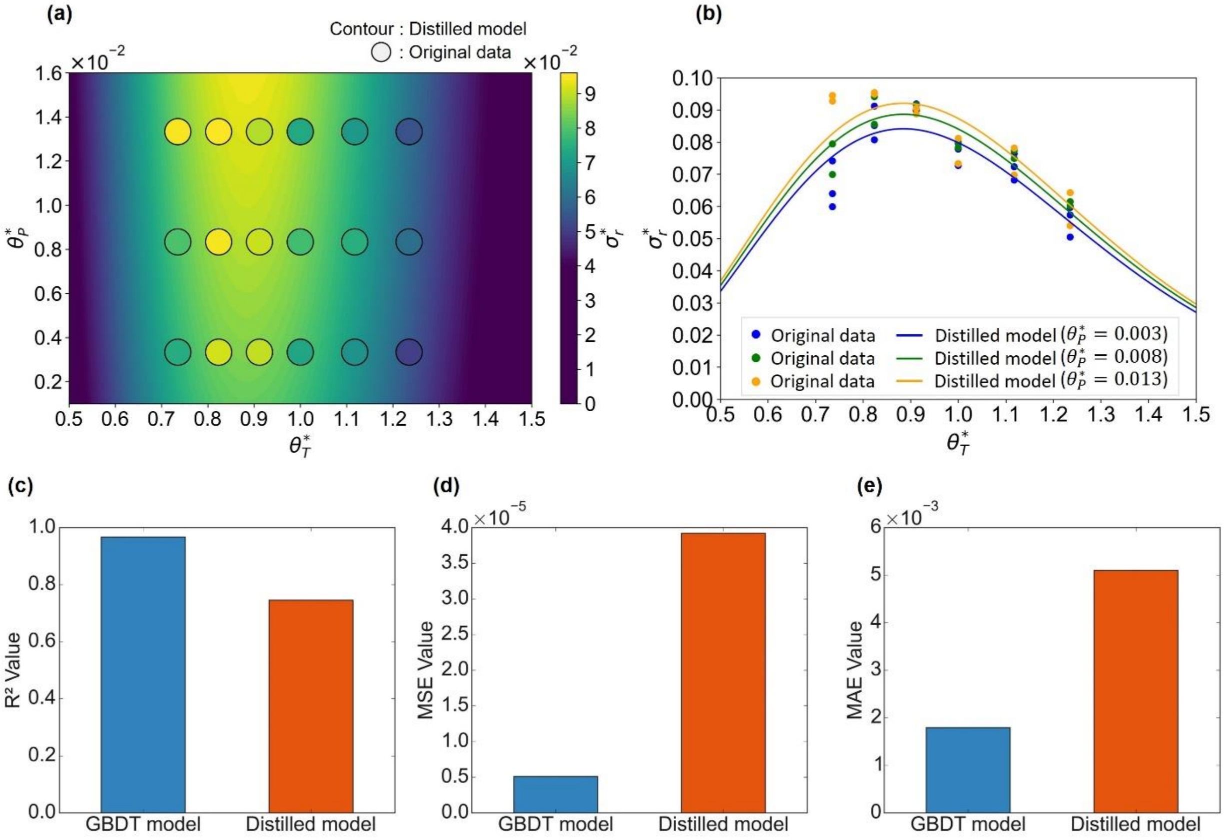

Fig. 46 The (a) contour and (b) 2D-plots comparison of distilled model and original data, as well as the comparison with GBDT model in terms of predictive ability (b) R^2, (c) MSE and (d) MAE.

5.5.2 Future research perspectives on interpretable functional relationships

To further assess the practical applicability and generalizability of the developed interpretable data-driven models, future work is proposed to extend the current modeling framework toward more realistic and heterogeneous joint configurations. In real-world engineering applications, the interfacial thermal–mechanical histories are rarely uniform across the entire joining interface due to local heating variations, tool–substrate contact fluctuations, or geometric complexity. Therefore, verifying the robustness of the proposed predictive model under spatially varied process inputs is of critical importance. As illustrated in Fig. 47, two types of multi-zonal hybrid joints are designed, in which two distinct joining conditions are intentionally applied within a single overlapped area between Al alloy and CFRTP sheets. The different partitions were then designed to be parallel and perpendicular to the lengthwise direction, respectively. This design creates a composite interface with spatially varying thermal–mechanical histories and resulting microstructural features, thereby mimicking more realistic industrial conditions. After fabrication, the mechanical properties of such multi-zonal joints will be evaluated via single-lap shear tests, where the measured joint strength reflects the integrated performance over regions with different bonding qualities.

The previously trained GBDT and distilled models will be employed to predict the shear strength of each zonal region based on the known input parameters (e.g., pressure, peak temperature, residence time), followed by model-based strength integration to estimate the overall joint strength. A comparison between predicted and experimentally measured strength will serve as a rigorous test for the generalization capability of the proposed models beyond uniformly bonded joints. This prospective validation framework provides not only a practical route for extending model applicability but also a systematic methodology for evaluating spatially coupled effects in heterogeneous joints. The results will contribute to closing the gap between controlled experimental studies and real-life manufacturing scenarios, thus promoting the industrial deployment of interpretable, data-driven decision-making tools for hybrid joining process optimization.

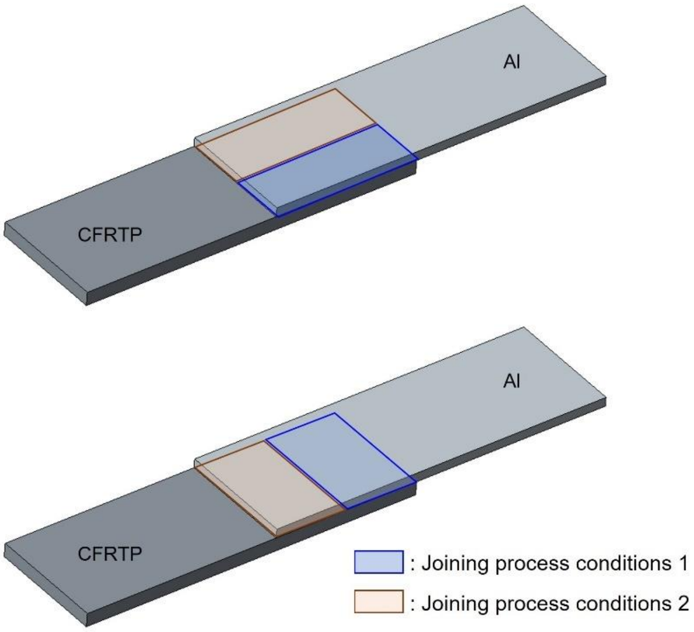

Fig. 47 Schematic of validation under complex joint configuration with multiple partitions.

5.6 Summary

This study establishes a comprehensive data-driven framework to investigate the quantitative relationship between process conditions, microstructure features and joining strength in the hot-pressing joining of Al and CFRTP. By employing dimensionless, machine learning models and model distillation techniques, we reveal the complex coupling mechanisms of different features. The key findings of this study can be summarized as follows:

(1) A dimensionless feature based GBDT model was successfully constructed, integrating process conditions, interfacial microstructural characteristics, and joining strength. This

model enables a comprehensive understanding of the causal relationships among multi-scale variables in the joining process.

(2) Feature importance analysis revealed that the melting residence ratio (θ_M^*) and maximum heating temperature (θ_T^*) are the dominant process parameters influencing microstructure evolution. Among the microstructural features, interfacial chemical bonding intensity (δ_{Ir}^*) and effective contact area (δ_{ca}^*) serve as positive contributors to strength, while defect area (δ_{Ar}^*) and defect density (δ_N^*) exhibit strong negative correlations.

(3) A model distillation approach was used to distill a simplified analytical model from the GBDT output. The derived closed-form expression retains physical interpretability and successfully captures the peak and decline trends of joining strength under varying process conditions.

(4) The final model provides both predictive accuracy and mechanistic insight, supporting the optimization of hot-press parameters to maximize bonding quality while minimizing defect formation. This approach offers a generalizable methodology for data-driven analysis of thermal joining systems.

6. Friction Spot Joining of Al/CFRTP: Tool Geometry and Thermal Behavior

The previous chapters have systematically established a physically interpretable framework for understanding and predicting the bonding mechanisms of dissimilar material joints between silanized Al alloys and CF/PA6. By using hot-press joining as a thermally and mechanically stable research platform, Chapters 3 through 5 have elucidated the individual and coupled effects of joining temperature, dwell time, and interfacial pressure on chemical reaction activation, resin flow, and defect formation. Through a combination of cross-sectional characterization, surface chemistry analysis, and thermal modeling, the relationship between process parameters and interfacial microstructure was clarified. Furthermore, a multi-domain data-driven modeling approach was developed to quantitatively connect process variables to microstructural features and ultimately to joint strength, enabling predictive and interpretable control of joint performance under idealized thermal–mechanical environments. However, in realistic industrial applications, joining processes are rarely as uniform or quasi-static as those employed in laboratory hot-pressing joining. Manufacturing techniques used in mass production often involve rapidly changing, spatially non-uniform, and tool-driven joining methods. These include variations in heating rate, local contact pressure, and material flow behavior, which pose significant challenges to the control and predictability of bonding quality. Therefore, there is a growing need to extend the insights obtained under controlled hot-press conditions to more complex, dynamically driven joining methods that better reflect real-world process environments. To address this gap, the present chapter focuses on friction spot joining (FSpJ), a solid-state joining method that has attracted significant attention for its applicability to lightweight hybrid structures. FSpJ operates by rotating a tool against the surface of a metal sheet (here, Al alloy) overlapped onto a thermoplastic composite (CF/PA6), generating localized heat through friction at the tool–metal interface. As the metal softens under the heat input, pressure is applied to plastically deform the Al downward into the softened polymer, thereby forming a direct, mechanical–chemical joint. This process eliminates the need for external heating, enhances joining speed, and reduces energy consumption, making it suitable for high-throughput automotive and aerospace applications. Despite its advantages, FSpJ introduces complex thermal and mechanical interactions that are fundamentally different from hot-press joining. These include:

Strongly localized heat generation, which leads to sharp thermal gradients and non-uniform interface temperatures.

Transient thermal cycles, which challenge the precise control of polymer melting and degradation behavior.

Tool-dependent contact conditions, especially influenced by shoulder geometry, which affect both heat input and material flow.

Interfacial reactions occurring under dynamic deformation, which differ from the more diffusion-controlled bonding mechanisms observed in static hot-press systems.

Previous studies on FSpJ of Al/CFRTP hybrid structures have highlighted the critical role of tool design—particularly the geometry of the tool shoulder—in determining bonding performance, thermal field evolution, and failure behavior. The shoulder geometry directly governs the contact interface between the rotating tool and the upper metal sheet, thereby controlling the frictional heat generation rate, pressure distribution, and material flow dynamics during the joining process. Compared to traditional friction stir welding where the tool pin plays a dominant role, pinless FSpJ relies almost entirely on the shoulder–substrate interaction, making the shoulder geometry the primary determinant of energy input and deformation behavior. For example, concave shoulders, which introduce a recessed cavity at the tool–metal interface, are known to increase the effective contact area, enhance frictional heating, and promote downward material flow, potentially improving joint formation with deeper plasticized zones. In contrast, flat shoulders apply more localized pressure and generate sharper thermal gradients, which may lead to more defined but thinner bonding regions. These geometric differences can also influence the extent of polymer melting, resin backflow, void formation, and thermal degradation—particularly at elevated tool rotation speeds and joining temperatures. As such, the shape and dimensional parameters of the shoulder significantly affect the local process conditions that determine the quality and reliability of the resulting joint. Despite these observations, the mechanistic understanding of how shoulder geometry modulates interfacial microstructure, chemical bonding, and mechanical response remains incomplete. Existing literature tends to focus on empirical strength comparisons without fully elucidating the intermediate structural transformations or thermal histories involved. Moreover, many studies neglect the synergistic effects between tool-induced pressure and temperature distribution, which are highly interdependent and sensitive to geometric features such as concavity depth, shoulder diameter, and contact contour [57–59]. In addition, comparative studies linking the bonding behavior in FSpJ to that in more controlled processes such as hot-press joining are still lacking. Given that hot-press joining provides a well-defined and spatially uniform thermal–mechanical environment, it offers an ideal reference platform for isolating key bonding phenomena. Investigating whether and how similar mechanisms—such as interfacial chemical activation, resin wetting, and defect suppression—manifest under the more dynamic and tool-sensitive conditions of FSpJ is critical for validating the generalizability of previously derived bonding principles and predictive models. Therefore, a more systematic investigation is required to elucidate how shoulder geometry influences the spatial and temporal evolution of temperature at the metal–polymer interface, and how such thermal patterns, when coupled with pressure-induced deformation, govern resin flow behavior, bonding layer formation, and the emergence of interfacial defects. It is also essential to determine whether these microstructural and thermal effects can be quantitatively correlated with macroscopic joint performance metrics, such as tensile shear strength and fracture mode distribution. Addressing these questions is critical for clarifying the mechanistic role of tool geometry in FSpJ and for evaluating the generalizability of bonding principles and predictive models developed under more controlled hot-press conditions. To address these gaps, the present chapter integrates experimental trials with tools of varied shoulder designs and high-fidelity thermo-mechanical simulations to reveal the process–structure interactions specific to FSpJ. The insights obtained are then discussed in the context of prior findings from hot-press joining, thereby laying the groundwork for cross-process understanding and unified model development. This chapter is organized as follows:

Section 6.1 presents the experimentation and ALE-based thermal–mechanical simulation framework and validation results.

Section 6.2 compares joint appearance and morphologies.

Section 6.3 analyzes joint mechanical performance.

Section 6.4 analyzes Fracture morphology.

Section 6.5 summarizes the heat transfer characteristics.

Section 6.5 compares the correlation between interfacial fracture and temperature distribution.

6.1 Experimentation

6.1.1 Joining condition

The Friction Stir Welding (FSW) machine with PC control was used to perform the FSpJ experiments. The specific stages of FSpJ are illustrated in Fig. 48(a). Main joining conditions such as tool plunge speed, plunge depth and tool material used are shown in Table 9. During the joining process, an overlapping interface of 50 × 50 mm^2 was formed by lapping the upper Al alloy sheet on the CF/PA6 sheet surface. According to previous work[60], a stepped shoulder tool with a single inward recess area was selected for investigation due to its simple structure and ease of fabrication. External shoulder diameters of 12 mm and 15 mm were considered to examine the effectiveness of this tool in improving joint performance. For each diameter tool, 0.2 mm and 0.4 mm recess depth were used in FSpJ experiments. In addition, a 15 mm-diameter flat shoulder tool was used as the reference tool in the experiment analysis. The detailed dimensional information of the friction tools studied is presented in Fig. 48(b), with their features simplified and illustrated. The tools are made up of SKD61 steel, which has high hardness and high wear resistance after heat treatment.

6.1.2 Measurement and characterization

Three-dimensional profilometer device (Keyence VR-5000) was used to evaluate the state of Al alloy distribution within the tool projection plane after joining as well as the morphological appearance of the fracture surfaces between CF/PA6 and Al alloy after tensile shearing test. In this study, joint strength was evaluated by a single lap tensile shear test conducted at a crosshead rate of 1 mm/min using a universal testing machine (SHIMADZU AGSX). Three joint samples at least were prepared for each condition and the maximum tensile shear forces of these samples were averaged as the joint strength. The single lap tensile shear test is shown in Fig. 48(c). Contact thermocouples and non-contact infrared cameras are both commonly used for temperature measurement in welding experiments [61,62]. However, ensuring the accuracy of the measurement results requires parameter calibration of the measurement methods before welding. In this study, an infrared imaging method, calibrated for emissivity in preliminary work [63], was used to accurately capture the temperature distribution on the Al upper surface. In the current study, a thermal infrared camera (CPA-E86S, Chino) was used in FSpJ to obtain temperature distribution data on the upper surface of the Al alloy around the rotating tool as shown in Fig. 48(d). In earlier work, the emissivity of the Al alloy surface was calibrated over the temperature range of 20-600 °C [64].

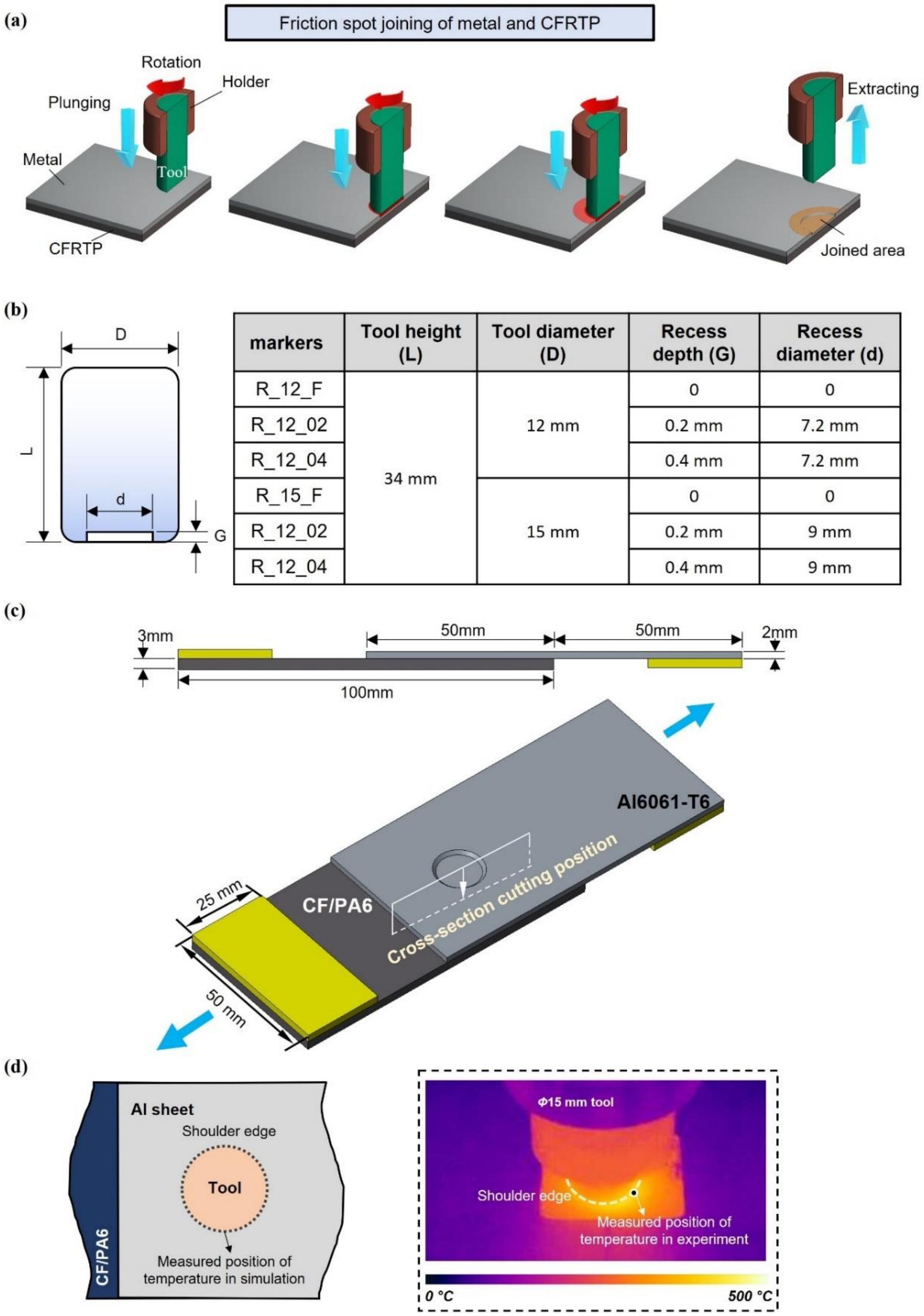

markers	Tool height (L)	Tool diameter (D)	Recess depth (G)	Recess diameter (d)
R_12_F	34 mm	12 mm	0	0
R_12_02			0.2 mm	7.2 mm
R_12_04			0.4 mm	7.2 mm
R_15_F		15 mm	0	0
R_12_02			0.2 mm	9 mm
R_12_04			0.4 mm	9 mm

Fig. 48 Schematic diagrams of (a) pinless-FSpJ process, (b) different shapes and sizes of tools, (c) lap joint showing cutting position of cross-section and lap shear test configuration and the (d) measured positions of temperature.

Table 9 Joining conditions and tool characteristic used in the experiment.

Joining conditions/tool characteristic	Used value
Rotational velocity (rpm)	1500
Plunging depth (mm)	0.3
Plunge speed (mm/s)	0.1
Tool material	SKD61 steel
Density (kg/m^3)	7760
Elastic modulus (GPa)	215
Thermal conductivity(W/mK)	10.4
Specific heat (J/kgK)	460

6.2 Finite element simulation

6.2.1 Basic information

The thermo-mechanical coupling finite element method based on the commercial software Abaqus/Explicit Arbitrary Lagrangian and Eulerian (ALE) formulation was applied to simulate the FSpJ process between the Al alloy and CF/PA6 in this study. The main physical issues including friction heat generation between rotational tool and Al alloy, heat transfer within Al alloy-CF/PA6 joining zone, and localized deformation of the plasticized Al alloy sheet driven by tool are contemplated in the simulation. Moreover, it is assumed that the Al-CF/PA6 interface is in intimate contact with each other, ignoring the effect of macro-scopic gap on contact heat transfer. And the material properties of Al alloy and CF/PA6 workpieces are assumed to be isotropic. Fig. 49 shows the FSpJ finite element model of Al-CF/PA6. To balance computational accuracy and cost, non-uniform meshing method with a minimum element size of ~ 0.1 mm in the lapped zone is used for both Al and CF/PA6 sheets. The lapped zone through the thickness direction was considered as an ALE adaptive mesh domain to prevent the distortion of the element mesh along caused by the sheet deformation. In the simulation, the steel tool is simplified as a rigid body and only the heat transfer is calculated. Eight-node thermo-mechanically coupled elements (C3D8RT) were used for the both sheets.

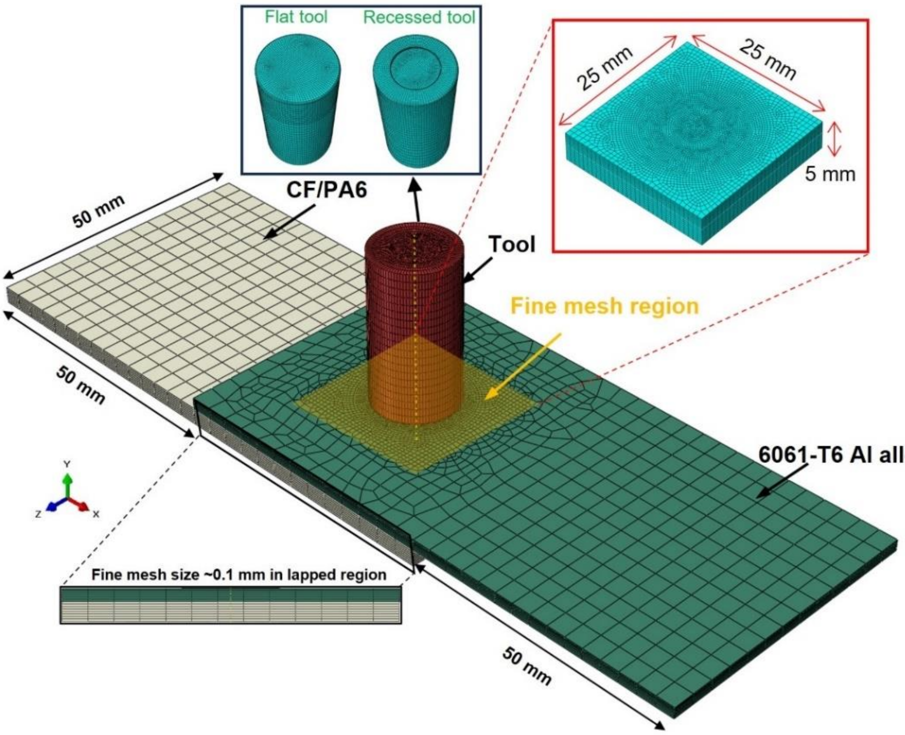

Fig. 49 Finite element model of the friction spot joining of Al alloy and CF/PA6.

6.2.2 Thermal and material models

In the thermo-mechanically coupled model used in this study, the instantaneous temperature distribution is calculated based on the non-Fourier heat conduction law. The heat sources are surface heating (q_f) from friction during the FSpJ process between the tool and the Al alloy workpiece and volumetric heating (q_p) from plastic deformation of the Al plate surface. These two heat source models are represented by the following equations, respectively:

$$q_{\mathrm{f}} = \tau\dot{\gamma} = \mu(T)P_{\mathrm{n}}\dot{\gamma} \tag{23}$$

$$q_{\mathrm{p}} = \eta\sigma\dot{\varepsilon}^{p} \tag{24}$$

In Eq. (23), q_{f} represents the frictional heat generation rate at the Al-tool interface calculated by Coulomb's friction law; μ is the coefficient of friction. P_{n} and $\dot{\gamma}$ are the nodal contact pressure and the sliding rate, respectively. In Eq. (24), q_{p} is denoted as the volumetric heat generation rate due to plastic deformation of the Al sheet. η is the constant of proportionality for the conversion of the energy from plastic deformation to heat with a value equal to 90% of the one used in the present model [65]; σ and $\dot{\varepsilon}^{p}$ are the plastic stress and strain rates, respectively. In the FSpJ process conducted by the pinless tool used in this study, almost no stirring effect between the tool and the Al sheet exists, therefore surface frictional heating dominates the heat input. In this simulation model, the temperature-dependent friction coefficients experimentally obtained by Zhang et al. [66] for 6061-T6 FSW are adopted, with the variation of the friction coefficient with temperature (T) described by the following linear equation:

$$\mu(T) = \mu_0 - KT \tag{25}$$

where μ_0 and K are experimentally obtained constants related to the temperature range. According to Eq. (25), we can obtain the folded lines of the friction coefficient with temperature for the different temperature intervals used in the simulation, as shown in Fig. 50.

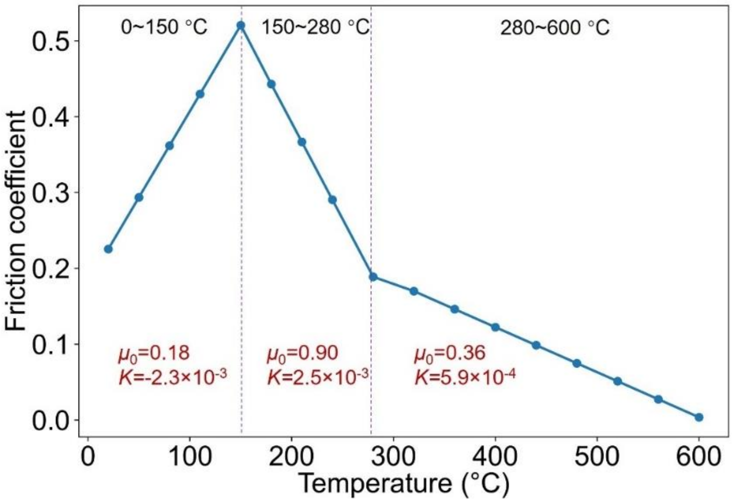

Fig. 50 Friction coefficient used in the model [66].

In the current simulation, the Johnson-Cook model widely used in numerical simulation of solid-state joining was employed to describe the flow stress of 6061-T6 Al alloy, and the correlation between flow stress and deformation conditions is expressed as follows:

$$\sigma_{\mathrm{y}} = \left(A + B\varepsilon_{\mathrm{p}}{}^{n}\right)\left[1 + Cln\left(\frac{\dot{\varepsilon}_{\mathrm{p}}}{\dot{\varepsilon}_{0}}\right)\right]\left[1 - \left(\frac{T - T_{\mathrm{r}}}{T_{\mathrm{m}} - T_{\mathrm{r}}}\right)^{m}\right] \tag{26}$$

where σ_{y}, ε_{p}, and $\dot{\varepsilon}_{\mathrm{p}}$ denote the yield flow stress, equivalent plastic strain, and equivalent plastic strain rate of the material, respectively. $\dot{\varepsilon}_{0}$ is the reference plastic strain rate, and T_{m} and T_{r} are the melting point and ambinent temperature, respectively. The solid-phase temperature is considered to be the melting point of the 6061-T6 alloy, and the values specified for the material constants in Eq. (26) were listed in Table 10. The CF/PA6 was modeled as an isotropic elasto-plastic material, while also accounting for temperature-dependent thermal conductivity, specific heat capacity, and thermal expansion properties, as shown in Fig. 51. The mechanical and thermophysical properties of CF/PA6 were measured by JFE Techno-Research. The Young's modulus and yield strength data for CF/PA6 were determined from the measured stress-strain curves according to BS EN ISO 527-1:1996. Data outside of the measured temperature range was linearly extrapolated from the available data[12].

Table 10 Material constants for Johnson-Cook model for 6061-T6 Al alloy [67].

A (MPa)	B (MPa)	n	C	m	T_M (°C)	T_s (°C)
293.4	121.26	0.23	0.002	1.34	582	20

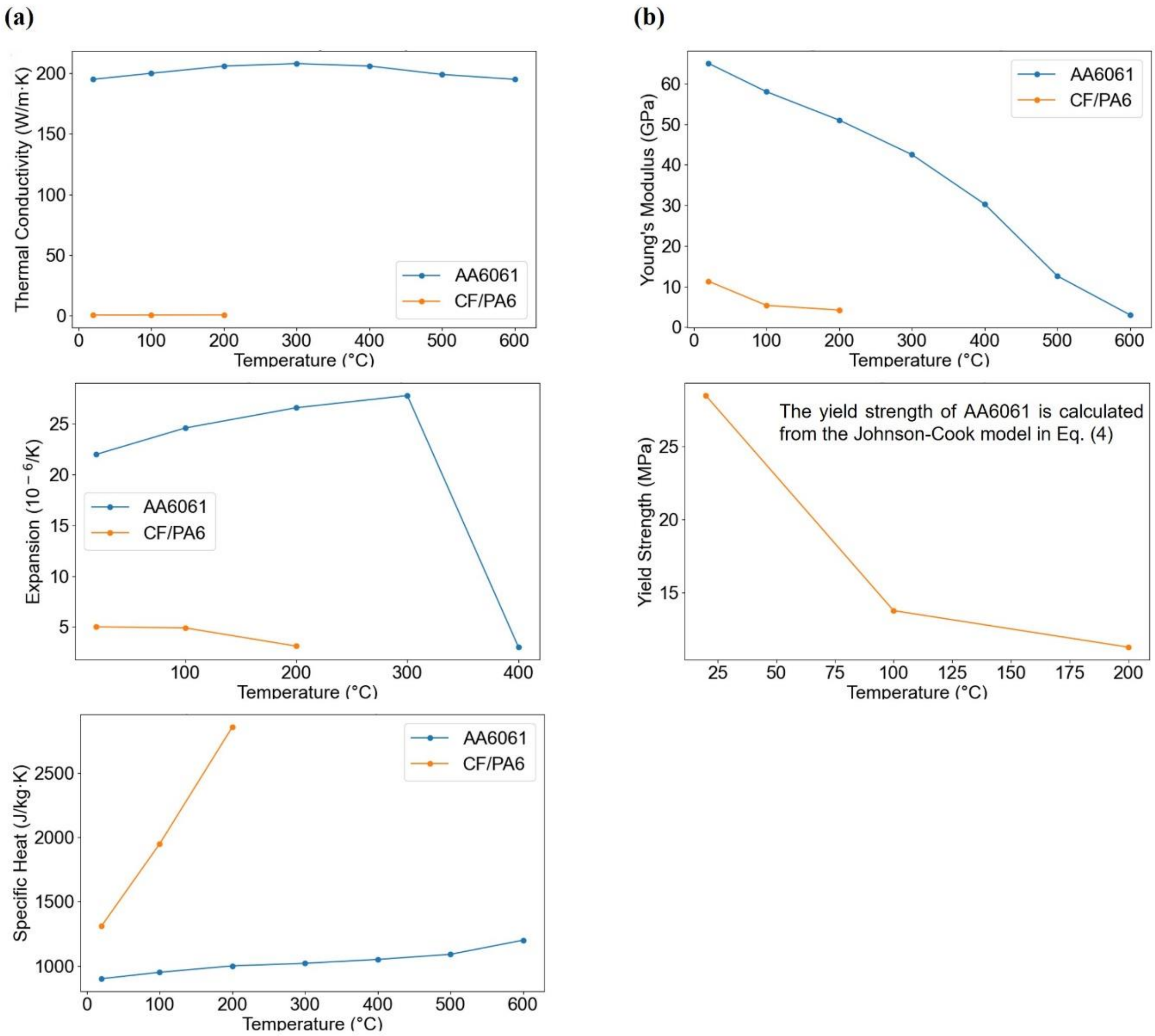

Fig. 51 The (a)thermo-physical and (b)mechanical properties of work-piece materials [12].

6.2.3 Boundary conditions and validation of Finite element simulation

The mechanical and thermal boundary conditions used in the simulation model are shown in Fig. 52. During the joining process, clamps were used to completely fix the workpieces except for the region of the weld at the top of the Al alloy in order to prevent misalignment and movement of the overlapping workpieces., The proportion of the frictional heat generated on tool/Al alloy interface, distributed into Al alloy side, was set at 60% [68] The heat loss is mainly accomplished by heat convection between the weld zone and air environment and contact heat transfer into the the jig at the clamping area, which is simplified to the following equation:

$$q_{\mathrm{c}} = h_{\mathrm{c}}(T - T_{\mathrm{a}}) \tag{27}$$

where h_{c} is the thermal convection coefficient and T_{a} is the temperature of the surrounding environment such as air, jig contact surface, etc., which is set as a constant temperature in this study. As shown in Fig. 52, a constant free convection coefficient of 20 W/m^{2}K was used for the unclamping zone of Al ally top surface, and a superposition heat transfer coefficient of $h_{\mathrm{c}} = h_0(T - T_0)^{0.25}$ was used for the other Al alloy external surfaces[69]. A simplified constant heat convection coefficient of 10 W/m^{2}K was used for the outside surface of CF/PA6 [70]. Additionally, the pressure-dependent heat transfer coefficient $h_{\mathrm{t}} = 391.529 \cdot {P_{\mathrm{n}}}^{0.577}$ was used to represent the heat transfer between the tool and the Al alloy [71]. A penalty function contact algorithm was used to simulate the interaction and contact behavior between the tool and the top surface of the Al alloy. In the overlap interface, a tie constraint was applied to the clamped region, while thermal contact conductance with a critical gap was used for the unclamped lap joint interface region, which more accurately reflected the actual situation of contact heat transfer [72]. For simplification, an average thermal conductivity between the Al alloy and CF/PA6 was used when the gap clearance was less than 0.01 mm.

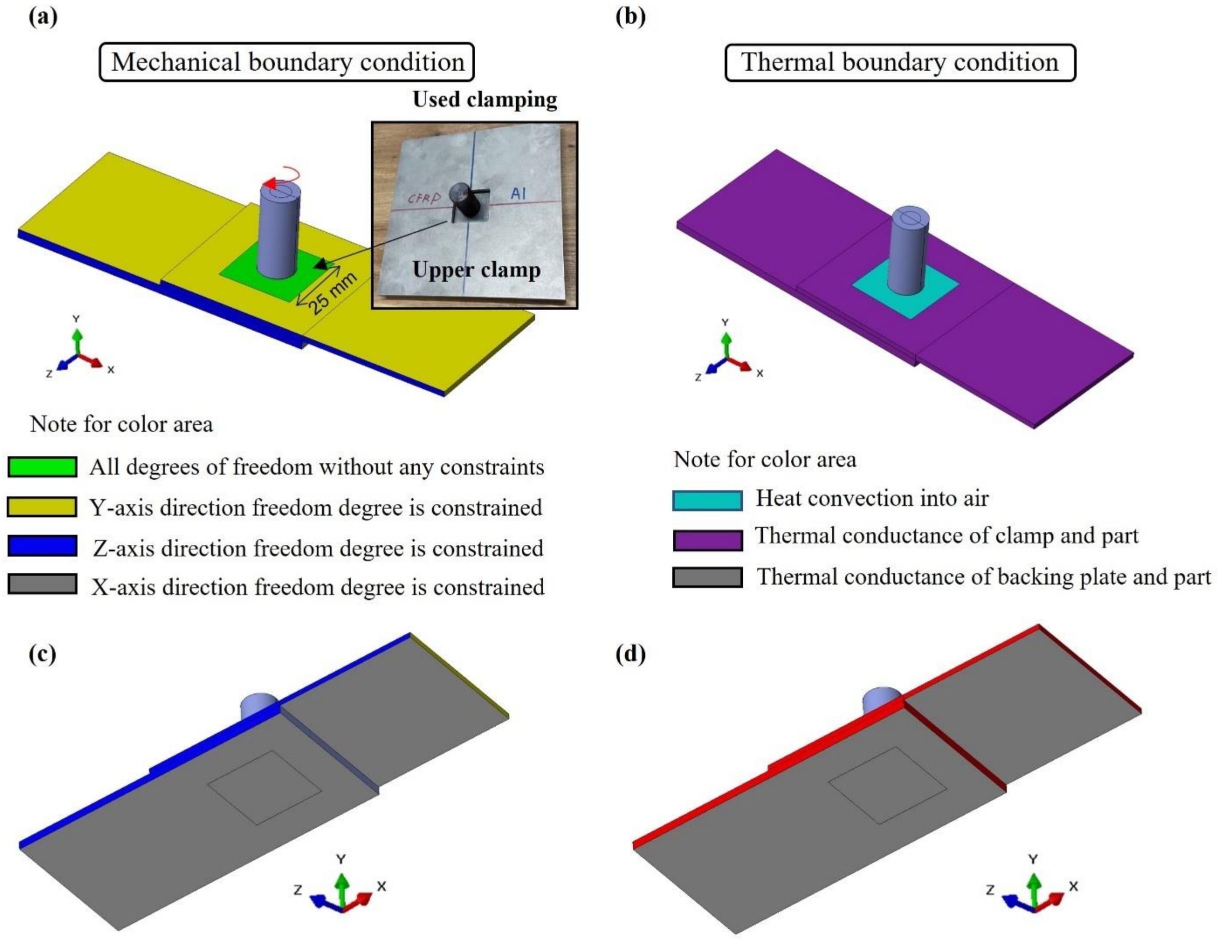

Fig. 52 Thermo-physical and mechanical properties of (a) CF/PA6 and (b) AA6061 workpiece materials. And schematic illustration of (c) mechanical and (d) thermal boundary conditions.

The simulated temperature history located on the upper surface of the Al alloy close to the outer edge of the tool was compared with the experimental temperature history recorded by the thermal infrared camera, as shown in Fig. 53. Based on the comparison, the predicted temperature histories and the measured temperature histories for different shapes and sizes of tools showed similar upward and downward trends, which indicated that the heat transfer model used in the experiments is reasonable. However, the Lagrangian formulation used for CF/PA6 in the model did not effectively capture the changes in solid flow dynamics and interactions. Consequently, the volume changes of

PA6 resin, such as melting into a fluid due to heat and shrinking upon solidification, were not accounted for. These limitations will be addressed in our future work.

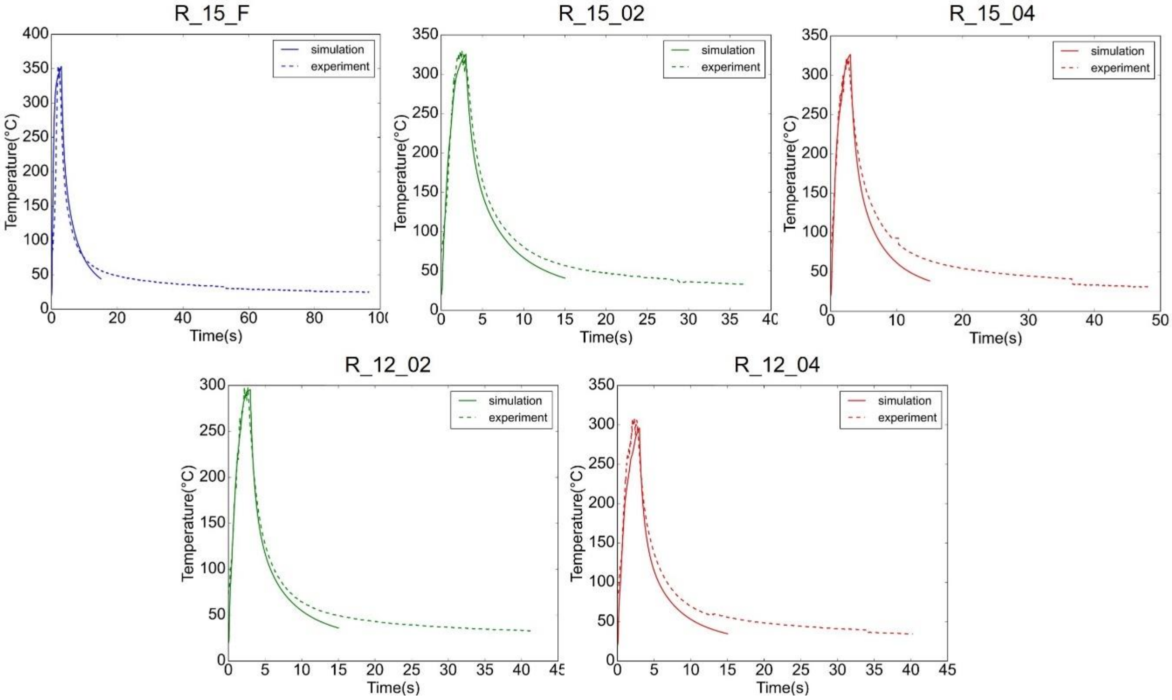
R_15_F

R_15_02

R_15_04

R_12_02

R_12_04

Fig. 53 Comparison of temperature histories between numerical simulation and experimental measurement for different tools.

6.2 Joint appearance and morphologies

Fig. 54 shows cross-sectional images of FSpJ joints fabricated with a 15mm flat tool (R_15_F), a 15mm tool with a 0.2mm recess depth(R_15_02), a 15mm tool with a 0.4mm recess depth(R_15_04), and a 12mm tool with a 0.4mm recess depth(R_12_04), to compare the effects on the joint appearance produced by different depths of recessed zone and outer diameters of tools at the same joining parameters. The Al to CF/PA6 interface was characterized by three distinct zones, namely, the tool-affected zone (TAZ), the resin adhesion zone (RAZ), and the resin outflow zone (ROZ). In the TAZ region, the PA6 resin matrix contacted the Al alloy under the action of the tool plunge. The silanized layer on the Al alloy surface underwent a chemical reaction with the molten resin matrix when heated, and the formation of epoxy groups and amide groups (-CONH-) predominated the chemical bonding [73–75]. The macro and micro mechanical interlockings were also formed with the re-solidification of molten resin matrix adhered on the Al alloy surface. In the RAZ region, even though there was no apparent interface deformation caused by the tool plunge, the resin matrix might still reach melting or decomposition temperatures through heat transfer from the Al alloy, contributing to interfacial strength. However, the molten resin from the TAZ zone flowed outward to the ROZ zone where the temperature of matrix resin of CF/PA6 was below its melting point, offering a weak bonding with the CF/PA6 orginal surface and even a gap existed due to the discontinuous outflowed resin. As shown in Fig. 54(a) and (b), the flat tool produced a maximum RAZ diameter of approximately 29 mm, whereas the RAZ region was narrowed to 27.2 mm with R_15_02 tool. As the depth of the recessed zone rose up to 0.4 mm in Fig. 54(c), the diameter of the RAZ region was further reduced. Furthermore, reducing the tool diameter from 15 mm to 12 mm at the same depth of recessed zone resulted in a decrease in the diameter of RAZ region.

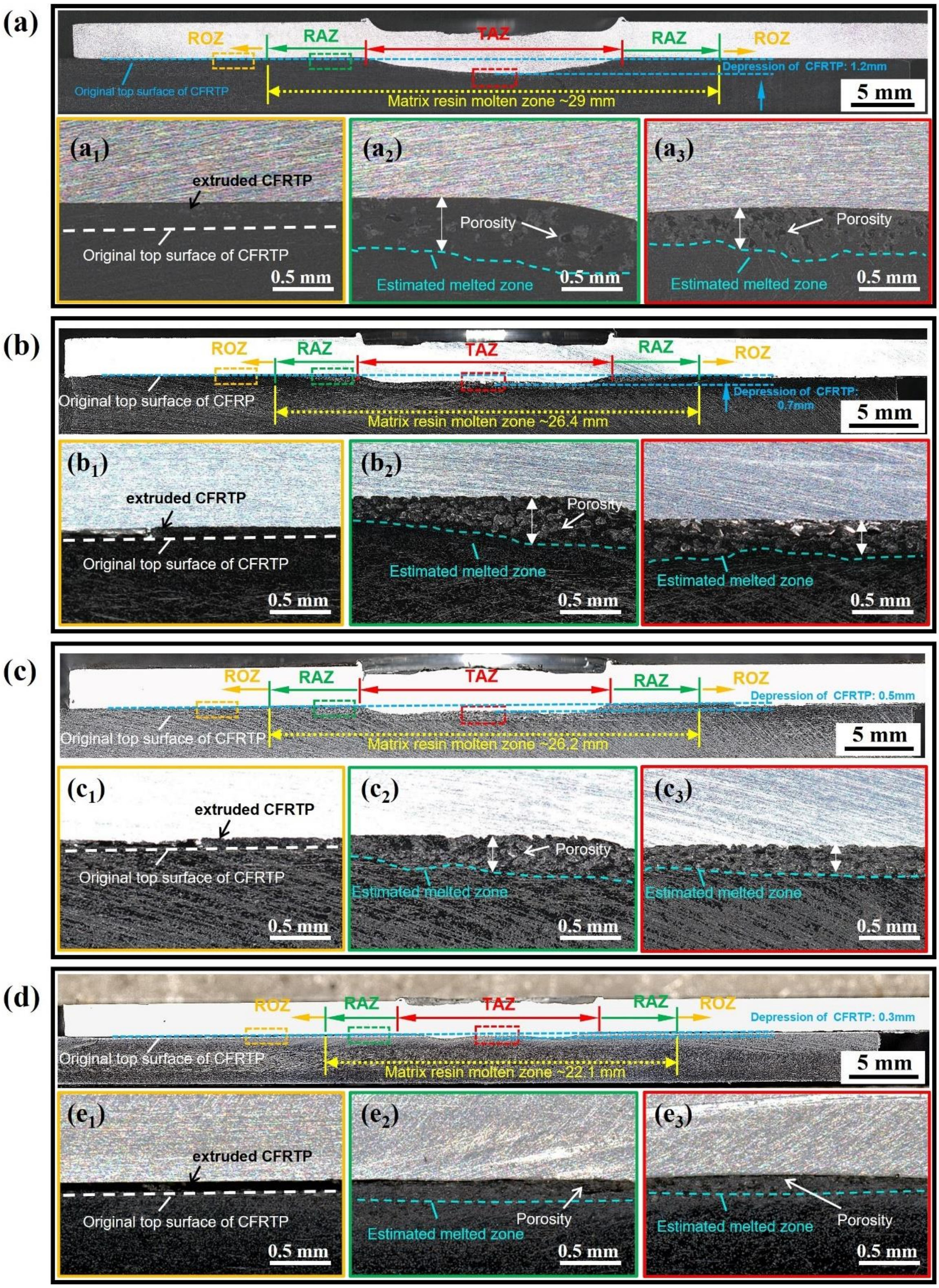

Fig. 54 Cross-sectional view of the FSpJ joint between 6061-T6 alloy and CF/PA6 at 1500 rpm showing the effects of tool modification on the interfacial microstructure. (a)

Flat-shaped Φ15mm tool, (b) 0.2mm recess-shaped Φ15mm tool, (c) 0.4mm recess-shaped Φ15mm tool, (d) 0.4mm recess-shaped Φ12mm tool.

Joining with the flat tool resulted in a significant interface bulge from the Al to the CF/PA6 side on the macroscopic scale shown in Fig. 55(a). This is due to the downward plastic deformation of the Al alloy sheet under the huge compression force exerted by the flat tool. The interfacial bulge reached 1.2 mm compared to the original contact interface. However, welding using a 15 mm-dimater recessed tool with a depth of 0.2 mm effectively mitigated the tendency of the Al alloy sheet to intrude into the CF/PA6. The overall interfacial bulge of the RAZ region was reduced to 0.7 mm (Fig. 54b). As the recess depth was changed to the 0.4 mm, the intrusion depth from the Al alloy deformation futher decreased to 0.5 mm in Fig. 54(c), indicating a deeper recess effectively suppressed the downward plastic deformation of Al alloy and prevent more molten-resin from overflowing from the RAZ region. Besides, some porosities defects caused by the thermal decomposition of molten-state resin existed within the resolidified CF/PA6 region. Compared to the flat tool, the porosities size in the estimated melted zone of CF/PA6 under the recess-shaped tool became smaller, reflecting a reduction in heat generation. As shown in Fig. 54(c), compared with the tool with a recess depth of 0.2 mm, the increase of depth further decreased the thickness of estimated melted zone and the excessive thermal decomposition-induced defects were also somewhat suppressed, which was more pronounced under the smaller diameter tool in Fig. 54(d).

6.3 Joint mechanical performance

Fig. 55 shows the results of tensile shear tests on FSpJ joints using different tools. The calculation of the tensile shear strength of joints is generally related to the joining area and local strength in different regions. Different calculation methods existed in previous publication without a unified standard[76,77]. Here we calculated the average joint strength based on the combined area of the RAZ and TAZ regions, and the individual area of the TAZ region, respectively, under the assumption that the interface characteristic regions are circular. And we compare the maximum tensile shear strength calculated for the TAZ with other previous studies. As seen in Fig. 55(a), increasing the tool diameter increases the maximum tensile shear force regardless of the tool shape because a larger diameter increases the joint area and thus increases the load carrying capacity of the joint. It is worth noting that the maximum tensile shear load or strength of the recessed tool is higher than that of the flat tool, which is due to the fact that using the recessed tool suppresses the density of porosity defects and consequently obtains good mechanical properties, as shown in Fig. 54(b)-(c). In addition, the large error bars in the tensile shear load shown in Fig. 55(a) are likely due to the accumulation of Al alloy on the welding tool during the process, which affects the tool's stability in long-term use. In future research, we will attempt to address this issue by optimizing the welding parameters. When the depth of recess increased from 0.2 mm to 0.4 mm, the density of porosity defects was further reduced, exhibiting an increase in the maximum tensile shear load or strength of the joint. Comparing the cases with the same depth of recess, the average strength of 12 mm and 15 mm diameters was comparable and exceeds 20 MPa when calculated on the basis of the area of the TAZ region, as shown in Fig. 55(b). The maximum average strength of about 28 MPa was obtained at 12 mm at a depth of 0.4 mm. When comparing the results calculated using TAZ+RAZ for a 15mm diameter, the joint strength for the 0.2mm and 0.4mm concave tools is approximately 22% and 34% higher than that of the flat tool, respectively. As shown in Fig. 54(d), the 12 mm tool produced less porosity defects compared to the 15 mm tool. As shown in Fig. 55(c), compared to the similar heat-assisted welding process, the joint strength of current work was slightly lower than the maximum strength value achieved in the Ref. [78]. However, their joint interface exhibited more significant combined-enhancement of macro/micro mechanical interlocking and chemical bonding. It was inferred that, by using optimized friction tools to join silanized Al alloy and CFRTP, there was a strong possibility that further introducing measures to reinforce interfacial mechanical interlocking could achieve even higher interfacial strength. Additionally, the result of joint residual stresses measurements is shown in Fig. 56 in the Supplementary Materials. A tension residual stress state was found at the center of the Al upper surface, showing a decreasing trend with increased recessed tool depth. This suggests that the recessed shoulder tool design has potential for both enhancing joint strength and improving stress conditions.

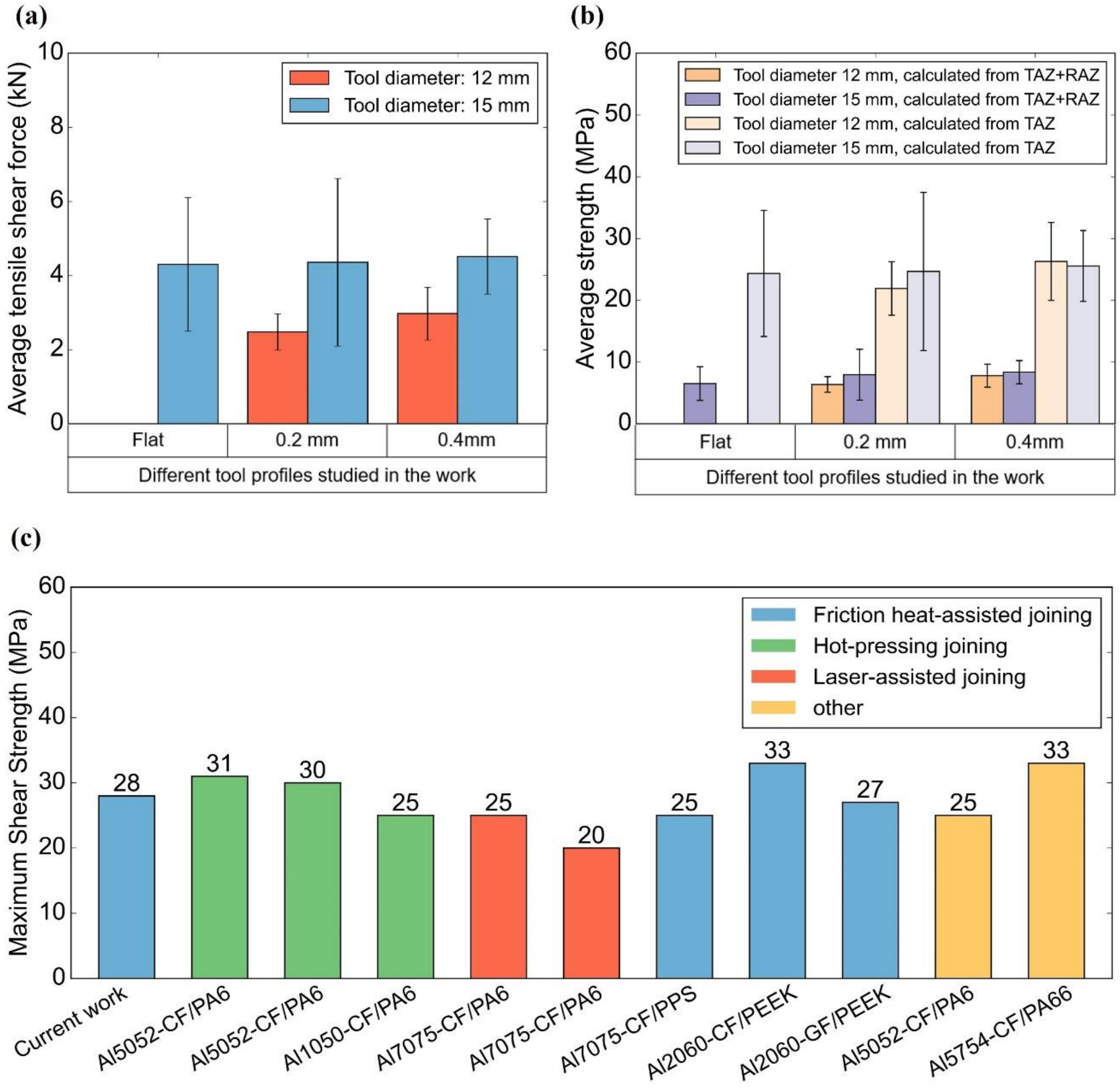

Fig. 55 (a) Tensile shear test result and (b) average strength of AA6061-T6 and CF/PA6 joint. Note that the average strengths lists the value of the maximum tensile shear force divided by the maximum melted area and projected area of the tool, respectively. (c) Comparison of the maximum shear strength of different heat-assisted joining processes for Al/CFRTP joint. Hotpressing joining of Al5052-CF/PA6[32,38] and Al1050-CF/PA6[79]; Laser-assisted joining of Al7075-CF/PA6[80,81] and Al7075-CF/PPS[82]; Friction heat-assisted joining of current work and Al2060-CF/PEEK[78] and Al2060-GF/PEEK[83]; Others are resistance spot welding of Al5052-CF/PA6[84] and ultrasonically welding of Al5754-CF/PA66)[85].

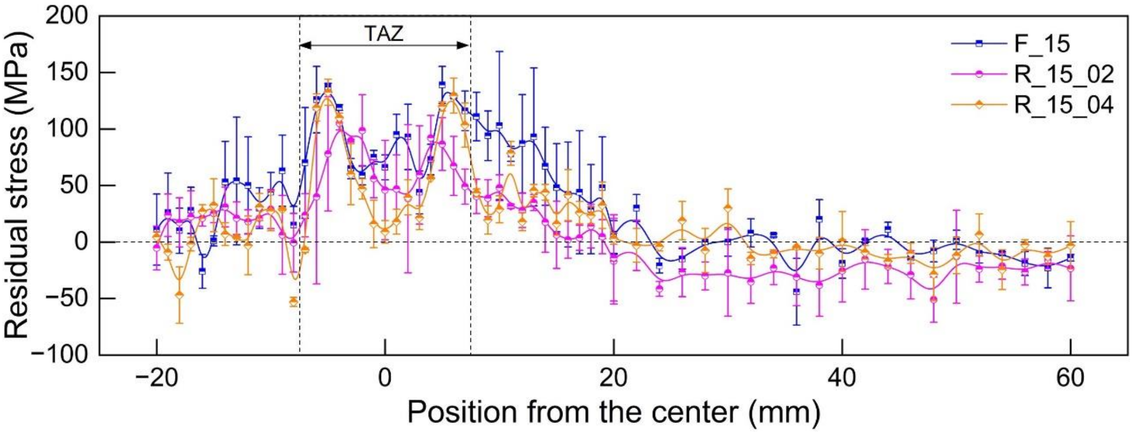

Fig. 56 Comparison of the surficial residual stresses along the sheet-length direction after the joining at different tools

6.4 Fracture morphology

The different fracture surface morphologies and crack extension paths, as well as the strength of the joints are interrelated [86]. Fig. 57 shows the fracture surface morphologies of different joints after the tensile shear tests. Combined with the cross-sectional morphology of the joints in Fig. 54 and the strength of the joints in Fig. 55, we summarize the fracture occurrence process of the joints fabricated by tools with different diameters and depths of indentation, and Fig. 58 shows the corresponding expected crack extension paths. Cracks typically initiated at the edge of the ROZ, where the melted resin was extruded outward under the squeezing force of the tool. It appeared that cracks initiated between the resolidified resin and the original resin, resulting in well-defined edges of residual CF/PA6 on the silanized Al alloy, as shown in Fig. 57. During the welding process, the temperature in the TAZ region was higher compared to the RAZ region, leading to severe thermal decomposition and cross-linking of porosity defects into larger areas, resulting in a higher density of porosity defects. Despite the outflow of molten resin with decomposition defects interspersed with fiber rods resulting in a thicker zone of resolidified resin in the RAZ, the lower temperature suppressed the size and density of porosity defects there. The amount of resolidified resin in the RAZ was significantly greater than in the TAZ region. As shown in Fig. 58, cracks initiated at the edge of the ROZ during the tensile shear experiments and propagated through the RAZ region along the porosity defects. Upon entering the TAZ, due to the high density of porosity defects caused by intense thermal decomposition of the resin near the Al alloy and the thinner region of remelted resin mixed with defects, cracks extended closer to the surface of the silanized Al alloy. Consequently, less CF/PA6 remained on the Al surface in the TAZ region compared to the RAZ region, as observed in Fig. 57. Comparing the fracture morphology corresponding to the 15 mm diameter tool with 0.2 mm and 0.4 mm depth of recess, the porosity defects caused by thermal decomposition near the weld interface are linked with each other to form a large defect area in the TAZ region of the fracture corresponding to the 0.2 mm tool. When the crack passes through, less CF/PA6 remains on the surface of the Al alloy in the TAZ region, showing a certain metallic luster; while in the TAZ region of the fracture corresponding to the 0.4 mm tool, the thermal decomposition is suppressed, and the porosity defects are scattered, making it difficult to form a large void area. The amount of re-solidified resin is higher, so more CF/PA6 is attached to the Al surface, which exhibits a dark gray color. In the fracture corresponding to the 12 mm tool with 0.4 mm recess, the TAZ region shows a similar morphology to that of the 15-mm tool. In the area outside the TAZ of the 12 mm tool, it can be found that the pure black color is more occupied due to the reduction of thermal decomposition defects inside the outflowed resin layer itself.

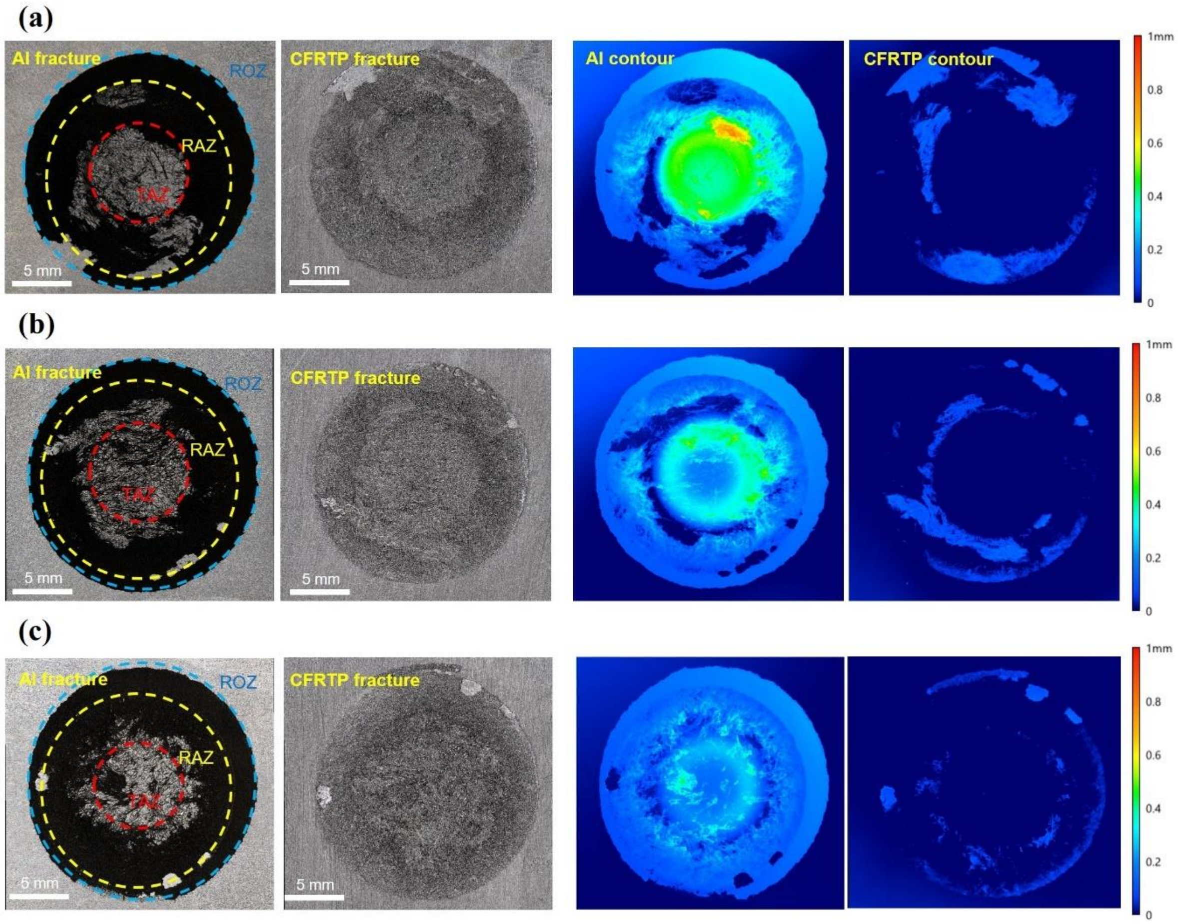

Fig. 57 Optical profiler images showing the macro-appearance of Al surface after welding and fractured surface. (a) 0.2mm recess-shaped Φ15mm tool, (b) 0.4mm recess-shaped Φ15mm tool and (c) 0.4mm recess-shaped Φ12mm tool.

The interfacial chemical bonding formed with a silane coupling agent coating as a transition layer has been confirmed as the dominant mechanism for the effective joining between silane-pretreated Al alloy and PA6 resin. Prior to the joining, the chemical reaction of silane layer to Al alloy is mainly through (Si-O-Al or Si-O-Mg) covalent bonds formed by hydrolyzed (-Si-O-Si-) bonds undergoing hydrogen-bonding transformation with Al or Mg in the Al alloy. During the joining process, the amide groups in PA6 and the epoxy groups in the silane layer undergo insertion and addition chemical reactions and ultimately form a stable covalent bond [12,13]. A strong interfacial joining between them strongly depends on the adequacy and extent of the chemical reaction, which is associated with the intimate contact without physical barriers and sufficient inter-diffusion of atoms or molecules on both sides of the interface [65]. Therefore, sufficient contact between the PA6 resin and the surface of the Al alloy as well as sufficiently high temperature are favorable conditions to ensure that the reaction proceeds. In our research and other related studies[13,63], it was found that the direct bonding strength between untreated metals and CF/PA6 was very low. After silane treatment, the silane film, acting as an intermediate layer, formed chemical bonds with both the metal side and the molten resin, significantly enhancing the joint strength. Observations from Fig. 57 indicated that the fracture mainly occurred in the chemical reaction region between the silane layer and the resin, with morphological characteristics of interfacial fracture near the silane layer and cohesive fracture within the re-solidified resin. Since this study did not perform mechanical interlocking surface pre-treatment, it could be concluded that the improvement in joint interface strength was mainly due to chemical bonding mechanism rather than mechanical interlocking. Moreover, based on previous XPS test results[60], covalent bonds formed through interface chemical reactions provided the bonding strength, consistent with the findings reported in Ref. [13,84].

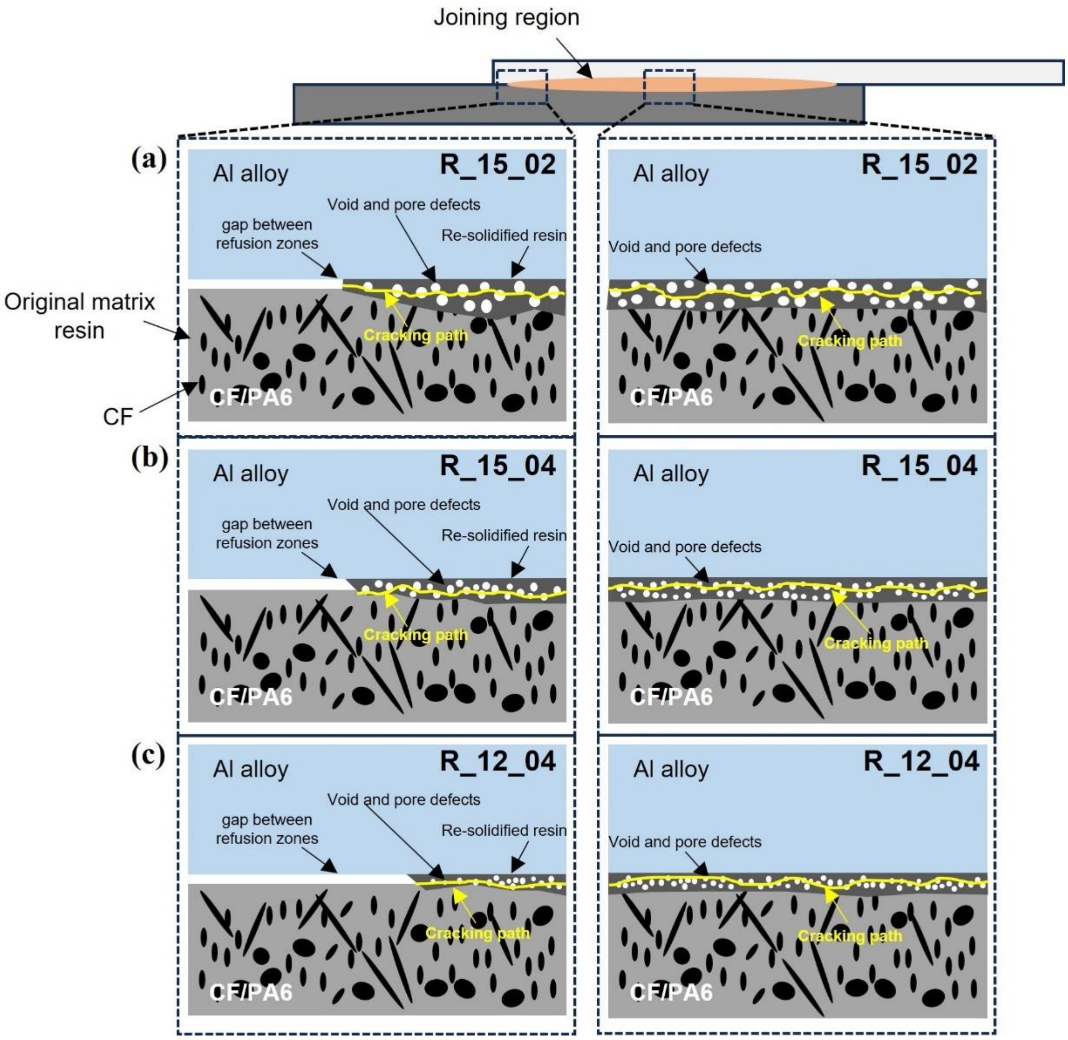

Fig. 58 Illustration of crack propagation within the joint interface of (a) 0.2mm recess-shaped Φ15mm tool, (b) 0.4mm recess-shaped Φ15mm tool and (c) 0.4mm recess-shaped Φ12mm tool.

6.5 Heat transfer characteristics

Fig. 59 shows the distribution of frictional transient heat flow at the tool/Al alloy surface produced by different tools. The heat originates in the frictional contact area and quickly dissipates outward, following this pattern across all tool friction interfaces. Heat generation correlates directly with tool diameter. Regardless of the tool shape, the lowest heat flow consistently occurs at the center of the friction area due to rotational friction properties, where heat generation relates to the radial speed at the current position. Comparison of heating times of 1s and 2s reveals that a flat tool consistently generates higher heat flow than a recessed tool of the same diameter. Conversely, increasing the depth of recessed tool grooves decreases transient heat flow at the same time point. The initial contact area of the recessed tool is smaller than that of the flat tool, reducing the friction area and consequent heat flow. However, by the time heating reaches 3 s, heat flow distribution encompasses the entire joining area regardless of tool structure.

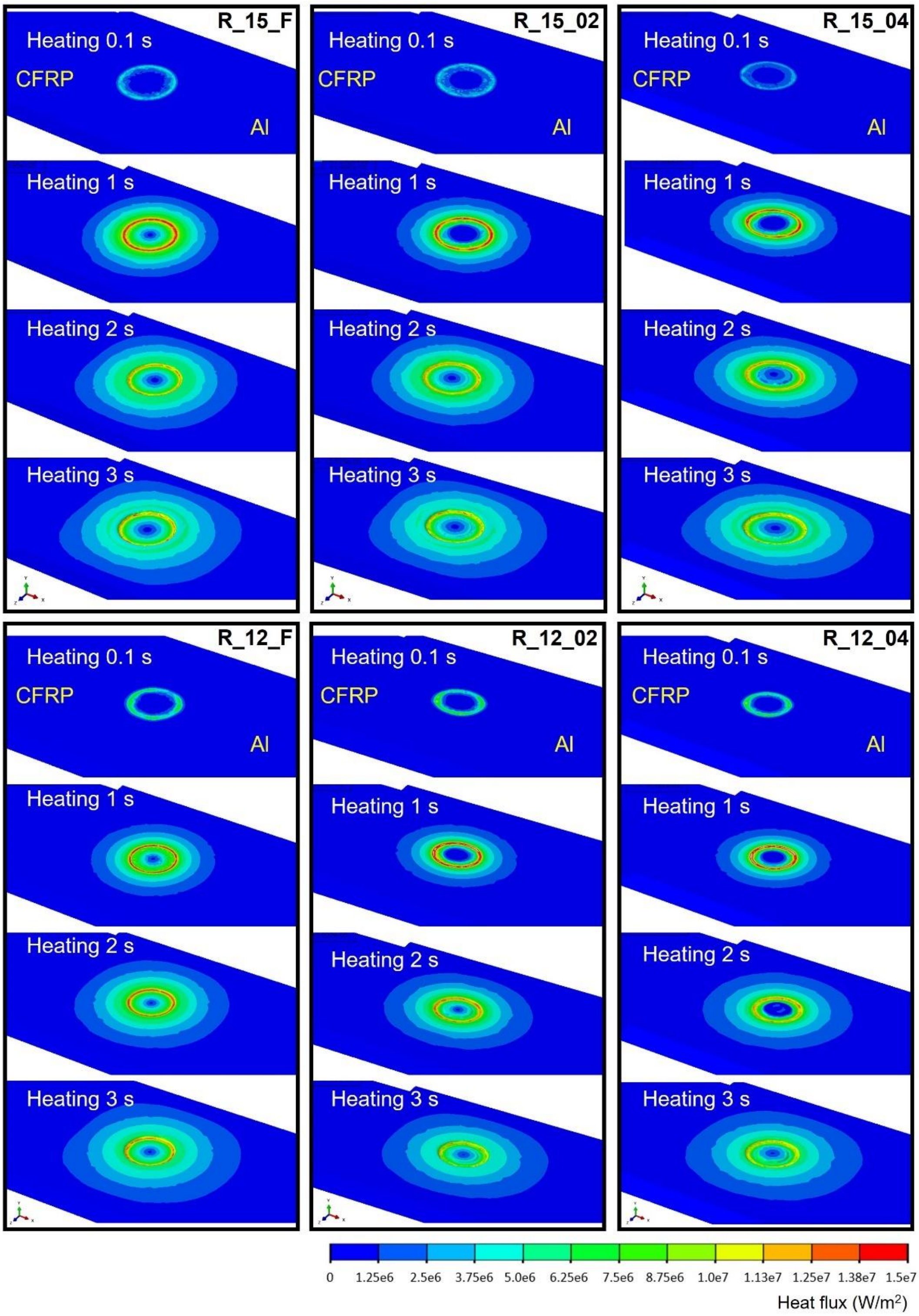

Fig. 59 Transient heat flux distribution on the tool-Al interface at different heating times.

The temperature field distributions in the joints produced by different tools are shown in Fig. 60. In the joint made by a flat tool with a diameter of 15 mm, the central temperature of the Al alloy rises rapidly within 3 s and forms an internal high-temperature zone (above 417 °C in Fig. 60a) almost the same diameter as the tool size. However, in the joint made with the recessed tool, the area of high temperature zone in the center of the Al alloy is significantly smaller than in the flat tool at the same moment, which is further reduced with increasing recess depth of tool. The same pattern exists in the joints made by the 12 mm diameter tool, and due to the reduction in the size of the tool diameter, the area of high temperature zone generated is smaller than that of the 15 mm tool at the same moment. Regardless of the size or shape of the tool used, the high temperature zone on the CF/PA6 side is significantly thin, which is caused by its lower thermal conductivity than the Al alloy.

In addition, Fig. 61(a-c) shows the temperature distributions along the joint interface at different times. Overall, the 15 mm diameter tool produces higher temperatures than the 12 mm tool due to the higher heat input. It is worth noting that, for recessed tools of different depths, there is an overlap in the temperature distribution curves at 1 s and 3 s shown in Fig. 61(a) and (c). It is evident that using a recessed tool results in lower temperatures at any position along the joint interface compared to using a flat tool. Particularly during the initial heat generation stage, due to the entire shoulder surface of the flat tool being involved in frictional heating, the interface temperature maintains a distribution pattern with high temperatures at the center gradually decreasing towards the sides. In contrast, with a recess-shaped tool, the interface temperature distribution exhibits an M-shape at the beginning stage. As the tool plunges and the recess zone of tool begins to contact the Al alloy surface, as shown in Fig. 61(b), the temperature in the central area gradually becomes higher than the sides, but the temperature gradient is significantly smaller than that with a flat tool. When using a tool with a larger recess depth, the aforementioned features become even more pronounced. The temperature history curves at the joint center point location for different tools are shown in Fig. 61(d). Compared to the flat tool, the heating rate and maximum temperature caused by the recessed tool are relatively low. Comparing the tools with the same diameter, the 0.4 mm depth recessed tools have a lower heating rate compared to the 0.2 mm depth, which implies that the 0.4 mm depth generates less heat and a shorter duration time above the decomposition temperature.

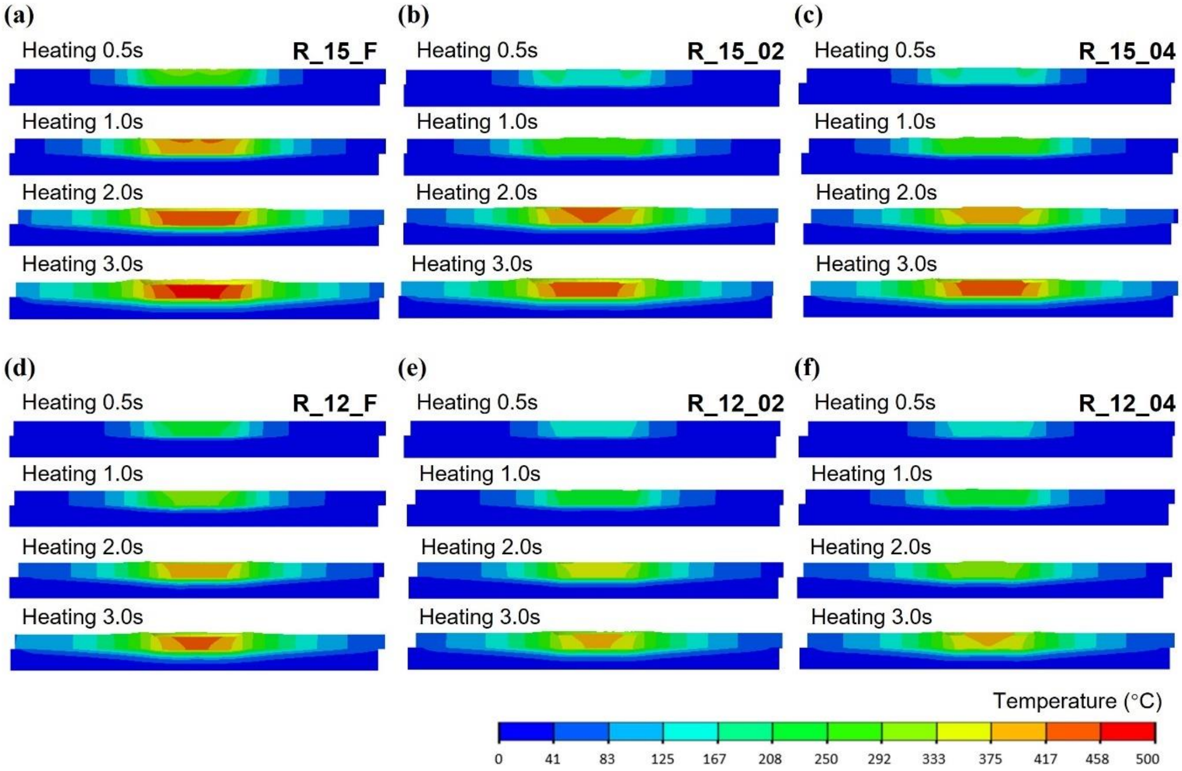

Fig. 60 Effects of different tool profiles on temperature field. (a) Flat-shaped Φ15mm tool, (b) 0.2mm recess-shaped Φ15mm tool, (c) 0.4mm recess-shaped Φ15mm tool, (d) flat-shaped Φ12mm tool, (e) 0.2mm recess-shaped Φ12mm tool, (f) 0.4mm recess-shaped Φ12mm tool.

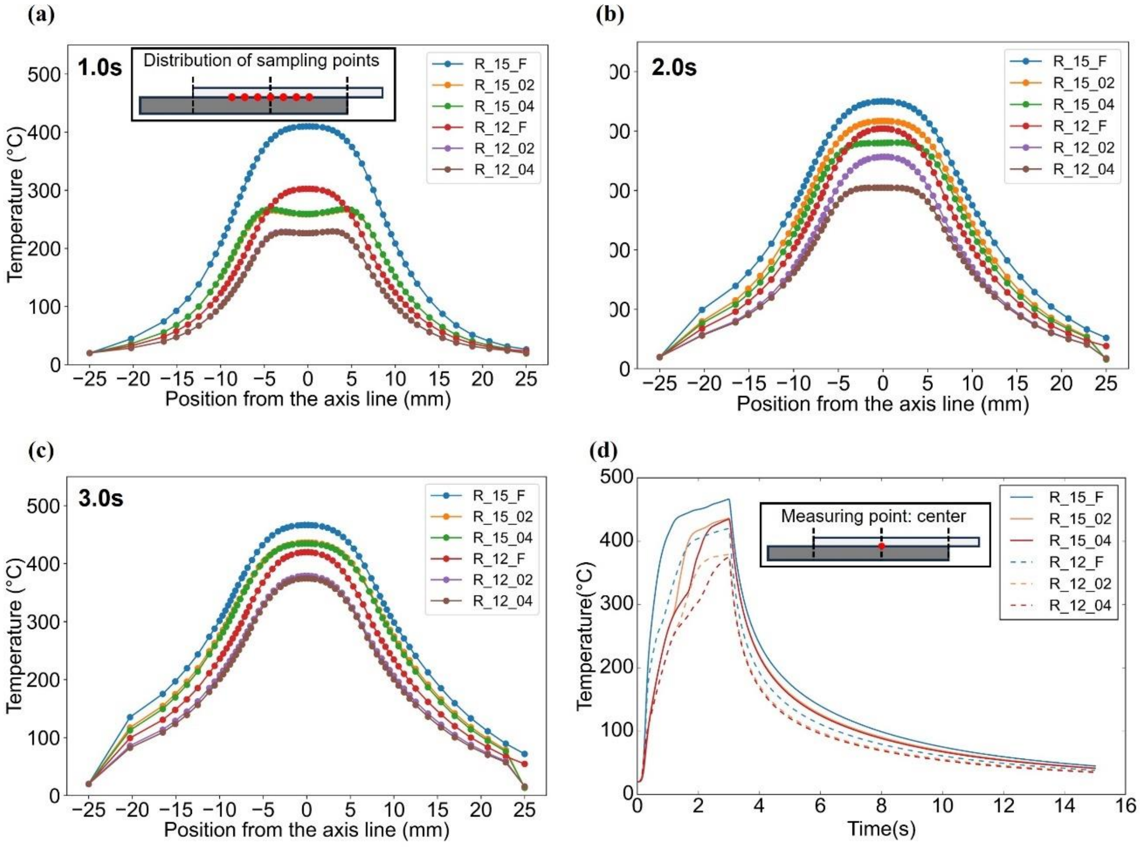

Fig. 61 Effects of tool profiles on the transient distribution of temperature across the Al-tool interface at (a) 1.0s, (b) 2.0s and (c) 3.0s. (d) The temperature history curves at the joint center.

6.6 Correlation between interfacial fracture and temperature distribution

The degree of chemical reaction and the density of thermal decomposition defects in the bonding area directly affect the joint strength, which is closely related to the temperature distribution of the interface. The temperature distribution and evolution determine the melting/decomposition durations and areas. The appropriate temperature not only promotes the chemical reaction between the epoxy and amide groups, but also improves the PA6 resin fluidity to adequately spread over the silanized Al alloy surface. This role of interface temperatures in enhancing interface bonding was also emphasized in a study by Sheikh-Ahmad et al.[72] in joining CF/PEEK to AA5052 by friction lap welding. Fig. 62 compares the melting/decomposition durations at different interface locations, and maximum/minimum duration times of TAZ are summarized in Fig. 63 (a). For the 12 mm and 15mm diameter tools, compared to the flat tool, the decomposition time was reduced for the recessed tools while the melting duration time was extended, with the 0.4mm depth resulting in a longer duration than the 0.2 mm depth. Therefore, using a recess-shaped tool with a significant depth, it ensured a more thorough chemical reaction between the molten resin and the silane layer, thereby avoiding excessive formation of porosity due to thermal decomposition. This heat transfer phenomenon aligns with experimental observations. The experimental results in Fig. 55(b) demonstrate that the maximum tensile shear force or strength occurred with the 0.4 mm-depth recessed tool. Tools of different diameters at this depth exhibited overall equivalent tensile shear strength. As shown in Fig. 63(a), for the 0.4 mm-depth recessed tool, the melting duration time in the TAZ region was approximately 1.6 to 2.1 s for the 15 mm diameter tool, and 1.9 to 2.5 s for the 12 mm diameter tool. This indicates that as the tool diameter decreases, the resin melting duration time slightly increases while the thermal decomposition time significantly decreases.

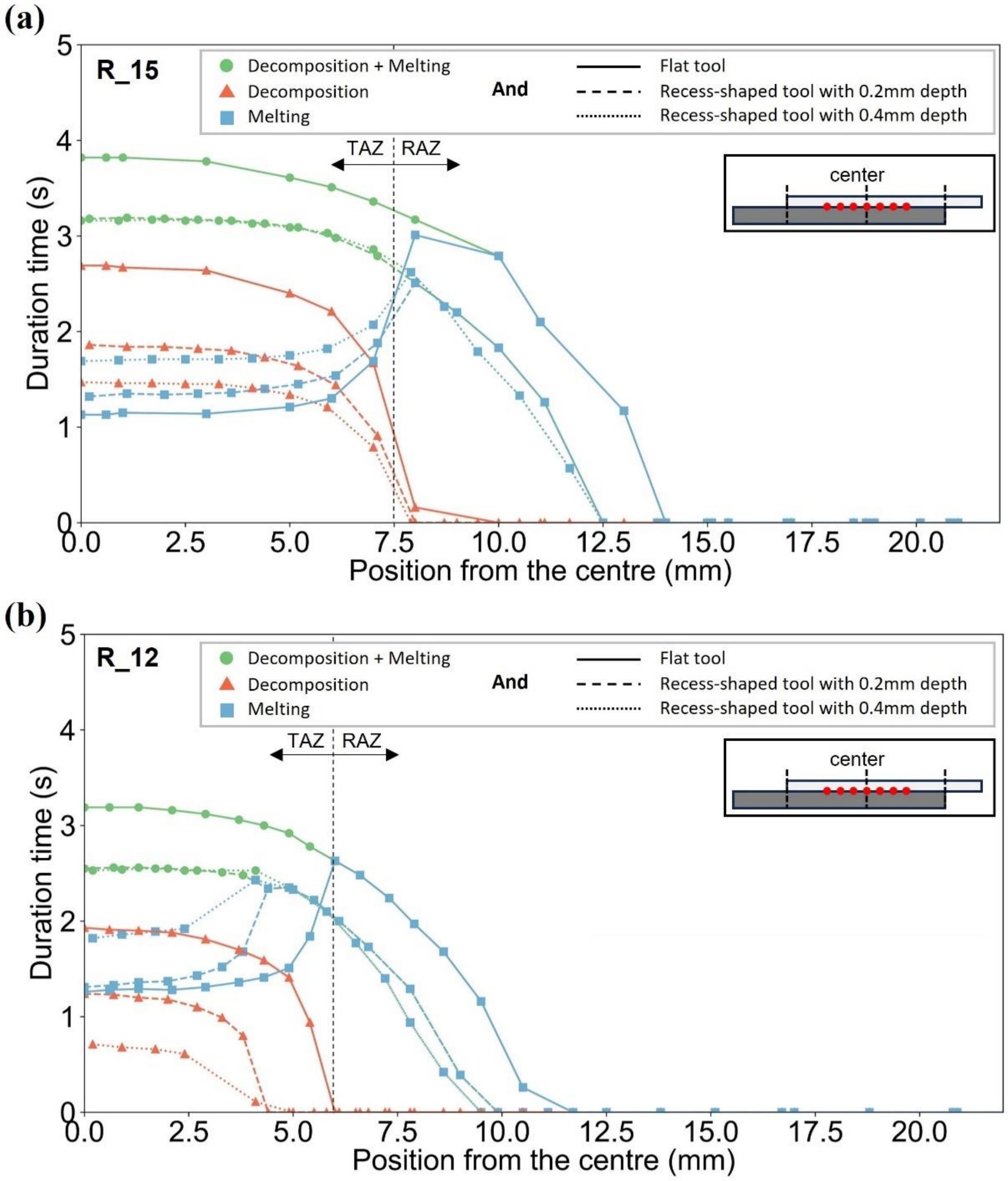

Fig. 62 The melting/decomposition duration times at different locations along the interface with (a) 15mm-diamater tool and (b) 12mm-diamater tool.

According to Choi et al. [13], joints with melting durations within 1.3 to 5.0 seconds, corresponding to adequate chemical reactions, exhibited the highest strengths on CF/PA6 substrates. Kimiaki et al. [75] also reported a sufficient reaction time between the silane layer and PA6 within a melting interval of 2.2 to 4.3 seconds. Therefore, using a 0.4 mm-depth recessed tool design under the current welding parameters can ensure more sufficient chemical reactions in the core interface region. Besides, under the current plunge depth conditions, when using a fixed 15mm diameter tool for joining, it is recommended to use a 0.4mm recessed tool to ensure sufficient chemical reaction in the interface region, particularly in the TAZ region, while minimizing the risks of thermal decomposition. When adjustable joint sizes are feasible, a smaller 12mm diameter recessed tool is recommended to achieve high-strength point joints between Al and CF/PA6.

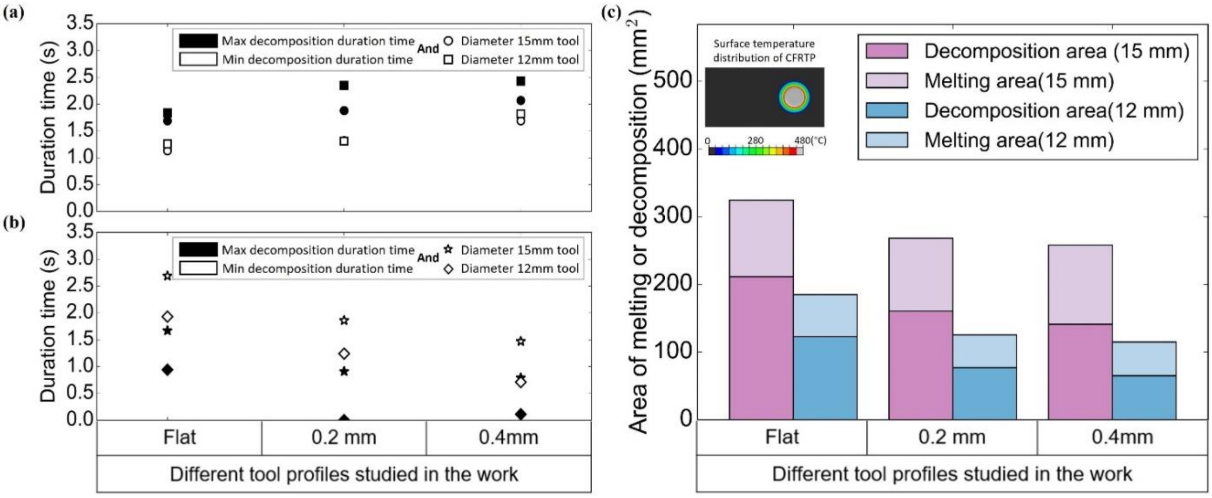

Fig. 63 The maximum/minimum (a) melting time and (b) decomposition time indside TAZ and (c) area of melting or decomposition region corresponding to different tools.

Fig. 63(c) illustrates the typical interface temperature distribution at the final time point of the weld (3 s after the start of the weld). The low-temperature region below the melting temperature of 220°C, the molten region above 220°C, and the decomposition region beyond 340°C are represented by black, color, and gray, respectively. The area of decomposition region (>340°C) and the area of molten region (220°C~340°C) corresponding to different tools are also shown in Fig. 63(c), respectively. Compared to a flat tool, a recess-shaped tool reduces the area of the decomposition zone and increases the percentage of the melting zone. For example, the percentage of melting area increases from 34% to 40% for a 0.2 mm recessed tool with a 15 mm diameter compared to a flat tool. And for the 12 mm tool, the percentage increased from 33% to 39%. The recessed tool effectively suppressed heat generation, thereby inhibiting resin decomposition and increasing the area of CF/PA6 in the melting state. Further when the recess depth increases from 0.2 mm to 0.4 mm, the percentage of the area of the melting zone increases from 40% to 45% and from 39% to 43% for the 15 mm tool and the 12 mm tool, respectively. The increase in recess depth further reduces the duration time of the resin above the decomposition temperature, which is consistent with the phenomenon observed in experiment shown in Fig. 54. Reducing the tool diameter from 15 mm to 12 mm at the recess depth of 0.4 mm results in a significant reduction in the area of the high temperature zone from approximately 300 mm^2 to 200 mm^2, while the percentage of the area of the melting zone is maintained at a comparable level for each recess depth. Overall, while the 12 mm tool limited the overall size of the weld area, the suppression of thermal decomposition within the joint still resulted in good average joint strength. Based on the above, using a 0.4 mm recess depth is more recommendable for recess-shaped tools.

6.7 Transferability of the Interpretable Strength Model to FSpJ Conditions

To further evaluate the applicability and generalizability of the interpretable strength prediction model distilled in Chapter 5, the derived mathematical formula was applied to a FSpJ process to predict the spatial distribution of bonding strength at the Al–CFRTP interface. The temperature field inputs were obtained from finite element simulations of FSpJ joints using flat tools with different diameters, as illustrated in Fig. 64(a). Specifically, the simulation result for the 15 mm flat tool (R_15_F) was reused from the thermal analysis discussed in Chapter 6, while the 20 mm flat tool (R_20_F) data was derived from our previous work [60].

In this model, the contact surface between CFRTP and aluminum was extracted from the simulation domain, temperatures were extracted from a predefined node set located on the CFRTP side. For each node, the temperature history over all time frames and steps was scanned, and the maximum temperature $Temp_{max}^{(i)}$ was identified:

$$Temp_{max}^{(i)} = \max_{t} temp^{(i)}(t) \tag{28}$$

where $temp^{(i)}(t)$ denotes the nodal temperature at time t for node i.

A constant nominal pressure of P = 0.4 MPa was assumed during joining. Given the dimensionless maximum temperature and normalized pressure, the nodal interfacial strength ($\sigma^{(i)}$) was predicted using the distilled regression model derived in Section 5.5. The functional form is:

$$\frac{\sigma^{(i)}}{60} = A \cdot (\frac{P}{60} + B)^m \cdot (\frac{Temp_{max}^{(i)}}{340})^n \cdot e^{-C \cdot \frac{Temp_{max}^{(i)}}{340}} \tag{29}$$

where A, B, C, m, n are the model parameters fitted from hot-press experimental data. This formulation accounts for both the thermal activation behavior of the resin and the dual influence of pressure on bonding efficiency. The maximum temperature, node strength, and node coordinate values were meshed to visualize the predicted strength field and maximum temperature field distribution. Fig. 64(b, c) and Fig. 64 (d, e) present the distributions of maximum interface temperatures and predicted strengths for two tool diameters: 15 mm (R_15_F) and 20 mm (R_20_F), respectively. It is evident that the highest temperatures occur near the geometrical center of the tool shoulder. As the tool diameter increases, a larger shoulder area contributes to increased heat generation, thereby enlarging the area affected by elevated temperatures. This trend is clearly observed in the broader temperature distribution in the R_20_F condition. The corresponding bonding strength distributions show a characteristic ring-like pattern, where strength is lower at the center and higher in the surrounding region. This is attributed to excessive thermal degradation of PA6 at temperatures exceeding 340 °C, which leads to void formation and reduced interfacial integrity in the central zone. In contrast, the surrounding regions experience temperatures within the optimal range (approximately 300–340 °C), which promotes favorable chemical interactions without resin decomposition, thereby achieving higher strength. Importantly, the tool with the larger diameter (R_20_F) results in a wider high-temperature area at the center, which expands the region susceptible to thermal degradation and lowers the strength over a broader area. This phenomenon is clearly reflected in the comparison of predicted strength contours in Fig. 64(d, e).

Moreover, to quantify the overall load-bearing capacity of the joint, the predicted strength values were integrated over the contact area. As shown in Fig. 64(a), for each element with average predicted strength $\bar{\sigma}_e$ calculated from the max temperature T_{max} and pressure P, the total load that the interface can support is obtained by integrating the strength and element area A_e of all elements, as shown in Fig. 64(f):

$$F_{total} = \sum_{e} (\bar{\sigma}_e * A_e)$$

The predicted total interface force was in reasonable agreement with the tensile shear test results, supporting the validity of the transferred model in capturing key trends in FSpJ processes. These findings demonstrate that the interpretable model derived from hot-press joining can be effectively extended to other thermal joining methods, such as FSpJ, provided that critical process inputs (temperature and pressure) are properly characterized. They also highlight the strong influence of tool geometry on thermal behavior and its implications for joint strength distribution.

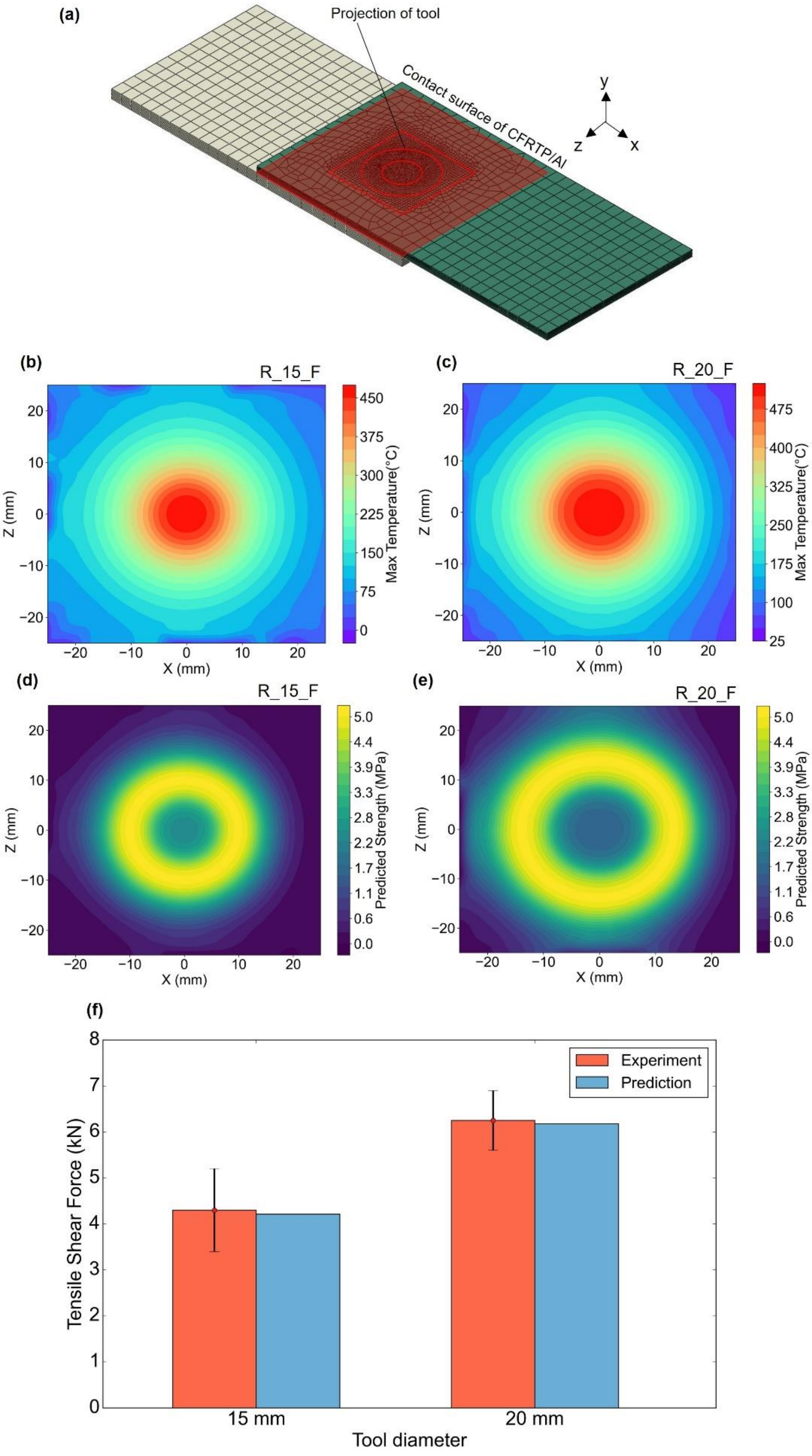
(a)
Projection of tool
Contact surface of CFRTP/Al
y
z
x
(b)
R_15_F
Z (mm)
X (mm)
Max Temperature(°C)
450
375
300
225
150
75
0
(c)
R_20_F
475
400
325
250
175
100
25
(d)
R_15_F
Predicted Strength (MPa)
5.0
4.4
3.9
3.3
2.8
2.2
1.7
1.1
0.6
0.0
(e)
R_20_F
(f)
Experiment
Prediction
Tensile Shear Force (kN)
15 mm
20 mm
Tool diameter

Fig. 64 The (a) Schematic diagram of Al/CFRTP interface and distributions of (b, c) simulated maximum temperature and (d, e) predicted interfacial strength for flat tool with diameter of 15mm(R_15_F) and 20mm(R_20_F), and (f) comparison of predicted and experimental tensile shear force.

6.8 Summary

Dissimilar point joints of 6061-T6 Al alloy and CF/PA6 were successfully obtained using tools of different shapes and sizes (flat and recess), and their bonding mechanisms and properties were compared experimentally and through simulations. The main conclusions are drawn as follows:

(1) Tool Geometry and Heat Production: The geometry of the joining tool significantly influenced heat production and distribution during the joining process. Tools with recess features, especially those with deeper recesses, were found to reduce the overall heat production compared to flat tools. This reduction in heat production was beneficial in minimizing thermal decomposition of the CF/PA6 resin matrix, thereby reducing defect formation.

(2) Joint Strength and Integrity: The tensile shear tests revealed that joints made with recessed tools exhibited superior mechanical properties compared to those made with flat tools. Specifically, increasing the depth of the recessed tool improved joint strength due to better suppression of interfacial deformation and reduced defect density within the resin matrix. Smaller diameter tools, although producing joints with smaller effective bonded areas, managed to maintain a high strength-to-area ratio due to enhanced thermal and mechanical conditions.

(3) Thermal Distribution and Resin Flow: The temperature distribution analysis indicated that recessed tools promoted a more uniform thermal field, which was crucial for achieving consistent resin melting and wetting of the silanized Al alloy surface. The suppression of excessive heat flow towards the resin also helped in maintaining the integrity of the polymer matrix, thus enhancing the overall joint quality.

(4) Crack Propagation and Defect Control: The study of fracture surfaces showed that recessed tools led to a more favorable distribution of residual resin on the Al alloy surface, indicating better interfacial bonding. The control of defect size and distribution through

optimized tool design was evident, which in turn contributed to the robustness of the joint under tensile loading.

(5) The predictive function distilled from hot-press experiments was applied to evaluate the interfacial strength distribution in FSpJ joints based on simulated temperature fields and assumed interface pressures. The results successfully revealed ring-shaped high-strength regions and center-weakening behavior consistent with thermal degradation mechanisms. The comparable magnitude and spatial trends confirmed the transferability of the quantitative model to more complex FSpJ processes, highlighting the practical potential of this interpretability-based modeling framework.

7. Summary and Outlook

This dissertation presents a comprehensive investigation into the thermo-mechanical joining mechanisms of aluminum alloys and carbon fiber-reinforced thermoplastics (CFRTP), with an emphasis on establishing quantitative relationships between joining process parameters, interfacial microstructures, and mechanical performance. The primary objective was to develop both experimental and data-driven methodologies that enhance our understanding and prediction of the joining behavior in metal–CFRTP hybrid systems, ultimately enabling more intelligent joint design and process optimization.

In the initial stages of this study (Chapter 2), a stable and controllable hot-press joining platform was constructed to allow systematic variation of thermal–mechanical inputs. Through a series of controlled experiments, the individual and coupled effects of temperature, holding time, and pressure on the joint strength were quantitatively assessed. Detailed interfacial characterizations using scanning electron microscopy (SEM), X-ray photoelectron spectroscopy (XPS), and Raman spectroscopy revealed the formation of Si–O–Al chemical bonds at the interface, as well as morphological evidence of resin flow, void formation, and thermal degradation. These findings highlighted the complex interplay between chemical reaction kinetics, polymer rheology, and defect evolution in the joining process.

In the Chapter 3, a thinning-controlled hot-press approach was proposed to explore the coupled influence of temperature and pressure. By constraining the vertical displacement of the pressure plate, the system allowed temperature-dependent changes in effective pressure to emerge naturally. This setup uncovered the dual role of pressure—facilitating interfacial contact and resin infiltration under moderate conditions but leading to excessive resin loss and structural defects when pressure or temperature was too high.

To move beyond qualitative interpretation, Chapter 5 proposed a data-driven modeling framework that integrates experimental observations, dimensional analysis, thermal simulations, and machine learning. A dataset encompassing process conditions, microstructure features, and joining strength was constructed and used to train gradient-boosted decision tree (GBDT) models. These models captured the nonlinear interactions among input variables and output performance, while feature importance analysis provided mechanistic insights. Importantly, interpretable mathematical expressions distilled from the trained models offered compact yet physically meaningful descriptors of the process–structure–property relationships, aiding both fundamental understanding and process design.

Chapter 6 further validated the generalizability of the insights gained by applying them to friction spot joining (FSpJ), a thermally assisted process with more complex heat and deformation fields. Through numerical simulation and experimental validation, the impact of tool geometry on temperature distribution, resin behavior, and joint performance was clarified, reinforcing the importance of precise thermal–mechanical control.

In conclusion, this research bridges the gap between experimental material joining studies and data-driven quantitative modeling. It demonstrates how physically informed machine learning approaches, when integrated with careful experimentation, can yield interpretable and predictive tools for hybrid joint design. Future work will focus on extending the proposed methodology to more complex 3D joint geometries, integrating time-dependent property evolution (e.g., creep or aging), and applying the framework to other multi-material combinations relevant to lightweight manufacturing and structural design in the automotive and aerospace industries.

References

[1] Ma H, Zhao Y, Qin G, Geng P. Formation of nanoscale reaction layer with several crystallinities in the friction-welded 6061 Al alloy/steel joint. Mater Des 2022;219:110742. https://doi.org/10.1016/j.matdes.2022.110742.

[2] Jiang H, Cao X, Gao J, Liu T, Chen H, Zhang Z. Design of Notch Filter Based on Spoof Surface Plasmon Polaritons. 2021 International Conference on Microwave and Millimeter Wave Technology (ICMMT), IEEE; 2021, p. 1–3. https://doi.org/10.1109/ICMMT52847.2021.9618262.

[3] Jiang H, Liao Y, Gao S, Li G, Cui J. Comparative study on joining quality of electromagnetic driven self-piecing riveting, adhesive and hybrid joints for Al/steel structure. Thin-Walled Structures 2021;164:107903. https://doi.org/10.1016/j.tws.2021.107903.

[4] Huang Y, Meng X, Xie Y, Li J, Wan L. New technique of friction-based filling stacking joining for metal and polymer. Compos B Eng 2019;163:217–23. https://doi.org/10.1016/j.compositesb.2018.11.050.

[5] Dawei Z, Qi Z, Xiaoguang F, Shengdun Z. Review on Joining Process of Carbon Fiber-Reinforced Polymer and Metal: Methods and Joining Process. Rare Metal Materials and Engineering 2018;47:3686–96. https://doi.org/10.1016/S1875-5372(19)30018-9.

[6] Naskar AK, Keum JK, Boeman RG. Polymer matrix nanocomposites for automotive structural components. Nat Nanotechnol 2016;11:1026–30. https://doi.org/10.1038/nnano.2016.262.

[7] Tao W, Su X, Chen Y, Tian Z. Joint formation and fracture characteristics of laser welded CFRP/TC4 joints. J Manuf Process 2019;45:1–8. https://doi.org/10.1016/j.jmapro.2019.05.028.

[8] Xia H, Ma Y, Chen C, Su J, Zhang C, Tan C, et al. Influence of laser welding power on steel/CFRP lap joint fracture behaviors. Compos Struct 2022;285:115247. https://doi.org/10.1016/j.compstruct.2022.115247.

[9] Liu Y, Su J, Tan C, Feng Z, Zhang H, Wu L, et al. Effect of laser texturing on mechanical strength and microstructural properties of hot-pressing joining of carbon fiber reinforced plastic to Ti6Al4V. J Manuf Process 2021;65:30–41. https://doi.org/10.1016/j.jmapro.2021.03.021.

[10] Balle F, Wagner G, Eifler D. Ultrasonic Metal Welding of Aluminium Sheets to Carbon Fibre Reinforced Thermoplastic Composites. Adv Eng Mater 2009;11:35–9. https://doi.org/10.1002/adem.200800271.

[11] Ren S, Ma Y, Saeki S, Iwamoto Y, Chen C, Ma N. Fracture mechanism and strength evaluation of Al5052/CFRP joint produced by coaxial one-side resistance spot welding. Compos Struct 2020;252:112766. https://doi.org/10.1016/j.compstruct.2020.112766.

[12] Ren S, Ma Y, Saeki S, Iwamoto Y, Ma N. Numerical analysis on coaxial one-side resistance spot welding of Al5052 and CFRP dissimilar materials. Mater Des 2020;188:108442. https://doi.org/10.1016/j.matdes.2019.108442.

[13] Choi J-W, Morisada Y, Liu H, Ushioda K, Fujii H, Nagatsuka K, et al. Dissimilar friction stir welding of pure Ti and carbon fibre reinforced plastic. Science and Technology of Welding and Joining 2020;25:600–8. https://doi.org/10.1080/13621718.2020.1788814.

[14] Geng P, Ma N, Ma H, Ma Y, Murakami K, Liu H, et al. Flat friction spot joining of aluminum alloy to carbon fiber reinforced polymer sheets: Experiment and simulation. J Mater Sci Technol 2022;107:266–89. https://doi.org/10.1016/j.jmst.2021.08.043.

[15] Wang S, Xu Y, Wang W, Tian Y, Zhang X, Huang H, et al. Enhancing interfacial bonding in friction stir lap welding of light metal and carbon fiber reinforced

polymer composite. J Manuf Process 2022;83:729–41. https://doi.org/10.1016/j.jmapro.2022.09.038.

[16] Wang T, Upadhyay P, Reza-E-Rabby M, Li X, Li L, Soulami A, et al. Joining of thermoset carbon fiber reinforced polymer and AZ31 magnesium alloy sheet via friction stir interlocking. The International Journal of Advanced Manufacturing Technology 2020;109:689–98. https://doi.org/10.1007/s00170-020-05717-9.

[17] Çoban O, Akman E, Bora MÖ, Genc Oztoprak B, Demir A. Laser surface treatment of CFRP composites for a better adhesive bonding owing to the mechanical interlocking mechanism. Polym Compos 2019;40:3611–22. https://doi.org/10.1002/pc.25224.

[18] Liu Y, Wu Q, Wang P, Zhuang W. Forming process prediction of a self-piercing riveted joint in carbon fibre reinforced composites and aluminium alloy based on deep learning. J Manuf Process 2023;106:453–64. https://doi.org/10.1016/j.jmapro.2023.10.015.

[19] Chen S-Z, Feng D-C, Han W-S, Wu G. Development of data-driven prediction model for CFRP-steel bond strength by implementing ensemble learning algorithms. Constr Build Mater 2021;303:124470. https://doi.org/10.1016/j.conbuildmat.2021.124470.

[20] SRIDHAR L. Investigation of thermal contact resistance at a plastic-metal interface in injection molding. New Jersey Institute of Technology; 1999.

[21] Boldyrev AI, Schleyer P v. R. Ab initio prediction of the structures and stabilities of the hyperaluminum molecules: Al3O and square-planar Al4O. J Am Chem Soc 1991;113:9045–54. https://doi.org/10.1021/ja00024a003.

[22] Colin B, Lavastre O, Fouquay S, Michaud G, Simon F, Laferte O, et al. Contactless Raman Spectroscopy-Based Monitoring of Physical States of Silyl-Modified Polymers during Cross-Linking. Green and Sustainable Chemistry 2016;06:151–66. https://doi.org/10.4236/gsc.2016.64015.

[23] Tuma R. Raman spectroscopy of proteins: from peptides to large assemblies. Journal of Raman Spectroscopy 2005;36:307–19. https://doi.org/10.1002/jrs.1323.

[24] Anastassakis E, Pinczuk A, Burstein E, Pollak FH, Cardona M. Effect of static uniaxial stress on the Raman spectrum of silicon. Solid State Commun 1993;88:1053–8. https://doi.org/10.1016/0038-1098(93)90294-W.

[25] Bomstein Joseph. Infrared Spectra of Oxirane Compounds. Correlations with Structure. Anal Chem 1958;30:544–6. https://doi.org/10.1021/ac60136a029.

[26] Shih PTK, Koenig JL. Raman studies of silane coupling agents. Materials Science and Engineering 1975;20:145–54. https://doi.org/10.1016/0025-5416(75)90143-3.

[27] Pelletier MJ. Quantitative Analysis Using Raman Spectrometry. Appl Spectrosc 2003;57:20A-42A. https://doi.org/10.1366/000370203321165133.

[28] Caspers PJ, Bruining HA, Puppels GJ, Lucassen GW, Carter EA. In Vivo Confocal Raman Microspectroscopy of the Skin: Noninvasive Determination of Molecular Concentration Profiles. Journal of Investigative Dermatology 2001;116:434–42. https://doi.org/10.1046/j.1523-1747.2001.01258.x.

[29] McCreery RL. Raman spectroscopy for chemical analysis. John Wiley & Sons; 2005.

[30] Balle F, Huxhold S, Wagner G, Eifler D. Damage Monitoring of Ultrasonically Welded Aluminum/ CFRP-Joints by Electrical Resistance Measurements. Procedia Eng 2011;10:433–8. https://doi.org/10.1016/j.proeng.2011.04.074.

[31] Huang Y, Meng X, Xie Y, Li J, Wan L. Joining of carbon fiber reinforced thermoplastic and metal via friction stir welding with co-controlling shape and performance. Compos Part A Appl Sci Manuf 2018;112:328–36. https://doi.org/10.1016/j.compositesa.2018.06.027.

[32] Iwata K, Suzuki A, Kim S-G, Takata N, Kobashi M. Enhancing the solid-state joinability of A5052 and CFRTP via an additively manufactured micro-structure. J Mater Process Technol 2022;306:117629. https://doi.org/10.1016/j.jmatprotec.2022.117629.

[33] Abe H, Chung JC, Mori T, Hosoi A, Jespersen KM, Kawada H. The effect of nanospike structures on direct bonding strength properties between aluminum and carbon fiber reinforced thermoplastics. Compos B Eng 2019;172:26–32. https://doi.org/10.1016/j.compositesb.2019.05.025.

[34] Jiao J, Jia S, Xu Z, Ye Y, Sheng L, Zhang W. Laser direct joining of CFRTP and aluminium alloy with a hybrid surface pre-treating method. Compos B Eng 2019;173:106911. https://doi.org/10.1016/j.compositesb.2019.106911.

[35] Jiao J, Ye Y, Jia S, Xu Z, Ouyang W, Zhang W. CFRTP -Al alloy laser assisted joining with a high speed rotational welding technology. Opt Laser Technol 2020;127:106187. https://doi.org/10.1016/j.optlastec.2020.106187.

[36] Lambiase F, Paoletti A, Durante M. Mechanism of bonding of AA7075 aluminum alloy and CFRP during friction assisted joining. Compos Struct 2021;261:113593. https://doi.org/10.1016/j.compstruct.2021.113593.

[37] Meng X, Huang Y, Xie Y, Li J, Guan M, Wan L, et al. Friction self-riveting welding between polymer matrix composites and metals. Compos Part A Appl Sci Manuf 2019;127:105624. https://doi.org/10.1016/j.compositesa.2019.105624.

[38] Li W, Geng P, Wang Q, Ma N, Zhao S, Chen C. Effect of thermal condition on isothermal-pressing joined strength of silanized Al alloy/carbon fiber-reinforced polyamide-6. Journal of Materials Research and Technology 2023;24:8035–52. https://doi.org/10.1016/j.jmrt.2023.05.043.

[39] Harper JF, Miller NA, Yap SC. The Influence of Temperature and Pressure During the Curing of Prepreg Carbon Fiber Epoxy Resin. Polym Plast Technol Eng 1993;32:269–75. https://doi.org/10.1080/03602559308019234.

[40] Leclerc JS, Ruiz E. Porosity reduction using optimized flow velocity in Resin Transfer Molding. Compos Part A Appl Sci Manuf 2008;39:1859–68. https://doi.org/10.1016/j.compositesa.2008.09.008.

[41] Amico S, Lekakou C. An experimental study of the permeability and capillary pressure in resin-transfer moulding. Compos Sci Technol 2001;61:1945–59. https://doi.org/10.1016/S0266-3538(01)00104-X.

[42] Gunpinar E, Khan S. A multi-criteria based selection method using non-dominated sorting for genetic algorithm based design. Optimization and Engineering 2020;21:1319–57. https://doi.org/10.1007/s11081-019-09477-8.

[43] Zhang Y, Kim NH, Park C, Haftka RT. Function Extrapolation at One Inaccessible Point Using Converging Lines. Volume 2B: 41st Design Automation Conference, American Society of Mechanical Engineers; 2015. https://doi.org/10.1115/DETC2015-47689.

[44] Iliescu D, Gehin D, Iordanoff I, Girot F, Gutiérrez ME. A discrete element method for the simulation of CFRP cutting. Compos Sci Technol 2010;70:73–80. https://doi.org/10.1016/j.compscitech.2009.09.007.

[45] Miyano Y, Nakada M. Accelerated testing methodology for durability of CFRP. Compos B Eng 2020;191:107977. https://doi.org/10.1016/j.compositesb.2020.107977.

[46] Carslaw HS, Jaeger JC, Feshbach H. *Conduction of Heat in Solids*. Phys Today 1962;15:74–6. https://doi.org/10.1063/1.3057871.

[47] Salje EKH, Schranz W. Low amplitude, low frequency elastic measurements using dynamic mechanical analyzer (DMA) spectroscopy. Zeitschrift Fur Kristallographie 2011;226:1–17. https://doi.org/10.1524/zkri.2011.1253.

[48] Li W, Geng P, Ma N, Chen C. Effect of thermal-mechanical conditions on strength of silanized Al alloy/CFRTP hybrid joint made by thinning-controlled

hot pressing. Mater Today Commun 2024;38:108507. https://doi.org/10.1016/j.mtcomm.2024.108507.

[49] He W-T, Liao S-T, Xiang Y-S, Long L-J, Qin S-H, Yu J. Structure and Properties Study of PA6 Nanocomposites Flame Retarded by Aluminium Salt of Diisobutylphosphinic Acid and Different Organic Montmorillonites. Polymers (Basel) 2018;10:312. https://doi.org/10.3390/polym10030312.

[50] Hu H, Wei Q, Wang T, Ma Q, Jin P, Pan S, et al. Experimental and Numerical Investigation Integrated with Machine Learning (ML) for the Prediction Strategy of DP590/CFRP Composite Laminates. Polymers (Basel) 2024;16:1589. https://doi.org/10.3390/polym16111589.

[51] Bai T, Wang D, Yan J, Cheng W, Cheng H, Shi SQ, et al. Wetting mechanism and interfacial bonding performance of bamboo fiber reinforced epoxy resin composites. Compos Sci Technol 2021;213:108951. https://doi.org/10.1016/j.compscitech.2021.108951.

[52] Bamane SS, Gaikwad PS, Radue MS, Gowtham S, Odegard GM. Wetting Simulations of High-Performance Polymer Resins on Carbon Surfaces as a Function of Temperature Using Molecular Dynamics. Polymers (Basel) 2021;13:2162. https://doi.org/10.3390/polym13132162.

[53] Xie J, Chen K, Yan M, Guo J, Xie Q, Lü F. Effect of temperature and water penetration on the interfacial bond between epoxy resin and glass fiber: A molecular dynamics study. J Mol Liq 2022;350:118424. https://doi.org/10.1016/j.molliq.2021.118424.

[54] Pramanik M, Early M, Wand S, Gottschalk D, Mendon SK, Rawlins JW. Amidoamine: Synthesis, disparity in cure with epoxy resins between bulk and solvent systems, and structure–property relationships of its epoxy-based coatings. Polym Eng Sci 2019;59. https://doi.org/10.1002/pen.24858.

[55] Araújo A, Franco L, Barreto J, Barros A, Bezerra E, Luna C, et al. Insights on the processing and thermal degradation kinetics of <scp>PA6</scp> / <scp>PE-g-AA</scp> blends. J Appl Polym Sci 2024;141. https://doi.org/10.1002/app.55489.

[56] Watanabe M, Satoh K. Control of Angular Distortion Due To Welding Conditions in T-fillet Welded Joints. Journal of the Japan Welding Society 1956;25:343–8. https://doi.org/10.2207/qjjws1943.25.343.

[57] Tozaki Y, Uematsu Y, Tokaji K. Effect of tool geometry on microstructure and static strength in friction stir spot welded aluminium alloys. Int J Mach Tools Manuf 2007;47:2230–6. https://doi.org/10.1016/j.ijmachtools.2007.07.005.

[58] Kim J-R, Ahn E-Y, Das H, Jeong Y-H, Hong S-T, Miles M, et al. Effect of tool geometry and process parameters on mechanical properties of friction stir spot welded dissimilar aluminum alloys. International Journal of Precision Engineering and Manufacturing 2017;18:445–52. https://doi.org/10.1007/s12541-017-0053-0.

[59] Huang Y, Meng X, Wang Y, Xie Y, Zhou L. Joining of aluminum alloy and polymer via friction stir lap welding. J Mater Process Technol 2018;257:148–54. https://doi.org/10.1016/j.jmatprotec.2018.02.043.

[60] Geng P, Ma H, Li W, Murakami K, Wang Q, Ma N, et al. Improving bonding strength of Al/CFRTP hybrid joint through modifying friction spot joining tools. Compos B Eng 2023;254:110588. https://doi.org/10.1016/j.compositesb.2023.110588.

[61] Peng C, Jing C, Siyi Q, Siqi Z, Shoubo S, Ting J, et al. Friction stir welding joints of 2195-T8 Al–Li alloys: Correlation of temperature evolution, microstructure and mechanical properties. Materials Science and Engineering: A 2021;823. https://doi.org/10.1016/j.msea.2021.141501.

[62] Ji S, Cui X, Ma L, Liu H, Zuo Y, Zhang Z. Achieving High-Quality Aluminum to Copper Dissimilar Metals Joint via Friction Stir Double-Riveting Welding. Acta Metallurgica Sinica (English Letters) 2023;36:552–72. https://doi.org/10.1007/s40195-022-01512-5.

[63] Geng P, Ma N, Ma H, Ma Y, Murakami K, Liu H, et al. Flat friction spot joining of aluminum alloy to carbon fiber reinforced polymer sheets: Experiment and simulation. J Mater Sci Technol 2022;107:266–89. https://doi.org/10.1016/j.jmst.2021.08.043.

[64] Geng P, Ma Y, Ma N, Ma H, Aoki Y, Liu H, et al. Effects of rotation tool-induced heat and material flow behaviour on friction stir lapped Al/steel joint formation and resultant microstructure. Int J Mach Tools Manuf 2022;174. https://doi.org/10.1016/j.ijmachtools.2022.103858.

[65] Wang YC, Wong PMH, Kodur V. An experimental study of the mechanical properties of fibre reinforced polymer (FRP) and steel reinforcing bars at elevated temperatures. Compos Struct 2007;80:131–40. https://doi.org/10.1016/j.compstruct.2006.04.069.

[66] Zhang XX, Xiao BL, Ma ZY. A Transient Thermal Model for Friction Stir Weld. Part I: The Model. Metallurgical and Materials Transactions A 2011;42:3218–28. https://doi.org/10.1007/s11661-011-0729-5.

[67] Cao JY, Wang M, Kong L, Yin YH, Guo LJ. Numerical modeling and experimental investigation of material flow in friction spot welding of Al 6061-T6. The International Journal of Advanced Manufacturing Technology 2017;89:2129–39. https://doi.org/10.1007/s00170-016-9247-3.

[68] Ma N, Geng P, Ma Y, Shimakawa K, Choi J-W, Aoki Y, et al. Thermo-mechanical modeling and analysis of friction spot joining of Al alloy and carbon fiber-reinforced polymer. Journal of Materials Research and Technology 2021;12:1777–93. https://doi.org/10.1016/j.jmrt.2021.03.111.

[69] Das A, Bang HS, Bang HS. Numerical modelling in friction lap joining of aluminium alloy and carbon-fiber-reinforced-plastic sheets. IOP Conf Ser Mater Sci Eng 2018;369:012032. https://doi.org/10.1088/1757-899X/369/1/012032.

[70] Lundström F, Frogner K, Andersson M. Numerical modelling of CFRP induction heating using temperature-dependent material properties. Compos B Eng 2021;220:108982. https://doi.org/10.1016/j.compositesb.2021.108982.

[71] Zhang B, Chen X, Pan K, Li M, Wang J. Thermo-mechanical simulation using microstructure-based modeling of friction stir spot welded AA 6061-T6. J Manuf Process 2019;37:71–81. https://doi.org/10.1016/j.jmapro.2018.11.010.

[72] Sheikh-Ahmad J, Zitoune R, Morel C, Ferrero JF, Vieille B. Joining of AA5052 to CF/PEEK by friction lap welding. International Journal of Advanced Manufacturing Technology 2024;132:1137–50. https://doi.org/10.1007/s00170-024-13457-3.

[73] Ota E, Matsuda T, Shoji H, Ogura T, Miyasaka F, Sano T, et al. Friction stir spot welding of aluminum and carbon fiber reinforced thermoplastic using hybrid surface treatment improving interfacial properties. Mater Des 2021;212:110221. https://doi.org/10.1016/j.matdes.2021.110221.

[74] Abibe AB, Sônego M, dos Santos JF, Canto LB, Amancio-Filho ST. On the feasibility of a friction-based staking joining method for polymer–metal hybrid structures. Mater Des 2016;92:632–42. https://doi.org/10.1016/j.matdes.2015.12.087.

[75] Kimiaki N, Hironobu T, Bolyu X, Atsuki T, Kazuhiro N. Effect of silane coupling on the joint characteristics of friction lap joined Al alloy/CFRP. Welding International 2018;32:328–37. https://doi.org/10.1080/09507116.2017.1346819.

[76] Tanaka K, Aiba Y. Evaluation of Joint Strength for CFRPs and Aluminum Alloys by Friction Stir Spot Welding Using Multi-Stage Heating. Journal of Composites Science 2024;8:110. https://doi.org/10.3390/jcs8030110.

[77] Guo Y, Zhao H, Ai C, Zhao J, Su H, Chen J, et al. Parameter optimization of friction stir spot welded Al 6061 and CFRTP PA6 with surface treatment and interfacial adhesion. Thin-Walled Structures 2024;197:111585. https://doi.org/10.1016/j.tws.2024.111585.

[78] Huang Y, Meng X, Xie Y, Li J, Wan L. Joining of carbon fiber reinforced thermoplastic and metal via friction stir welding with co-controlling shape and performance. Compos Part A Appl Sci Manuf 2018;112:328–36. https://doi.org/10.1016/j.compositesa.2018.06.027.

[79] Abe H, Chung JC, Mori T, Hosoi A, Jespersen KM, Kawada H. The effect of nanospike structures on direct bonding strength properties between aluminum and carbon fiber reinforced thermoplastics. Compos B Eng 2019;172:26–32. https://doi.org/10.1016/j.compositesb.2019.05.025.

[80] Tao W, Su X, Chen Y, Tian Z. Joint formation and fracture characteristics of laser welded CFRP/TC4 joints. J Manuf Process 2019;45:1–8. https://doi.org/10.1016/j.jmapro.2019.05.028.

[81] Jiao J, Ye Y, Jia S, Xu Z, Ouyang W, Zhang W. CFRTP -Al alloy laser assisted joining with a high speed rotational welding technology. Opt Laser Technol 2020;127. https://doi.org/10.1016/j.optlastec.2020.106187.

[82] Lambiase F, Paoletti A, Durante M. Mechanism of bonding of AA7075 aluminum alloy and CFRP during friction assisted joining. Compos Struct 2021;261:113593. https://doi.org/10.1016/j.compstruct.2021.113593.

[83] Meng X, Huang Y, Xie Y, Li J, Guan M, Wan L, et al. Friction self-riveting welding between polymer matrix composites and metals. Compos Part A Appl Sci Manuf 2019;127:105624. https://doi.org/10.1016/j.compositesa.2019.105624.

[84] Ren S, Ma Y, Saeki S, Iwamoto Y, Chen C, Ma N. Fracture mechanism and strength evaluation of Al5052/CFRP joint produced by coaxial one-side resistance spot welding. Compos Struct 2020;252. https://doi.org/10.1016/j.compstruct.2020.112766.

[85] Balle F, Huxhold S, Wagner G, Eifler D. Damage monitoring of ultrasonically welded aluminum/CFRP-joints by electrical resistance measurements. Procedia Eng, vol. 10, Elsevier Ltd; 2011, p. 433–8. https://doi.org/10.1016/j.proeng.2011.04.074.

[86] Zhang Z, Liu H, Ji S, Zhang J, Jin C, Ma L, et al. Enhanced formation quality and tensile shear load of 7B04 aluminum alloys lap joint by impacting flow friction stir lap welding. Journal of Materials Research and Technology 2024;30:5096–108. https://doi.org/10.1016/j.jmrt.2024.04.197.

Achievements

Publications related to doctor thesis:

[1] **Li W**, Geng P, Ma N, Chen C. Effect of thermal-mechanical conditions on strength of silanized Al alloy/CFRTP hybrid joint made by thinning-controlled hot pressing. Mater Today Commun 2024;38:108507. https://doi.org/10.1016/j.mtcomm.2024.108507.

[2] **Li W**, Geng P, Ma N, Fujii H, Ma H. Effect of tool shoulder geometry on lapped Al/CFRTP hybrid joint structure and strength made by pinless friction spot joining. Journal of Materials Research and Technology 2024;33:2183–98. https://doi.org/10.1016/j.jmrt.2024.09.192.

[3] **Li W**, Geng P, Wang Q, Ma N, Zhao S, Chen C. Effect of thermal condition on isothermal-pressing joined strength of silanized Al alloy/carbon fiber-reinforced polyamide-6. Journal of Materials Research and Technology 2023;24:8035–52. https://doi.org/10.1016/j.jmrt.2023.05.043.

[4] **Li W**, Geng P, Ma N, Interpretable Data-Driven Modeling of Process-Microstructure-Strength Relationship in Hot-Press Joining of Aluminum and CFRTP, submitted to Composite Structures, 2025.

[5] **李蔚豪**, 耿培皓, & 麻寧緒. (2024, March). 減肉制御熱圧接合による Al 合金/CFRTP ハイブリッド接合部の強度に対する熱機械条件の影響. In *溶接学会全国大会講演概要 2024 年度春季全国大会* (pp. 126-127). 一般社団法人 溶接学会.

[6] **Li, W.**, Geng, P., Ma, N., Yasuhiro, A., & Hidetoshi, F. (2023). Al/CFRTP 摩擦スポット接合における接合強度に及ぼすツール変更の影響. *溶接学会全国大会講演概要*, 2023, 94-95.

[7] **李蔚豪**, 耿培皓, & 麻寧緒. (2023). 炭素繊維強化プラスチックとアルミニウ

ム合金の熱圧接合強度に及ぼす諸条件の定量化評価. In *溶接学会全国大会講演概要2023年度秋季全国大会* (pp. 148-149). 一般社団法人 溶接学会.

Other Publications:

[1] Geng P, Ma H, **Li W**, Murakami K, Wang Q, Ma N, et al. Improving bonding strength of Al/CFRTP hybrid joint through modifying friction spot joining tools. Compos B Eng 2023;254:110588. https://doi.org/10.1016/j.compositesb.2023.110588.

[2] Geng P, Morimura M, Ma N, Huang W, **Li W**, Narasaki K, et al. Measurement and simulation of thermal-induced residual stresses within friction stir lapped Al/steel plate. J Mater Process Technol 2022; 310: 117760. https://doi.org/10.1016/j.jmatprotec.2022.117760.

[3] Ren S, Chen H, Ma N, **Li W**, Saeki S, Iwamoto Y, et al. Coaxial one-side resistance spot welding for cross-lap joints of Al5052 and CFRP: Thermal process and strength evaluation. Journal of Materials Research and Technology 2024;28:1032–43. https://doi.org/10.1016/j.jmrt.2023.12.076.

[4] Choi J-W, **Li W**, Ushioda K, Yamamoto M, Fujii H. Influence of solute Mg and Zener–Hollomon parameter on microstructural evolution of linear-friction-welded Al joints. Journal of Materials Research and Technology 2023;23:4334–45. https://doi.org/10.1016/j.jmrt.2023.02.078.

[5] Choi J-W, **Li W**, Ushioda K, Yamamoto M, Fujii H. Strengthening mechanism of high-pressure linear friction welded AA7075-T6 joint. Mater Charact 2022;191:112112. https://doi.org/10.1016/j.matchar.2022.112112.

[6] Choi J-W, **Li W**, Ushioda K, Yamamoto M, Fujii H. Microstructure evolution and hardness distribution of linear friction welded AA5052-H34 joint and AA5083-O joint. Journal of Materials Research and Technology 2022;17:2419–30. https://doi.org/10.1016/j.jmrt.2022.02.003.

[7] Choi J-W, **Li W**, Ushioda K, Yamamoto M, Fujii H. Effect of applied pressure on microstructure and mechanical properties of linear friction welded AA1050-H24 and AA5052-H34 joints. Science and Technology of Welding and Joining 2022;27:92–102. https://doi.org/10.1080/13621718.2021.2013710.

[8] 崔正原, 山本元道, **李蔚豪**, 潮田浩作, & 藤井英俊. (2022). 線形摩擦接合された析出強化型 Al 合金の強化機構の解明. In *溶接学会全国大会講演概要 2022 年度秋季全国大会* (pp. 74-75). 一般社団法人 溶接学会.

[9] 崔正原, **李蔚豪**, 潮田浩作, & 藤井英俊. (2023). 線形摩擦接合における Al 合金継手の高効率化の検討. 軽金属溶接= Journal of light metal welding: *軽金属溶接協会誌*, 61(8), 357-361.

Acknowledgements

First and foremost, I would like to express my sincere gratitude to supervisor Prof. Ninshu Ma, header of the department of Joining Mechanics and Analyses, Joining and Welding Research Institute, for providing me with the opportunity to conduct my doctoral research in such an outstanding academic environment. His visionary leadership and consistent encouragement have shaped the foundation of this work and inspired me throughout my journey.

I am deeply indebted to Associate Prof. Peihao Geng, for his patient guidance, insightful feedback, and unwavering support over the years. His deep expertise and continuous mentoring were crucial in helping me overcome challenges and refine both the technical and conceptual aspects of this research.

I am also grateful to Assistant Prof. Qian Wang, and Prof. Hisashi Serizawa for their active involvement and expert advice in the research project. Their expertise and insights have significantly contributed to the depth and quality of my study.

I also extend my heartfelt thanks to the faculty members and colleagues at the Joining and Welding Research Institute (JWRI), Osaka University, for their support, stimulating discussions, and collaborative spirit. I am particularly grateful to Dr. Kunio Narasaki, Prof. Sendong Ren, Dr. Song Wu, Prof. Hui Huang, Dr. Fujun Cao, Prof. Yaqiong Ge, Prof. Pengkang Zhao, Prof. Jiamin Sun, Prof. Jingjing Li, Mr. Renzhi Zhang, Dr. Yifan Gao, Mr. Mingzhe Fan, Mr. Suyu Wang, Mr. Jingjia Chen, Mr. Mohan He, Mr. Tianxing Chang, Mr. Liangyu Fei, Mr. Kai Song, Mr. Di Yang, Mr. Yang Li, Dr. Onishi, Dr. Miyamoto, Mr. Aso, Mrs. Kikuchi, Mrs. Hirose, Mrs. Nakahara, Mrs. Akaji, and others lab members for their technical assistance and generous help during experiments and data analysis.

This research was supported in part by the Japan Society for the Promotion of Science (JSPS) KAKENHI, Amada Foundation, whose financial assistance I gratefully acknowledge.

Finally, I would like to thank my family, especially my wife Mrs. Xuran Guo, my parents Mrs. Yuning Bian and Mr. Guoyuan Li. They have always been my strongest pillar, offering unconditional love, encouragement, and sacrifice that enabled me to pursue this path. I am also grateful to my friends and who have stood by me through all the highs and lows of this journey.

I am deeply grateful to everyone mentioned above for their contributions and support. This dissertation would not have been possible without the support of all of them.